Topological Defects in Coulomb Crystals
Spectroscopy and Dynamics of Solitons

Andreas Sören Jonathan Brox

Fakultät für Mathematik und Physik
Albert-Ludwigs-Universität Freiburg

Topological Defects in Coulomb Crystals
Spectroscopy and Dynamics of Solitons

Andreas Sören Jonathan Brox
aus Herdecke

Dissertation zur Erlangung des Doktorgrades
der
Fakultät für Mathematik und Physik
der
Albert-Ludwigs-Universität Freiburg im Breisgau

Mai 2017

Dekan:	Prof. Dr. Gregor Herten
Betreuer/Erstgutachter:	Prof. Dr. Tobias Schätz
Zweitgutachter:	Prof. Dr. Giuseppe Sansone
Tag der mündlichen Prüfung:	26. Oktober 2017
Prüfer:	Prof. Dr. Tobias Schätz
	Prof. Dr. Jens Timmer
	Prof. Dr. Alexander Rohrbach

Abstract

A lack of order seems to be easily achievable. However, during the crystallization process, a system seeks for perfect order, that is, its configuration of minimal energy. By evolving the phase-transition on timescales beyond the exchange of information between different sections of the crystal, sub-ensembles reach perfect crystalline order. However, they might become incommensurate at their common boarders. We recently revealed in Coulomb crystals of laser-cooled trapped ions that these topological defects are created and stored in a stable manner in their self-induced trapping potential. Such defects can be treated as quasi-particles and it has been predicted that their description is identical to those of solitons.

In this thesis, I present experimental results on radial eigenmode spectroscopy, depending in frequency on the existence of the soliton. Resonant excitation in the presence of the continuous damping drives the structural defect out of its self-induced potential. Timescales depend on the excitation strength. We experimentally derive the depth of the Peierls-Nabarro potential. In addition, we resolve transport directionality of the defect to the side of the crystalline structure, depending on the structure of the defect itself.

Zusammenfassung

Unordnung scheint leicht generierbar zu sein. Trotzdem strebt jedes System während des Kristallisationsprozesses nach dem Zustand minimaler Energie, in diesem Fall die fehlerfreien Kristallstruktur. Wenn der Phasenübergang auf Zeitskalen erfolgt, die so schnell sind, dass kein Informationsaustausch zwischen unterschiedlichen Subdomänen des Kristalls stattfinden kann, bilden sich Untereinheiten der optimalen Struktur. Jedoch passen diese aneinander grenzenden Bereiche nicht zwangsläufig zusammen. Wir konnten zeigen, dass Coulomb Kristalle aus gespeicherten, laser-gekühlten Ionen solch topologische Defekte aufweisen und diese stabil für längere Zeit in ihrem selbsterzeugten Speicherpotential gehalten werden können. Solche Defekte können als Quasi-Teilchen betrachtet werden, deren Beschreibung der von Solitonen gleicht.
In dieser Arbeit zeige ich experimentelle Ergebnisse radialer Eigenmodenspektroskopie, die in der Frequenz von der Anwesenheit des Solitons im Kristall abhängen. Resonante Anregung bei zeitgleicher Laserkühlung führt zum Verlust der strukturellen Defekte aus ihrem selbstinduzierten Potential. Die Zeitskalen hängen von der Anregungsstärke ab. Wir leiten aus experimentellen Ergebnissen die Tiefe des Peierls-Nabarro Potentials ab. Zudem können wir abhängig von der Struktur des Defekts die Transportrichtung der Defekte zum jeweiligen Ende des Kristalls auflösen.

Contents

List of Figures

Chapter 1

Introduction

1.1 Motivation

Nature features imperfections, as defects disturb periodicity inside crystaline structures. Examples for naturally structural defects are Schottky defects [3] (missing atom in the lattice) and Frenkel defects [4] (additional atom). These defects can become useful, namely by doping of silicon with foreign atoms like boron or phosphor. This leads to a change in the valence-conduction band gap, allowing to manipulate macroscopic conductivity of semiconductors. Addressing and controlling these structural defects is challenging, as their interatomic distance is on the order of few Å.

Recently, it was proposed that magnifying the interatomic distance of the crystalline structure enables individual control and adressability. This can be realized by atoms in optical lattices [5] or by ion crystals confined in radiofrequency traps [6]. Ionic crystals are generated, by decelerating charged atoms to Coulomb crystals by laser-cooling [7]. In addition, ion crystals can be doped by foreign atomic ions or even molecular ions [1, 8, 9]. The trapping potential of the radiofrequency trap can be tuned deterministically, allowing structural phase transitions from linear over planar to three-dimensional crystals [1, 10–12]. For the case of two dimensions, crystals might feature subdomains of individual periodicity. These subdomains are devided by a domain wall, having properties of quasi-particles. These can be described as discrete solitons, also referred to as kinks. Many groups, both theoretical and experimental, study these solitons in the context of condensed matter, atomic physics, optics or cosmology [13–15].

Several proposals predict, that defects in finite ion crystals can be created by multiple methods. The most prominent one is a non-adiabatic change of the trapping potential [16, 17]. These phase-transitions has been theoretically studied by Kibble and Zurek [18–21]. These predictions have been experimentally realized by several groups [22–24]. Localized defects in ion crystals have been experimentally generated during a

first order phase transition from an ion cloud to the crystalline structure [2, 6]. Since these discrete defects have been deterministically created, they are in many cases of experimental interest. In all these experiments the lifetime of these defects has been limited to hundreds of milli-seconds. This short lifespan impedes the investigation of fundamental properties of the solitons. It has been predicted that these properties give insight into gap seperated vibrational eigenmodes [16], meaning the change of dispersion relation due to the presence of the defect. In addition, they might be suited to study effects in quantum information [25, 26] and quantum coherence [27, 28].

In this thesis, I realize long term stable solitons in Coulomb crystals and measure their properties. The experimental results reveal that the lifetime of these defects is related to the size of the system. In the next step, I performed spectroscopy on the vibrational eigenmodes of Coulomb crystals related to the presence of the soliton. In addition, I derive the energy barrier the soliton has to overcome related to the Peierls-Nabarro potential. Furthermore, I excite on resonance a vibrational eigenmode to study internal energy transfer and motional excitation of quasi-particles.

1.2 Outline

This thesis is structured the following:

- In chapter 2, I introduce on relevant theoretical aspects, like ion trapping and laser cooling. In addition, I point out aspects of structural defects in Coulomb crystal, like occurrence and shape, as well as their relevance on the eigenmode spectrum. In order to study dynamical aspects, I define the position of the structural defect as well as its velocity. Finally, I adopt an established model [29] to our system, to obtain access on the depth of the soliton induced trapping potential.
- Chapter 3 gives a general overview on the experimental setup. I focus on the important modifications, like the quadrupol excitation field and the image analysis routine. Furthermore I summarize the numerical methodes, we use to gain deeper understanding on the timescales inside the system.
- Chapter 4 shows the results of eigenmode spectroscopy of a structural defect based on quadrupol excitation. We achieve frequency selectivity as well as structure selectivity in the Coulomb crystal. Based on this, I show first results on the lifetime of solitons in the presence of resonant excitation of the crystal. In combination with numerics, we can estimate the depth of the Peierls-Nabarro potential.
- Chapter 5 focuses on the dynamical aspects of these structural defects inside the ion crystal. There are transformation processes between individual conformations, which reveal their relative conformational energy. Additionally I present the results on the direction of motion of the individual conformations.

Chapter 2

Theoretical background

In this thesis, we present first systematic results on static and dynamical aspects of structural defects in Coulomb crystals. These consist of trapped ions, which are confined by electric fields and cooled to the milli-Kelvin regime. In the first part we discuss the theoretical background of the relevant physical concepts of ion trapping and laser cooling of atomic ions.
In the following section, we give a short overview on the properties of structural defects and their dynamics inside these laser cooled crystalline structures [1, 2, 30]. This can be described as a diffusion process of a quasi-bound particle. As they escape their local potential well on long timescales, we use Kramers' escape model to derive the barrier height of the Peierls-Nabarro potential.

2.1 Atomic ions in a confining potential

This chapter summarizes main aspects of trapping of charged particles in a linear Paul trap, as shown in [31]. Subsequently, a short summary on laser cooling of atomic ions is presented. Further details are described, e.g. in [32, 33].

2.1.1 Trapping atomic ions

Single ions are harmonically confined at a certain place, if there is a restoring force $\vec{F}$, pushing them back to a local minimum of the potential Φ. As $\vec{F} = -\nabla\Phi$, we describe a three dimensional confining potential to trap particles by:

$$\Phi(x, y, z) \propto (\alpha\, x^2 + \beta\, y^2 + \gamma\, z^2). \tag{2.1}$$

To confine charged particles, we use in our experiment electric fields to generate the trapping potential. Laplace's equation $\Delta\Phi = 0 = \alpha + \beta + \gamma$ has to be fulfilled for electric fields. Thus, W. Paul [31] suggested to choose, e.g. $\alpha = 0$ and $\beta = -\gamma$ to

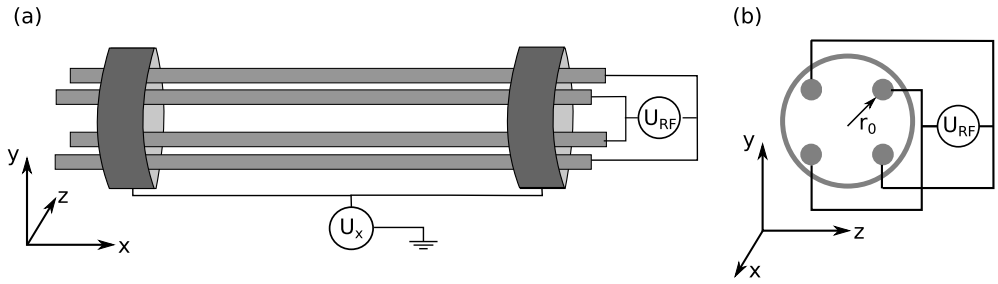

Figure 2.1: Scetch of a linear Paul trap: An alternating voltage is applied to four pairwaise connected electrode rods. Both pairs are $\approx \pi$ out of phase.
(a) U_x is applied to two ring shaped electrodes and controls the confinement of charged particles in x-direction.
(b) Lateral view on the trap: The vector $\vec{r}_0$ indicates the radial distance from the center of the trap.

generate a two dimensional trapping potential, like:

$$\Phi(y,z) = \frac{\Phi_0}{2r_0^2}\left(y^2 - z^2\right), \tag{2.2}$$

where r_0 is the radial distance from the trap center to one of the four electrodes, see fig. 2.1 (b). This is realized in Paul traps by a combination of static and alternating (DC, AC) electric fields, whereas Φ_0 is time dependent:

$$\Phi_0(t) = U_{\mathrm{DC}} - U_{\mathrm{RF}} \cdot \cos\left(\Omega_{\mathrm{RF}} t\right), \tag{2.3}$$

with Ω_{RF} as alternating frequency of the radiofrequency drive. The AC electric field is applied to four rods arranged in a square, which are diagonally connected, see fig. 2.1 (b). They are pairwise π out of phase. This results to a saddle potential in two dimension: y and z. Such a potential confines in one direction, whereas it defocuses in the other direction. A charged particle moves along the gradient of the potential in direction of the minima of the saddle. We invert the voltages pairwise, so the particle is pushed back again. Switching the voltages on short timescales ($1/\Omega_{\mathrm{RF}}$), the particles are on time average confined in radial direction.
The axial confinement is given by U_x, a DC voltage, applied to two ring shaped electrodes, see fig. 2.1 a. So the whole potential to trap charged particles can be written as

$$\begin{aligned}\Phi\left(x,y,z,t\right) = &\frac{1}{2\,r_0^2}\left(U_{\mathrm{DC}} - U_{\mathrm{RF}} \cdot \cos\left(\Omega_{\mathrm{RF}}\,t\right)\right)\left(y^2 - z^2\right) \\ &+ \frac{1}{2}\,\alpha_{\mathrm{x}}\,U_{\mathrm{x}}\,x^2 - \frac{1}{2}\,\alpha_{\mathrm{x}}\,U_{\mathrm{x}}\,\left(y^2 + z^2\right)\end{aligned} \tag{2.4}$$

and α_x is a geometrical factor specific for each Paul trap. The relevant parameters of our trap are described in [8, 9]. The ion's motion inside the potential is described by

the solution of the equation of motion in each of the three dimensions. The derivation is scetched for instance in one of the radial directions:

$$\ddot{y} = e/m \, \frac{U_{\mathrm{DC}} - U_{\mathrm{RF}} \cdot \cos\left(\Omega_{\mathrm{RF}}\, t\right)}{r_0^2} \, y, \tag{2.5}$$

with the electron charge e and the mass of the atomic ion m. The differential equation is a Mathieu equation and can be solved by Matthieu's ansatz. The solution of equation 2.5 can be written as

$$y(t) \propto \left[1 - \frac{q}{2}\cos\left(\Omega_{\mathrm{RF}} t\right)\right] \cos\left(\frac{\beta_y \Omega_{\mathrm{RF}}}{2} t\right), \tag{2.6}$$

with $q = \frac{2\,e\,U_{\mathrm{RF}}}{m\,\Omega_{\mathrm{RF}}^2\,r_0^2}$ and $\beta_y = \sqrt{a + q^2/2} \ll 1$, with $a = \frac{4\,e\,U_{\mathrm{DC}}}{m\,\Omega_{\mathrm{RF}}^2\,r_0^2}$. Particles are long term stable, if a and q are in regions of stable trapping of the stability diagram, for instance $a \leq q < 0.5$ [31].
The solution of the equation of motion has two periodic terms, one with Ω_{RF} and a second with $\frac{\beta_y\,\Omega_{\mathrm{RF}}}{2}$. The first part has the same frequency as the RF-drive of the Paul trap and is caused by the oscillation of the electric field. It is called micromotion and its contribution to the ion's motion increases with its distance from the trap axis.
The oscillatory motion of the second term of the ion with mass m has a smaller frequency compared to the micromotion and is called the secular frequency $\omega_{\mathrm{sec},i}$.

$$\omega_{\mathrm{sec},y} = \omega_y = \sqrt{\frac{1}{2}\left(\frac{e\,U_{\mathrm{RF}}}{m\,r_0^2\,\Omega_{\mathrm{RF}}}\right)^2 - \frac{e\,U_{\mathrm{DC}}}{m\,r_0^2}}. \tag{2.7}$$

These calculations can be done analogous for the z-direction to derive the corresponding secular frequency.

$$\omega_{\mathrm{sec},z} = \omega_z = \sqrt{\frac{1}{2}\left(\frac{e\,U_{\mathrm{RF}}}{m\,r_0^2\,\Omega_{\mathrm{RF}}}\right)^2 + \frac{e\,U_{\mathrm{DC}}}{m\,r_0^2}}. \tag{2.8}$$

Both frequencies are degenerate in the case of $U_{\mathrm{DC}} \approx 0$. Secular frequencies of ions depend on the ion's mass as $\omega_{\mathrm{sec},i} \propto 1/m$.

So far, we focused on the radial directions. In axial direction, there is no time dependent electric field. The secular frequency is calculated by:

$$\omega_{\mathrm{sec},x} = \omega_x = \sqrt{\frac{e\,U_x}{m\,x_0^2}}, \tag{2.9}$$

with U_x the voltage symmetrically applied to both ring electrodes as introduced above. The global trapping potential can be rewritten as an harmonic oscillator potential. $\omega_{\mathrm{sec},i}$ are the eigenfrequencies of each of the three dimensions of the potential. For instance in axial direction, it can be written as

$$\Phi'(x) = m\,\omega_x^2\,x^2. \tag{2.10}$$

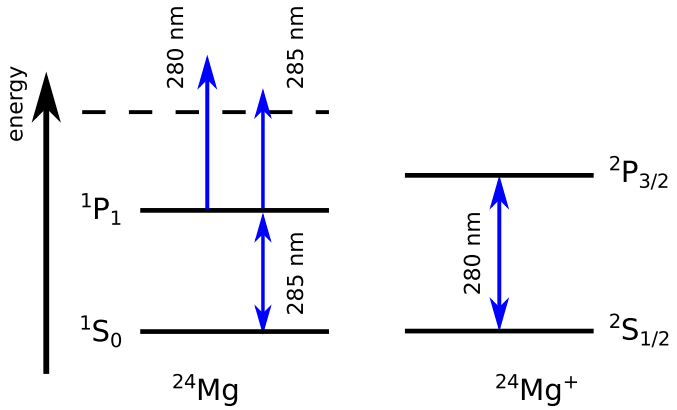

Figure 2.2: Scetch of the level scheme of Magnesium (Mg). On the left, the photo ionization process of a neutral magnesium atom is depicted. Two photons are necessary to exceed the binding energy of the electron. One excites the atom to the $^1P_1$ level and another photon transfer the electron to the continuum [34]. This is accomplished by two photons with the energy corresponding to at least 285 nm.
The right part shows the relevant levels of the ion. Line width of the transition is $\Gamma = 2\pi \cdot 42\,\mathrm{MHz}$. As there are no additional levels, this is a closed transition necessary for laser cooling, see text. Figure similar to [35].

Based on these equations, we trap a charged particle.
Introducing the reduced mass of several ions to the equations of motion, we can extend these equations for several particles. As we are interested in crystalline structures, we have to cool the motional degrees of freedom of the particles. We want to study structures, that are dominated by Coulomb repulsion. The kinetic energy of the particles has to be at least in the same order as the repulsive energy due to identical charges, otherwise the ions would not crystallize to an ordered structure [7]. Therefore, we use the laser cooling technique as introduced in the next section.

2.1.2 Laser cooling of Magnesium ions

As discussed above charged particles can be confined in a certain volume. We use magnesium ions in our experiments, as the atomic species is well established in the group. Its properties will be discussed in the following:
Magnesium has three isotopes - ^{24}Mg, ^{25}Mg and ^{26}Mg - with a natural abundance of 0.79, 0.1 and 0.11. Ionized ^{25}Mg atoms are used at the quantum simulation experiments in our lab, as it has a nuclear spin of 5/2 and therefore a hyperfine structure, for details see [6, 36, 37]. In addition, there are no D-Levels, so we do not have to take care of additional atomic levels we have to repump.

$^{24}Mg^+$ ions are used in this thesis, as these are the ions of the dominant isotope. The magnesium atom belongs to the group of alkaline earth atoms. To ionize the atom, we

use a two photon transition, introduced by [34]. The ions are confined by the electric fields of the Paul trap. Once ionized it has a single valence electron and offers a so called closed cycling transition between the indicated levels, see fig. 2.2 on the right side. Thus, it is suitable for laser cooling.

Laser cooling The deceleration of ions is realized by laser cooling techniques [38]. Here is only given a short overview, for details see [33]:
If ion and photon counter- propagate, the ion will be decelerated due to momentum transfer. An ion absorbs a photon out of the laser beam, which has the corresponding wavelength $\lambda = 280\,\mathrm{nm}$ to the $S_{1/2} \rightarrow P_{3/2}$ transition, as shown in fig. 2.2. This inelastic process leads to momentum transfer from the photon to the atomic ion. The photon is reemitted in random direction and as indicated by the level scheme the atom decays to the ground state within the mean lifetime $1/\Gamma = 1/(2\pi \times 41.8\,\mathrm{MHz}) \approx 3.8\,\mathrm{ns}$ of the excited state (a so called closed transition). Averaging over time the momentum transfer via absorption is along $\vec{k}_\mathrm{L}$ of the laser, whereas the repulsion of the reemission of the photon averages to zero. The laser force $\vec{F}_\mathrm{L}$ interacting with the ion is proportional to the scattering rate:

$$\vec{F}_\mathrm{L} = \frac{h}{2\pi}\,\vec{k}_\mathrm{L}\,R_\mathrm{sc}, \tag{2.11}$$

with h as Planck's constant and the scattering rate R_sc:

$$R_\mathrm{sc} = \frac{I/I_\mathrm{sat}\cdot\Gamma/2}{1 + I/I_\mathrm{sat} + \left(\frac{2\,\delta - \vec{k}_\mathrm{L}\cdot\vec{v}}{\Gamma}\right)^2} \tag{2.12}$$

and I as the intensity of the laser beam, I_sat the saturation intensity calculated by $I_\mathrm{sat} = \frac{\pi\,h\,c\,\Gamma}{3\,\lambda^3}$. $\delta = \omega - \omega_0$ is the detuning with respect to the atomic transition $\omega_0 = 2\pi\,c/\lambda$, c speed of light and $\vec{v}$ the velocity of the atoms. The scattering rate depends on the detuning δ and the intensity of the laser. The detuning of the laser frequency has to match the Doppler shift of the internal electronic transitions. Ions, propagating along $-\vec{k}_\mathrm{L}$, absorb photons with a higher energy. We choose $\omega < \omega_0$ to ensure that only atoms counter propagating the laser absorb photons. To obtain optimized cooling rates, we set $\delta \approx -\Gamma/2$ and obtain a "red" detuned laser. For such a detuning, we do not reach minimal temperature, but we still have a reasonable scattering rate.

We use this force to decelerate the ions, so their kinetic energy decreases to the same order of magnitude as their Coulomb repulsion. The cooling in one dimension and the coupling of all motional degrees of freedom due to the trapping potential of the Paul trap leads to a deceleration in all three dimensions. This process is limited by repulsion, as the excited state of the atom decays via spontaneous emission of a photon. The temperature limit that can be reached in one dimension in the case of no further scattering events and is given by

$$T_\mathrm{D} = \frac{h\,\Gamma}{4\,\pi\,k_\mathrm{B}} \approx 1\,\mathrm{mK}, \tag{2.13}$$

the Doppler temperature, with k_B as the Boltzmann constant and the line width of the transition Γ. Therefore, it is the limit that we can achieve with classical laser cooling techniques.

The $^{24}Mg^+$ ions are confined in a Paul trap and laser cooled to the milli-Kelvin regime.

In addition, we use such light forces to excite motion. For instance, we modulate the intensity in time to drive motion corresponding to eigenvectors via light pressure (for details see [35, 39]).

Photo chemistry Laser cooled ions are well isolated from their environment in the global confining potential. Their mean lifetime inside the trap is mostly limited by collisions with background gas. Elastic collisions lead to an impulse transfer to the trapped ion. In the case of weak confining potential, the ions might be pushed away from the stable trapping volume. Inelastic collision result in chemical reactions. Background gas, such as H_2, can react with Magnesium ions in the $P_{3/2}$ state of the ion [8, 9], like

$$Mg^{*+} + H_2 \rightarrow MgH^+ + H^*. \tag{2.14}$$

Reactions can also take place with water as reactant. Depending on the mass of the molecular ion, the reaction product can stay in the crystalline structure as Coulomb interaction leads to a sympathetic recooling. But the closed transition necessary to cool the ion and to reemit photons for detection does not exist any more. Recorded pictures of such crystals show the crystalline structure with an interruption. A non-fluorescing (dark) ion is incorporated in the periodic structure and it looks as if there is an ion missing.
Ions of different mass at the crystalline structure show interesting effects on the structure of the crystal. They might even interact with defects inside the periodic structure, as shown in [1, 40] and have to be investigated further.

2.2 Structural defects in Coulomb crystals

Laser cooled trapped ions form crystalline structures [7]. We are interested in crystalline structures, consisting of several tens of ions. Their shape depends on the properties of the trapping potential:

$$\Phi_{\text{Paul Trap}} = m\left(\omega_x^2\, x^2 + \omega_y^2\, y^2 + \omega_z^2 z^2\right). \tag{2.15}$$

It depends strongly on the individual set of parameters like the number of ions N and the characteristic trapping frequencies $\omega_{\{x,y,z\}}$ and is discussed in detail, e.g. in [42, 43]. In the case of $\omega_x \ll \omega_{\{y,z\}}$, ions form a linear chain, lowering one of the radial frequencies, the crystal undergoes a structural phase transition. We obtain a two dimensional structures of up to 50 ions, choosing $\omega_x \ll \omega_y < \omega_z$, with image

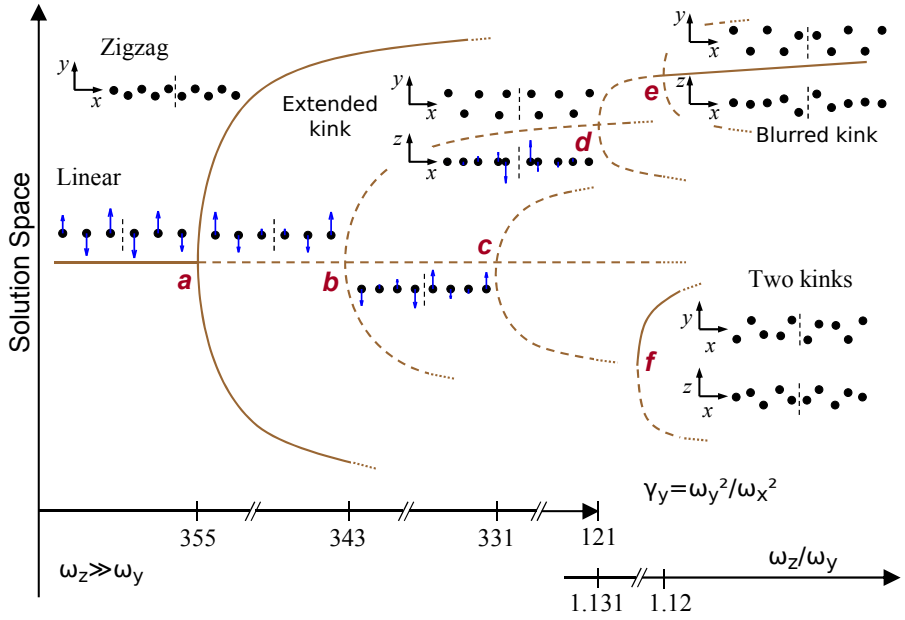

Figure 2.3: One- and two-kink configurations in a crystal of 50 ions. For ion crystals, there are two parameters, which we use to describe the dimensionality of the crystal: $\gamma_y \equiv \omega_y^2/\omega_x^2$ and ω_z/ω_y. On the left, we depict the transitions from a linear chain to planar zigzag and structures with kinks as γ_y is lowered, while $\omega_z \gg \omega_y$. On the right for fixed $\gamma_y = 121$, ω_z/ω_y is lowered. As indicated in the configurations (e) and (f) the ions forming the kink extend into the third dimension, as they leave the crystal plane. At each parameter value, there are many possible crystal configurations and only few of these are indicated in the figure, showing how they continuously depend on the parameters. The spatial configurations emphasizes the central part, where the kink is located. The black dashed line indicates axial symmetry of the crystal, and the arrows depict the direction and relative amplitude of ion motion in the normal mode of highest frequency, further details and the figure are published in [1].
The so called "Extended kink" is not stable for such large crystals. Whereas the "Blurred kink" is stable for long time, even for crystals of about 30 ions only. In crystalline structures of such a size even the "Extended Kink" is a stable configuration.

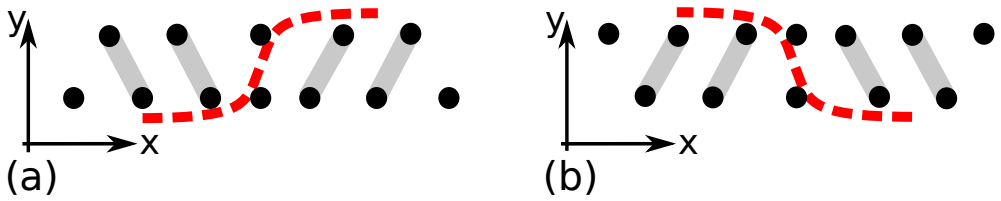

Figure 2.4: Schematics of a structural defects inside a Coulomb crystal.
Two mismatching domains at the center of the crystal form a topological protected structural defect. A dashed red line indicates the solution of the SG equation, see equation 2.17.
(a) A kink is depicted for a topological charge $\sigma = 1$. In the context of spin chains, it would be represented by $(\cdots \downarrow\downarrow\downarrow\uparrow\uparrow\uparrow\uparrow \cdots)$.
(b) The anti-particle of a kink a $\overline{\text{kink}}$ is depicted. It has a topological charge of $\sigma = -1$. Here the spin chain representation would be $(\cdots \uparrow\uparrow\uparrow\downarrow\downarrow\downarrow\downarrow \cdots)$.

and mirror image, labeled as zigzag and $\overline{\text{zigzag}}$. Properties of these structures are discussed in the following. In this chapter, we focus on the occurrence and properties of structural defects inside these Coulomb crystals as well as the spectrum of normal modes (phonons) for zigzag ($\overline{\text{zigzag}}$) as well as kinks ($\overline{\text{kinks}}$). First, theoretical predictions on structural defects in Coulomb crystals are published in [16, 17] and the experimental realization is shown in [6].

2.2.1 Occurrence and shape of structural defects

We study ion crystals with defects in the x-y-plane. The square of the ratio of radial to axial confinement $\gamma_y \equiv \omega_y^2/\omega_x^2$ is used to define the transition from a linear to a two dimensional crystal, as long as $\omega_z \gg \omega_y$ is valid. In numerical simulations, we start with a linear chain and continuously lower γ_y, undergo a structural phase transition and reach the parameter range of two dimensional structures, as shown for the representative case of 50 ions in fig. 2.3 [1]. At (a) the solution space splits in "Zigzag" and its mirror conformation "$\overline{\text{Zigzag}}$", both containing one domain only, of undisturbed periodicity. Further lowering γ_y, we obtain stable configurations containing structural defects, as shown in (d) and (e) [1, 2]. Via tuning γ_{y}, we can shape characteristic parameters of the kink.

In these configurations two mismatching domains occur in the same crystal. Zigzags can be written in the context of spin chains as: $(\cdots \downarrow\downarrow\downarrow\downarrow\downarrow\downarrow\downarrow\downarrow \cdots)$, whereas a $\overline{\text{Zigzag}}$ as $(\cdots \uparrow\uparrow\uparrow\uparrow\uparrow\uparrow\uparrow\uparrow \cdots)$. Two mismatching domains in the same ion crystal lead to a configuration like: $(\cdots \uparrow\uparrow\uparrow\uparrow\downarrow\downarrow\downarrow\downarrow \cdots)$ which is a structural defect, a so called kink. A single mismatch in the pattern would be illustrated as $(\cdots \uparrow\uparrow\uparrow\uparrow\downarrow\uparrow\uparrow\uparrow \cdots)$. In contrast to the topological protected defects, only one spin mismatches the pattern.

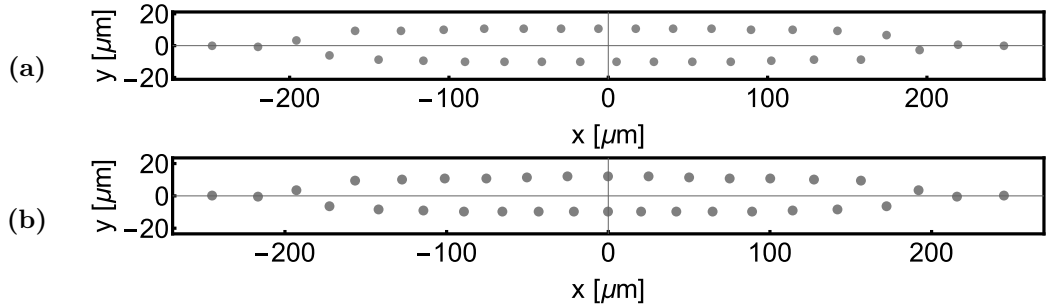

Figure 2.5: Comparing numerical results of ion crystal configurations consisting of 34 ions (gray discs) confined in the harmonic potential of linear Paul trap.
(a) The periodic configuration, labeled as $\overline{\text{Zigzag}}$, shows the configuration of minimal energy, the energetic ground state. A rotation of 180° with respect to the crystal's x-axis, a mirror image, is labeled as Zigzag.
(b) An ion crystal contains a defect, here a so called extended structural defect, which results in two ions on the vertical axis at the center of the crystal. These defects are created by two mismatching subdomains referrec to as "kinks". The mirror image is labeled as $\overline{\text{kink}}$. As depicted, the kink coordinate is $\vec{\mathcal{K}}(x,t) = 0$, see eq. 2.18.

Structural defects as kinks - topological solitons

Structural defects form domain walls inside crystalline structures. A kink moves inside the crystal, when the domain wall moves along the axis of weak confinement ($\cdots\uparrow\uparrow\uparrow\uparrow\uparrow\downarrow\downarrow\cdots$). If two mismatching domains are created during a non-adiabatic phase transition from the gas phase to the crystalline phase, a topological protected defect is created. The assumption of a non-adiabatic phase transition is valid, as long as the relevant timescale is short compared to the inverse of the given eigenfrequency of the harmonic oscillator potential along the axial direction $2\pi/\omega_x$, related to the speed of sound. Another approach is a so-called "quenching" of the trapping potential on similar timescales as needed for a laser induced phase transition, shown by [6, 22, 23]. Strictly speaking, a topological protection is perfect, only if the crystal was of infinite size or had periodic boundary conditions, like a circular shaped crystal [44, 45].

Periodic one dimensional systems can be described by the sine-Gordon-equation (SG), for details see [41].

$$\frac{\partial^2 u(x,t)}{\partial t^2} - \frac{\partial^2 u(x,t)}{\partial x^2} + \sin(x) = 0, \tag{2.16}$$

where u is the coordinate of a particle upon the periodic potential. There are three types of excitations as solution of a general system described by the SG: phonons, kinks and breathers. In ion crystals, phonons and kinks are relevant. Phonons are global excitations of the system as a whole, the quantized excitation of the vibrational eigenmodes as discussed in the following. Kinks are static, non-perturbative excitations related to the structural defects as discussed before. They show a localization of the

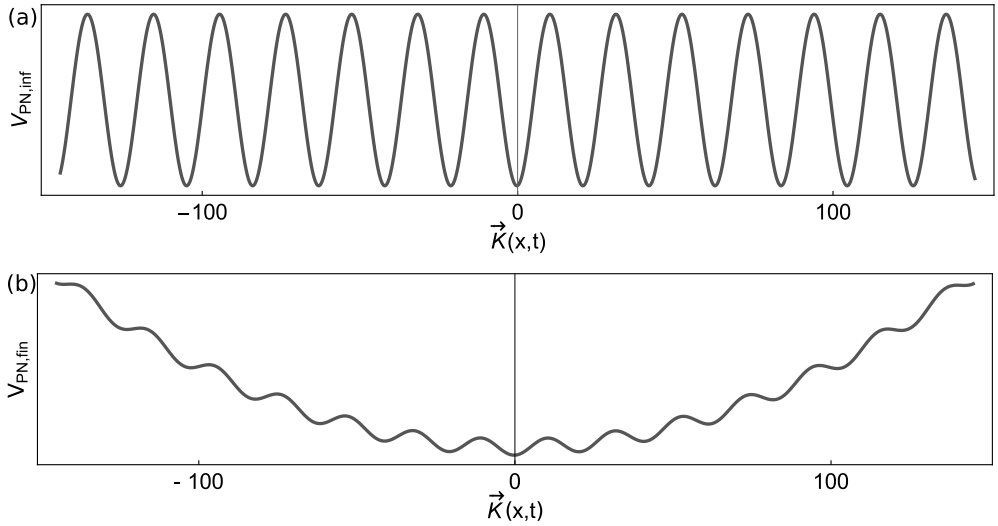

Figure 2.6: Schematics of the Peierls-Nabarro (PN) potential dependent on the size of the system as function of the kink coordinate $\vec{\mathcal{K}}(x,t)$ depending on N and $\omega_{\{x,y,z\}}$.
(a) The PN potential is sinusoidale for systems of infinite size, $N \to \infty$ [41].
(b) As the system is of finite size, there is an additional finite potential superimposed, that can be averaged to a harmonic shape, see fig. 2.7.

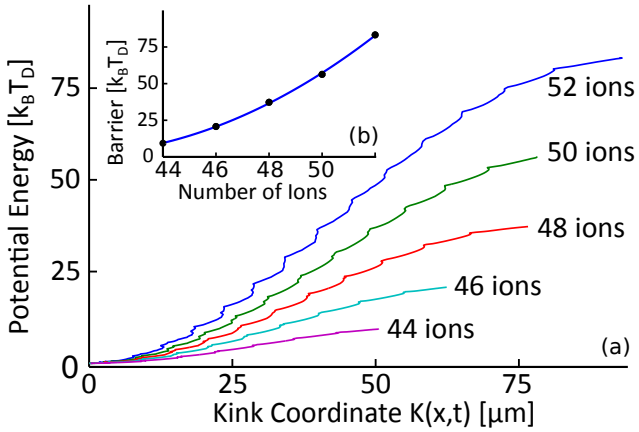

Figure 2.7: Numerical simulation of the effective Peierls-Nabarro (PN) potential energy of a kink dependent on its distance from the center of the Coulomb crystal, defined by its coordinate $\vec{\mathcal{K}}(x,t)$, see eq. 2.18.
(a) The potential depth is calculated for a so called "Blurred Kink", as shown in [2] (parameter range is in fig. 2.3 at point (e)). The potential is symmetric about the trap center and reaches its maximum roughly at the extremal values shown (dependent on the total ion number).
(b) The kink escapes its self induced trapping potential by reaching the sides is given in dependence of the number of ions, fitted by a quadratic function (blue line) [2].

vibrational eigenmode to the few ions forming the periodicity breaking defect. The position of a defect in axial direction is given by the solution of the SG equation

$$\vec{\mathcal{K}}(x,t) = 4 \arctan\left(e^{-\sigma\,\gamma(\dot{x})\,(x-\dot{x}\,t)}\right) \tag{2.17}$$

and depends on its topological charge σ and the kink's velocity in axial direction $\dot{x}$. $\gamma(\dot{x})$ is the Lorentz contraction $\gamma(\dot{x}) = 1/\sqrt{1-(\dot{x}/c)^2}$ as the SG equation is relativistic invariant. The topological charge indicates, whether the solution is labeled as kink ($\sigma = +1$, see fig. 2.4 (a)) or as anti-kink ($\overline{\text{kink}}$, $\sigma = -1$, see fig. 2.4 (b)).

In the case of crystals with finite size, the kink is only a quasi topological protected and anneals, if it is translated along the x-axis to the edge of the crystal. As this is a discrete effect related to the domain wall, there is no dispersion in the localization, even a change in γ does not influence the prescence of the kink, only its shape.

Structural defects fulfill the properties of discrete solitons: localized, topological protected and non-perturbative [46]. Further details are discussed in [47] and references therein, such as [14].

Kink coordinate

We want to investigate the dynamics of defects, for the representative case of the "Extended Kink" in fig. 2.5 (b). Dynamics of the defect are limited by the extension of the crystalline structure in one dimension, the axial direction x of finite length. The kink can move along this single degree of freedom. Therefore it is appropriate to define the kink's position inside the crystal relative to the axial coordinates. We use the approach by H. Partner et al. [40], determining the position $\vec{\mathcal{K}}(x,t)$ of the "Extended kink" as the point of maximal deviation of comparing zigzag and a kinked crystal in axial direction

$$\vec{\mathcal{K}}(x,t) = \frac{\sum_{j}^{N-1} \langle x\rangle_j (t) \left[\psi\left(\langle x\rangle_j, t\right) - \psi^{(Z)}\left(\langle x\rangle_j^{(Z)}\right)\right]^2}{\sum_{j}^{N-1} \left[\psi(\langle x\rangle_j, t) - \psi^{(Z)}\left(\langle x\rangle_j^{(Z)}\right)\right]^2}. \tag{2.18}$$

$\langle x\rangle$ is the mean distance between two neighboring ions, while $\psi\left(\langle x\rangle_j\right) = x_{j+1} - \langle x\rangle_j$ as the distribution of the mean distance of all j ions in axial direction and $\langle x\rangle_j = (x_{j+1} + x_j)/2$. $\psi^{(Z)}\left(\langle x\rangle_j^{(Z)}\right)$ denotes the distances of the ions in a periodic zigzag crystal. It is introduced to remove contribution that are related rather to deviations from the assumed trapping potential than the presence of the kink. This definiton is valid as long as there is a difference in the amount of ions in the upper and the lower ion chain inside the Coulomb crystal, which is fulfilled by our types of kinks, see fig. 2.5 (b). Thus, we can calculate the kink's center and coordinate, respectively in each crystalline

structure. The velocity of a kink $\dot{\vec{\mathcal{K}}}(x,t)$ is defined by

$$\dot{\vec{\mathcal{K}}}(x,t) = \frac{\vec{\mathcal{K}}(x,t) - \vec{\mathcal{K}}(x,t+\Delta t)}{\Delta t}, \tag{2.19}$$

where Δt is the difference in time between two succeeding measurements of the crystalline structure.

Peierls-Nabarro potential

In theoretical descriptions, the Peierls-Nabarro (PN) potential is of infinite size [41] and is sinusoidal on the length scale of the lattice constant, see fig. 2.6 (a). Even in experimental realizations for appropriate trapping parameters, defects are stable for long time, compared to the natural timescales relevant for the crystal: $\tau \gg \frac{1}{\Omega_{\mathrm{RF}}} \gg \frac{1}{\omega_{\mathrm{sec},i}}$. They create their own self induced trapping potential inside the crystalline structure. The PN potential considering finite size effects confines the kink at the center of the crystal. The finite size of our system combines the periodic potential with an additional quasi-harmonic potential, as shown in fig. 2.6 (b). The depth V_{PN} depends on all parameters especially on the size of the crystal, see fig. 2.7 from [2]. We might explain this by a simple picture: One defect can only leave the crystal if one half of the structure finally appears as "flipped" to the pattern matching the other half of the crystal. In a crystal of finite size, only a finite number of ions have to change their position. In addition, the global trapping potential of the Paul trap affects the depth of the PN potential [35].

We experimentally study the occurrence of such defects and published first time systematic results in [2]. Therein we analyzed the occurrence of defects in dependence on the number of ions of these crystals for a dedicated confining potential.

In the following, crystals of the size of 34 ions are discussed. Numerical studies reveal two crystal configuration, as shown in fig. 2.5, a Zigzag and a two domain crystal.

2.3 Internal degrees of freedom of an ion crystal

The N ions of a Coulomb crystal are confined in a superposition of the trapping and the Coulomb potential $V = V_{\mathrm{trapping}} + V_{\mathrm{Coulomb}}$ and have $3N$ degrees of freedom (DoF), further details are described in [49–51]. There are center of mass and rotational motion, so there remain $(3N-6)$ internal DoF. Considering only small oscillations around equilibrium positions, we can Taylor expand the potential up to second order:

$$V = V_0 + \sum_{i}^{3N-6} \left.\frac{\partial V}{\partial x_i}\right|_{x_i=0} x_i + \frac{1}{2} \sum_{i,j}^{3N-6} \left.\frac{\partial^2 V}{\partial x_i\, \partial x_j}\right|_0 x_i\, x_j + \dots \tag{2.20}$$

We choose the global minimum of the potential to be 0 and assume that the internal dynamics can be described by small oscillations. The sum of kinetic (E_{kin}) and potential

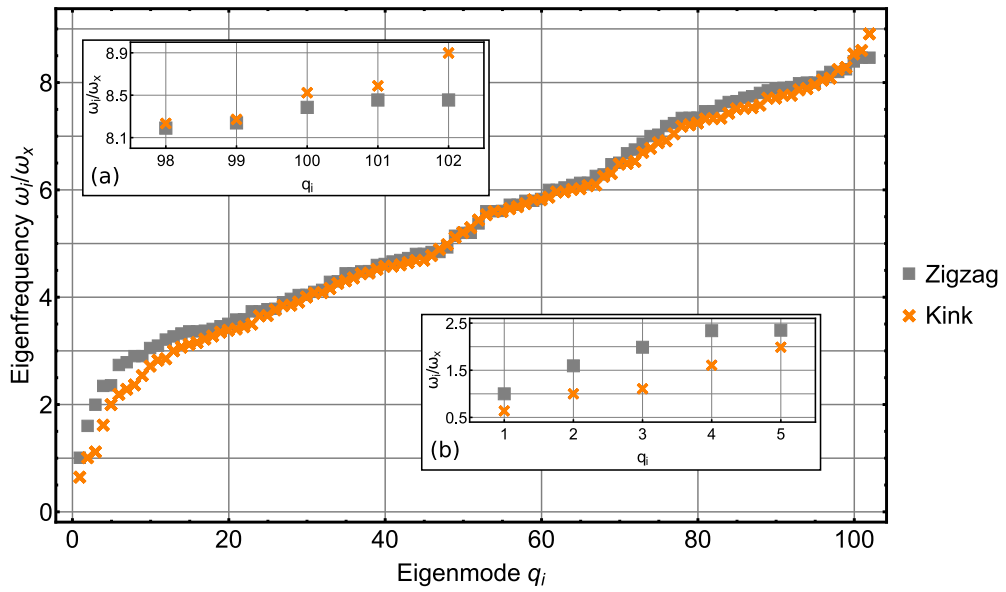

Figure 2.8: 102 normalized motional eigenfrequencies of an ion crystal consisting of 34 ions in a harmonic confining potential. The numerical calculation is done with a code provided by H. Landa [1, 48]. The grey squares represent the frequencies of a periodic zigzag structure, the orange crosses frequencies of a kink containing structure. The eigenfrequencies of both structures deviate most in the high and low frequencies range, emphasized in the insets:
(a) Mode ω_{100} - ω_{102} are shifted in the high frequency spectral range of the crystal with kink compared to the zigzag configuration.
(b) The defect containing crystal has an eigenfrequency shifted below the axial COM-mode (mode q_2 of the kinked crystal), scetched in fig. 2.9 (c).

energy V of the system can be written as

$$E_{\text{tot}} = E_{\text{kin}} + V = \frac{1}{2}\sum_{i}^{3N-6} m_i \dot{x}_i^2 + \frac{1}{2}\sum_{i,j}^{3N-6} \frac{\partial^2 V}{\partial x_i \, \partial x_j}\bigg|_0 x_i \, x_j \tag{2.21}$$

where m_i denotes the mass of each particle with its velocity $\dot{x}_i = \frac{\partial}{\partial t} x_i$. The coordinates are rescaled with the mass of the ions $x_{m,i} = \sqrt{m_i}\, x_i$. In our case all ions have the same mass. The Hessian Matrix $\overline{\overline{K}}$ is defined as

$$K_{ij} = \frac{\partial^2 V}{\partial x_{m,i} \, \partial x_{m,j}}\bigg|_0 . \tag{2.22}$$

Rewriting 2.21 in the new coordinates

$$E_{\text{tot}} = \frac{1}{2}\sum_{i}^{3N-6} \dot{x}_{m,i}^2 + \frac{1}{2}\sum_{i,j}^{3N-6} K_{ij} \, x_{m,i} \, x_{m,j} \tag{2.23}$$

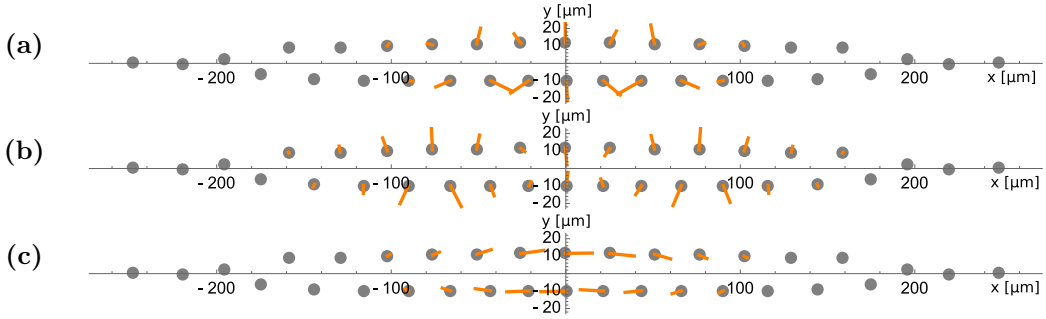

Figure 2.9: Numerically derived 34 ion crystal confined in a linear Paul trap with $\omega_{\{x,\,y,\,z\}} = \{1, 6.0, 7.5\}\,\omega_x$ incorporating a structural defect.
Numerically obtained ion positions (gray discs) in harmonic confinement and characteristic vibrational eigenmodes of the ion crystal containing a kink. Each ion's motional amplitude is drawn as a orange lines. Length indicates relative amplitudes and direction the motional phases, as all arrows are magnified by the same ratio for illustrative reasons.
(a) Eigenmode q_{100}: mainly radial contributions to the movement profile. Both ion chains move in radial direction out of phase.
(b) Eigenmode q_{97}: contains 2 knots symmetrical to the y-axis with mainly radial movement contributions. The projection of the eigenvector to the ions delivers motional amplitudes for each ion. The upper ion chain can be seperated into three region: The outer parts move in phase, whereas the centre part is shifted π out of phase. The motional direction of the lower chain is shifted by π with respect to the upper chain.
(c) Eigenmode q_1: mainly axial contributions to the movement profile, which could be described as an axial sliding mode, which allows for an axial motion of the kink. The axial position is defined by $\vec{\mathcal{K}}(x,t)$.

oscillatory motions are coupled in the basis of these coordinates. The matrix $\overline{\overline{A}}$ diagonalizes $\overline{\overline{K}}$:

$$\overline{\overline{A}}^{-1}\,\overline{\overline{K}}\,\overline{\overline{A}} = \overline{\overline{\Omega}} \tag{2.24}$$

The eigenvalues of $\overline{\overline{\Omega}}$ determine the square of the eigenfrequencies ω_i.

The vectors derived by

$$\vec{q} = \overline{\overline{A}}^{-1}\,\vec{x}_m \tag{2.25}$$

are called the normal coordinates of the system.
We can describe the dynamics of the ion crystal in the basis of the eigenmodes.

Beside the change in pattern of the ions' positions, a structural defect influences the eigenmode spectrum, as shown in fig. 2.8. The eigenmodes are sorted based on their eigenfrequencies and for comparison the ω_i of a zigzag crystal (gray squares) and a kink containing crystal (orange crosses) are shown. In most parts of the eigenfrequency spectrum there are differences due to the presence of the kink. In high frequency

$q_{100} - q_{102}$ and the low frequency spectral range q_1, there are significant deviations, as the spectral range is extended due to the presence of the kink. Some of these vibrational eigenmodes are shown in fig. 2.9. In (a) q_{100} and (c) q_1 only few ions contribute to the eigenmode, whereas in (b) almost all ions oscillate, if eigenmode q_{97} is excited. q_{100} can be described as radial breathing mode and q_1 as axial sliding mode. The localization of the mode in the presence of the kink can be used for several aspects, e. g., individually addressing of a quasi-particle, especially in the context of quantum simulation and quantum information processing, as discussed in [16, 17] and [52].

2.4 Dynamics of discrete solitons

Properties of structural defect allow to handle it analogue to a discrete soliton, a quasi-particle inside the crystal. Dynamical aspects like diffusion inside the crystal and the viscosity of the system will be discussed in this section. In the last paragraph, the well established model of Kramers [29] is introduced to describe the escape dynamics out of a potential well and adopt it to our system of a kink inside a Coulomb crystal. The motion is damped due to the prescence of the laser cooling.

2.4.1 Brownian motion

Following the discussion above, structural defects can be interpreted as quasi-particles. Brown discovered in 1827 the intrinsic motion of particles in a solvent [53]. Einstein, Smoluchowski and Langevin [54, 55] derived in the beginning of the 20th century the dependency on time t of the mean quadratic distance from the starting point in a system based on Brownian motion:

$$\left\langle \vec{\mathcal{K}}(x,t)^2 \right\rangle = 2\,D\,t \tag{2.26}$$

where D is the diffusion coefficient of the particle inside the solvent and can be calculated by the Stokes-Einstein-Equation:

$$D = \frac{k_\mathrm{B}\,T}{6\,r\,\pi\,\xi} \tag{2.27}$$

with temperature T, the radius of the particle r and ξ the viscosity of the solvent. We study ion crystals initialized in thermal equilibrium near the Doppler cooling limit. In our case the position of the domain wall is described by $\vec{\mathcal{K}}(x,t)$ and given by the motion of the ions inside the crystalline structure.

2.4.2 Dynamics of indistinguishable particles

The ion crystal consists of N ions of the same species. Ions are laser cooled along axial direction to the milli-Kelvin regime. There is no tracer to resolve dynamics of

an individual ion in the crystalline structure. Incorporating a different isotope or a molecular ion, we can identify the trajectory of a single ion inside the ion crystal. However this would influence our eigenmode spectrum as it shifts the eigenfrequencies and changes the motional profiles.
In our case, the ions are specially separated but indistinguishable particles, i.e. we are not yet able to resolve, whether two neighboring ions interchanged their position on any timescales.
Diffusion in systems of identical particle is refered to as "self diffusion" [56, 57]. Relevant time scales and the viscosity $\xi_{\mathcal{K}}$ depend on the temperature T of the system. They can be derived by the relation of Green and Kubo [58, 59], in dependence on the velocity auto correlation function (vACF) derived from the time derivative the kink coordinate. In a system with high viscosity the velocities are damped on short timescales, so the dot product of $\dot{\vec{\mathcal{K}}}(x,t,T)\,\dot{\vec{\mathcal{K}}}(x,t+\Delta t,T)$ decays to zero. The viscosity of such systems can be described by the following formular:

$$\xi_{\mathcal{K}}(T) = \rho_{\mathrm{IC}} \int_0^\infty \left\langle \dot{\vec{\mathcal{K}}}(x,t,T)\,\dot{\vec{\mathcal{K}}}(x,t+\Delta t,T) \right\rangle dt \tag{2.28}$$

where $\dot{\vec{\mathcal{K}}}(x,t,T)$ is the discrete time derivative of the kink coordinate for a certain temperature T and $\langle\rangle$ indicates the time average. ρ_{IC} gives the density of the ion crystal.

The viscosity within an ion crystal strongly depends on its internal temperature. There are at least two approaches to describe this dependency. One is published by Raman and Andrade [60, 61], called the Arrhenius-Andrade model:

$$\xi_{\mathcal{K}}(T) = \xi_0 e^{b/T} \tag{2.29}$$

where ξ_0 can be interpreted as the intrinsic viscosity of the system and b as material constant. These models have been originally introduced for liquids, like water or ethanol.
Another approach is to model the temperature dependency [62] by:

$$\xi_{\mathcal{K}}(T) \propto T^{-\alpha/2}, \tag{2.30}$$

where α takes the dimensionality of the system into account. In our case the kink can only move along the axial direction of the crystal, that is, it is limited to one dimension. In this case the temperature dependency might be described by the $T^{-1/2}$.
Both models are discussed in comparison with the data to reveal, which approach might be suited best to incorporate the temperature dependency of the viscosity into the Kramers' model.

Any energy transfer to the system leads to motion of the kink at its lattice site or even its propagation to the next one in the Peierls-Nabarro (PN) potential V_{PN}, see fig. 2.7. We have to distinguish between a kink moving to the neighboring local potential minimum, a lattice constant apart, and a kink leaving the finite PN potential, as reaches

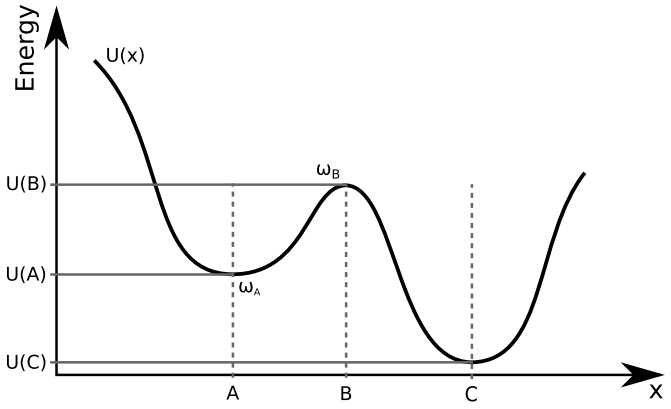

Figure 2.10: One dimensional energy landscale with a energy barrier at B on the x-axis. Kramers model describes the timescale, a particle located in A needs to overcome the energy barrier $U(\mathrm{B})$ in dependency on the viscosity and the temperature of the bath. To calculate the mean time for the passage in the regime of strong viscosity, the curvature $\omega_\mathrm{A} \propto \frac{\partial^2}{\partial x^2} U(x)\big|_{x=\mathrm{A}}$ to the left and the curvature at the transition state $\omega_\mathrm{B} \propto \frac{\partial^2}{\partial x^2} U(x)\big|_{x=\mathrm{B}}$ are relevant.
The energy $U(\mathrm{C})$ represents the energetic groundstate within the potential energy landscape. In the context of the crystalline structures, this can be interpreted as the energy of a Zigzag, the periodic crystalline structure without a defect. The energy difference $U(\mathrm{B}) - U(\mathrm{C})$ can be derived by numerical studies and amounts to about $40\, k_\mathrm{B}\, \mathrm{T_D}$.

the edge of the crystal. In the following, we focus on the latter, the kink vanishing from the finite two dimensional region of crystal to the outer linear part.

2.4.3 Kramers' escape model

Kinks are quasi bound to the crystals and have to overcome a barrier $E_\mathrm{B} = U(\mathrm{B}) - U(\mathrm{A})$, see fig. 2.10. Thus, the motional excitation of the defect inside the crystal is interpreted in the context of reaction-rate theory [63]. Relevant timescales are described by the reaction rate k, described by the Arrhenius law

$$k \propto e^{-\frac{E_\mathrm{B}}{k_\mathrm{B}\, T}}. \tag{2.31}$$

Hendrik Anthony Kramers derived in 1940 a relation for the escape time of a particle from a thermal bath inside a one dimensional potential [29]. The model is based on the assumption, that a particle can only escape via a single barrier of height E_B and gets trapped in a second potential well, which is lower in energy than the initial one. Damping leads to a stabilization of the system.
The timescale depends on the viscosity of the system. Kramers derived two solutions for the problem, one in the case of small and one for large viscosity. In both cases, there is the Arrhenius factor, see eq. 2.31, whereas the prefactor differs. In our realization the

structural defect is stable for long time ($\approx 2.7\,\mathrm{s}$, [35]) at the place of minimal energy, labeled with A, which corresponds to the kink coordinate $\vec{\mathcal{K}}(x,t,T)=0$. Here we focus on Kramers derivation for the strong viscosity and assume the motion of the kink to be overdamped. In this case the Kramers' rate is given by [29]:

$$k = \frac{\omega_\mathrm{A}\,\omega_\mathrm{B}}{2\,\pi\,\xi} e^{-\frac{E_\mathrm{B}}{k_\mathrm{B}\,T}}, \tag{2.32}$$

where $\omega_\mathrm{A} \propto \frac{\partial^2}{\partial x^2}U(x)\big|_{x=\mathrm{A}}$ the curvature at the centre and $\omega_\mathrm{B} \propto \frac{\partial^2}{\partial x^2}U(x)\big|_{x=\mathrm{B}}$, as shown in fig. 2.10. $\omega_\mathrm{B} \geq 0$ in the transition state approach, as used by H.A. Kramers. ξ is interpreted as the viscosity of the Coulomb crystal. Latter depends on the temperature of the laser cooled ion crystal, see eq. 2.28.
The energy landscape can be interpreted in the context of the ion crystal and the Peierls-Nabarro potential. So B represents the outermost stable position of a kink closest to the crystal edge inside the PN potential. The minimum of $U(x)$ in A can be identified as the configuration with the kink located at the centre of the crystal. The curvature is given by ω_A and reflects the local shape of the PN potential $\omega_\mathrm{PN}(\mathrm{A})$.
The barrier height can be estimated by $E_\mathrm{B} = U(\mathrm{B}) - U(\mathrm{A})$. The depth of the PN potential E_PN is given by the barrier height E_B. So the rate to escape from the PN potential is given by

$$k_\mathrm{PN} = \frac{\omega_\mathrm{PN}\,\omega_\mathrm{B}}{2\,\pi\,\xi(T)}\, e^{-\frac{E_\mathrm{PN}}{k_\mathrm{B}\,T}}. \tag{2.33}$$

Inside the PN potential, the kink can move in both directions to the left and to the right and escape from the crystal, thus an extension of the model is required. So there is a second exit channel in contrast the original Kramers energy landscape. We assume, that this increases the escape rate by a factor of two, as to first order, the PN potential is symmetric.

We have no direct experimental access on the shape of the PN potential, but we can measure mean lifetimes. The mean lifetime τ_PN is the invers of the escape rate k_PN, as given in the following:

$$\tau_\mathrm{PN} = \frac{1}{2}\cdot\frac{2\,\pi\,\xi(T)}{\omega_\mathrm{PN}\,\omega_\mathrm{B}} e^{\frac{E_\mathrm{PN}}{k_\mathrm{B}\,T}}, \tag{2.34}$$

as the shape of the potential is constant. ω_PN can be identified as the eigenfrequency of eigenmode q_1. So we can rewrite eq. 2.34 to

$$\tau_\mathrm{PN} = \frac{\pi\,\xi_\mathcal{K}(T)}{\omega_1}\,\frac{e^{\frac{E_\mathrm{PN}}{k_\mathrm{B}\,T}}}{\omega_\mathrm{B}}. \tag{2.35}$$

$\xi_\mathcal{K}(T)$ can be derived by the relation given in equation 2.28. There are still two parameters to be determined: In the following, we exploit our experimental data to derive the barrier height E_PN as well as the outermost curvature of the PN potential ω_B.

Chapter 3

Experimental setup and molecular dynamics simulation

In the chapter before, the theoretical background of our experiments is described that we want to carry out. Here I short summary on the experimental setup is given to introduce our excitation methode and explain in detail, how we analyse our camera pictures. For numerical studies, we use a molecular dynamics code, which will be described at the end of this chapter.

3.1 Ion trap apparatus and laser system

The linear radiofrequency ion trap is part of a 45 cm long RF-guide housed in a vacuum chamber, for details see [8, 9]. It has been set up in three parts separated by differential pumping stages. Additional ring shaped DC-electrodes segment the radial symmetry of the RF-guide to generate local potential wells. There is an additional electrode next to the trap used for the experiments to apply additional DC, as well as AC electric fields, see [35]. The experiments were carried out in the experimental part of the trap in chamber 3, see fig. 3.1.
As the vacuum chamber is constructed around a U-shaped RF-guide, there is only limited optical access along the trap axis. In addition small window flansches, long distance apart from the experimental trap limit the focal strength of the laser cooling beam at the trap.
The vacuum chamber has been used in the past to optically trap Barium ions in radial direction. For this, the optical access has been improved at several points [64, 65]. The counter-propagating electron beam source has been removed, used in former times to ionize the atoms via electron scattering. In addition, the lid of the oven has been removed to avoid scattering and charging of surfaces caused by the optical trapping beam.

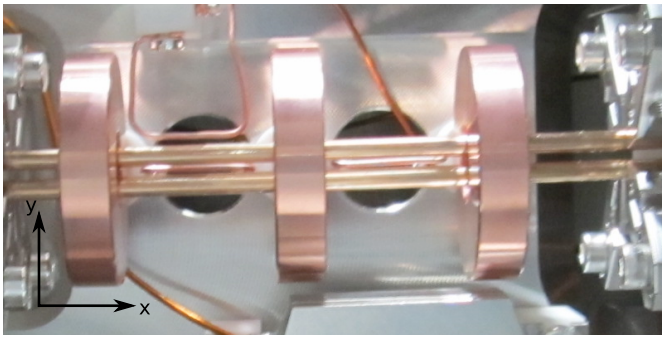

Figure 3.1: View in camera perspective on our Paul trap. It is located inside a ultra-high vacuum chamber, to protect the ions from the surroundings. The four goldplated rods are a part of the RF-guide. Three cylindrically shaped copper plates are 2 cm apart from each other and ensure the confinement in x-direction along the RF-guide. The wire electrode above the rods is removed to improve optical access to the left trap, the experimental trap. To the right the loading trap is located directly above the oven.

An homebuild oven heats a small piece of Magnesium to create a hot cloud of atoms next to the trapping volume. There are three Magnesium isotopes, but we are only interested in $^{24}Mg^{+}$.
Philip Kiefer and myself planned and setup the whole laser beamline consisting of two laser sources, frequency doubling stages and several acusto-optical modulators [35]: We use a resonantly frequency doubled C-Wave [66], based on an optical parametrical oscillator [67], pumped by a solid state laser to photoionize Magnesium atoms at the appropriate wavelength (285 nm). As the atoms are ionized from a hot cloud of ions, the unstabalized C-Wave provides stable loading rates for several hour. The ions are Doppler cooled on the $S_{1/2} \leftrightarrow P_{3/2}$ transition (280 nm) with a quadrupled fiberlaser (1118 nm) (further called BD). BD is used as an abbreviation for "blue doppler" as the electronic transition is higher in energy than the $S_{1/2} \leftrightarrow P_{1/2}$. It is stabilized in frequency by a Doppler free Iodine spectroscopy and detuned red ($\delta \approx -\Gamma/2 = -2\pi \cdot 42\,\mathrm{MHz}/2$) to the atomic transition, see equation 2.12. The BD laser frequency can be shifted by a double passed acousto-optical modulator (AOM) and its cooling power can be tuned up to $140\,\mu\mathrm{W} \mathrel{\widehat{=}} 0.035\,I_{sat} = 0.035 \cdot 2550\,\mathrm{W/cm^2}$). During the experimental sequence the crystal is melted to an ion cloud by the blue shifted BD laser ($\delta \approx +\Gamma/10$) BD_{bl} with respect to the atomic transition and gets recooled with BD at $\delta \approx -\Gamma/2$. An additional permanently running red detuned ($\delta \approx -10\,\Gamma$) cooling laser (BDD) ensures that ions do not get lost from the trap volume. Further details on the laser system are described in [35].
The fluorescence light of the laser cooled ions is detected on a charged-coupled device (CCD) camera to obtain structural information of the ion crystal inside the Paul trap. A camera pixel of 6 μm length corresponds to 1.3 μm distance in the trap. Based on a home build National Instruments LabView interface [65], we are able to control all

relevant parameters during the experimental sequence. Further details like the relevant measurements to characterize the laser system and the Paul trap are described in detail in [35]. Inside the vacuum chamber, we can trap laser cooled ions, shape the crystal via trapping potential and record pictures, as shown for instance in fig. **??** (a).

3.2 Amplitude modulation of the RF

In this thesis, we present experiments based on a frequency selective quadrupol field excitation of vibrational eigenmodes of an axial laser cooled ion crystal. To generate such an electric field, we use the radial trapping electrodes, see fig. 3.1, as they are arranged in quadrupol configuration. For this purpose, we had to modify the control of the amplitude of our trapping amplitude U_{RF}. Therefore we add the output voltage of an arbitrary waveform generator $U_{\mathrm{mod}}(t)$ via a capacitor to the control voltage of the amplitude modulation input of our radiofrequency generator[1].

3.2.1 Tuning the secular frequencies via DC amplitude modulation

First, the influence of a constant voltage is scetches, as we apply it to the modulation input of our radiofrequency generator. 34 $^{24}\mathrm{Mg}^{+}$ ions are confined in a linear Paul trap, consisting of four radiofrequency rods with a RF drive $\Omega_{\mathrm{RF}} = 2\pi\ 5.84\,\mathrm{MHz}$ and two ring electrodes, providing a radial, respectively axial trapping potential. As introduced in eq. 2.7 and eq. 2.8 the secular frequencies depend on the amplitude of the trapping potential $U_{\mathrm{RF},0}$. Amplying a constant voltage U_{mod}, we can increase or decrease the curvature of the trapping potential. As the shape of the potential defines the eigenfrequencies /-modes of the ion crystal, we try to keep them as constant as possible during the experiment. With an additional electrode parallel to the RF-electrodes, we lift the radial degeneracy applying a DC voltage.
To measure the radial secular frequencies, we use the following approach: The real time observation via our camera[2] enables us to selectivly detect a motional excitation of the ion crystal. This is prominent when we tune the excitation frequency to the resonance of the secular frequency. As we scan the applied frequency and reduce the amplitude to become more sensitive on resonance, we can resolve the eigenfrequencies with an inaccuracy of several ten Hz. The AC voltage is applied to the electrode behind the trap, as shown copper wire between the goldplated rods in fig. 3.1. In axial direction, the overlap of electric field vector and eigenmode vector is to small to achive reasonable frequency selectivity. Thus, we use an intensity modulation of the axial cooling laser to drive the motional excitation of the axial secular frequency. This is described in detail in [35]. The axial secular frequency is $\omega_{\mathrm{x}}/(2\,\pi) = (38.2 \pm 0.5)\,\mathrm{kHz}$ and the radial secular

[1] Rohde & Schwarz, SMG B1
[2] PCO, DicamPro

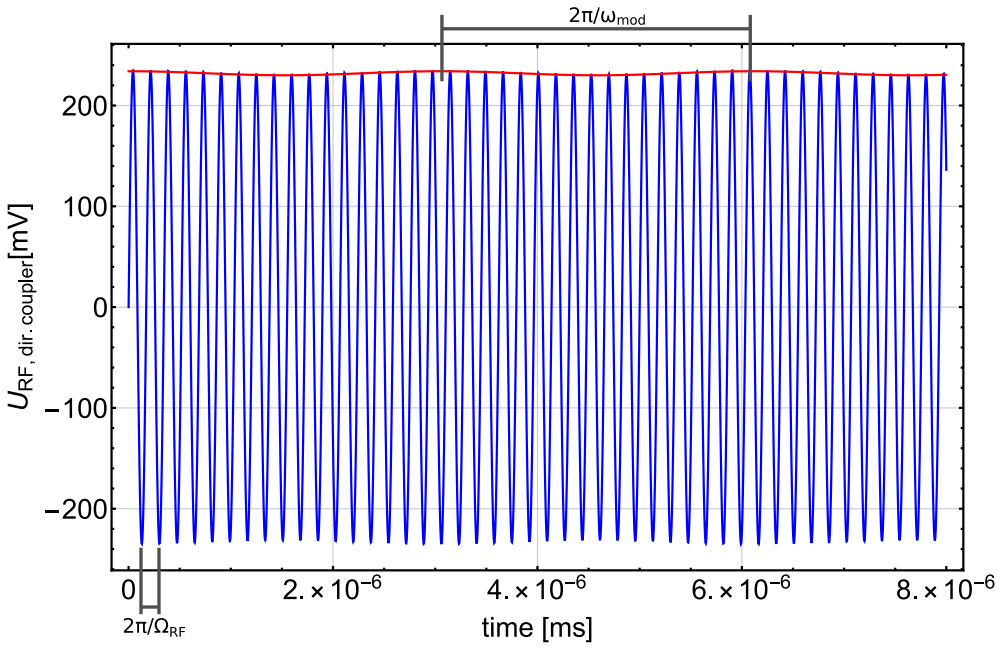

Figure 3.2: Beating signal measured in front of the helical resonator. We record the signal reflected by the helical resonator at a directional coupler with an oscilloscope. The beating signal (blue line) represents the recorded trace. As we know the modulation frequency of $\omega_{\mathrm{mod}} = 2\pi\,327\,\mathrm{kHz}$, we can measure the amplitude of the modulation (red line). Taking the frequency selectivity of the helical resonator into account, we can calculate the modulation depth η as the ratio of U_{mod} and U_{RF}.

frequencies are $\omega_{\{\mathrm{y,\,z}\}}/(2\,\pi) = \{(232.3 \pm 0.2), (293.0 \pm 0.3)\}\,\mathrm{kHz}$. The errorbars indicate the uncertainty within the whole set of data, that is taken into account in this thesis. Individual dataset have smaller uncertainties of the secular frequencies. To generate comparable sets of data, we use the DC voltages to tune the eigenfrequencies of the ion crystal to the level of 0.1 kHz.

These single ion secular frequencies result for a crystal consisting of 34 ions to a spectrum of 102 normalmodes (see fig. 2.8) with a range in frequency for the zigzag $\omega_i^{\mathrm{zigzag}} \in 2\pi\,\{38\,\mathrm{kHz}, \ldots, 328\,\mathrm{kHz}\}$ and the kink containing crystal $\omega_i^{\mathrm{kink}} \in 2\pi\{23\,\mathrm{kHz}, \ldots, 345\,\mathrm{kHz}\}$.

3.2.2 Modulation of the RF trapping potential with sidebands

The aim of this thesis is to perform spectroscopy of eigenmodes of the ion crystal. We will study eigenfrequencies $\omega_i/(2\,\pi)$ between 300 und 350 kHz with mainly radial motional profile, see fig. 2.9. Therefore we modulate the amplitude $U_{\mathrm{RF},\,0}$ of the RF-field with a frequency $\omega_{\mathrm{mod}}/(2\pi)$ in this range. In the case of constant modulation

voltage U_{mod}, the RF-voltage can be described by

$$U_{\mathrm{RF},\,0} = [U_0 + U_{\mathrm{mod}}]\,\sin(\Omega_{\mathrm{RF}}\,t) \tag{3.1}$$

Adding a timedependent voltage, the RF-voltage is modified to

$$U_{\mathrm{RF}}(t) = [U_0 + U_{\mathrm{mod}}\sin(\omega_{\mathrm{mod}}\,t)]\sin(\Omega_{\mathrm{RF}}\,t)\,. \tag{3.2}$$

We can rewrite this as

$$\begin{aligned} U_{\mathrm{RF}}(t) = {} & U_0\sin(\Omega_{\mathrm{RF}}\,t) \\ & + \frac{U_{\mathrm{mod}}}{2}\cdot\{\sin[(\Omega_{\mathrm{RF}}-\omega_{\mathrm{mod}})\,t] + \sin[(\Omega_{\mathrm{RF}}+\omega_{\mathrm{mod}})\,t]\}. \end{aligned} \tag{3.3}$$

The modulation of the RF-amplitude results in sidebands in the frequency spectrum next to Ω_{RF}. Voltages at the rods of the Paul trap are resonantly enhanced via a helical resonator [8, 9, 35]. The enhancement of the helical resonator is described by a lorentzian profile:

$$U_{\mathrm{RF,\,rods}}(\omega) \propto U_{\mathrm{RF}}\,\frac{\sigma^2}{(\sigma/2)^2 + [\omega/(2\,\pi) - \Omega_{\mathrm{RF}}/(2\,\pi)]^2}, \tag{3.4}$$

with $U_{\mathrm{RF,rods}}(\omega)$ represents the voltage applied to the rods inside the vacuum chamber and $\sigma \approx 2\pi\,40\,\mathrm{kHz}$ as full width at half maximum.
The helical resonator acts as a frequency filter and reflects frequencies outside its amplification profile. A directional coupler in front of the resonator enables us to measure the rejected power for each frequency. We measure the secular frequencies detecting the blurring due to resonant excitation, as described before, in dependence on the reflected part of $U_{\mathrm{RF},0}$ at the directional coupler. Considering the frequency selectivity of the helical resonator, we derive the relative amplitudes of carrier U_{RF} and sideband U_{mod} at the directional coupler, condicering the amplitudes in the beating signal, see fig. 3.2. Based on this, we estimate the relative amplitude at the trap electrodes. The modulation depth η' is defined by:

$$\eta = \frac{U_{\mathrm{mod,\,rods}}}{U_{\mathrm{RF,\,rods}}}, \tag{3.5}$$

where $U_{\mathrm{mod,\,rods}}$ is the modulation amplitude at the electrodes. As the sidebands are about 300 kHz apart from resonance of the helical resonantor, these frequencies are supressed.
In the frequency spectrum relevant for the experiments, the modulation depth varies in the order of 4% due to the frequency selectivity of the helical resonator, see eq. 3.4. The amplitude modulation results in a time dependent radial confinement and, with this, a force sensitive to the distance of the ions from the center (x-axis) inside the crystal.

3.2.3 Isotope selective cleaning

In addition to the secular frequencies representing the trapping potential, the mass of the individual particles is relevant in the eigenmode derivation. We want to compare sets of data taken during several days at the experiment, so we have to do our measurements under comparable conditions. For this, we have to ensure to trap only the isotope $^{24}Mg^{+}$ inside the potential well.
In the beginning of each measurement, we load ions into the trapping volume. As there are all three isotopes around, we trap together with $^{24}Mg^{+}$ other isotopes or even molecular ions. They are of different mass and their secular frequency decreases with the an increase of the mass $\omega_{\mathrm{sec},\,i} \propto 1/\sqrt{m}$, see eq. 2.7. We lower the excitation frequency and resonantly enhance mass selective their motion in the same way as we determine the secular frequencies of the potential. In addition, we lower the confinement of the RF potential, so we can drive ions of different mass than $^{24}Mg^{+}$ out of the trapping potential, as they are not laser cooled. Further details on this methode are described in [8, 35].

3.3 Acquisition of data and structure identification

3.3.1 Experimental sequence for data acquisition

The mean lifetime of the crystals is in the order of several seconds, which is limited by residual background gas collisions. We set up an experimental sequence consisting of four steps to obtain statistical independent measurements. They are scetched in figure 3.3 and described in detail in the following:

1. To initialize structures, we melt crystals with a laser triggered first order phase transitions to a cloud of ions with $\mathrm{BD_{bl}}$. Then we tune the laser frequency red (BD) and increase the power to crystallize the ion cloud. The laser power is optimized to create kinks inside the crystalline structure. Timescales as well as the laser power dependency are aspects studied in detail in [68]. This preparation of the ion crystals enables us to perform quantitative statistically independant measurements.

2. The cooling laser power is decreased to reduce the probability of photo assisted chemical reactions with background gas. The fluorescence light of the initial recrystalized configuration is recorded for an exposure time of 150 ms with an uv-sensitive CCD camera .

3. The radial trapping potential of the ion crystal is modulated with relative amplitude η and a frequency $\omega_{\mathrm{mod}}/(2\,\pi)$ for a time t_{mod}. During the modulation, the

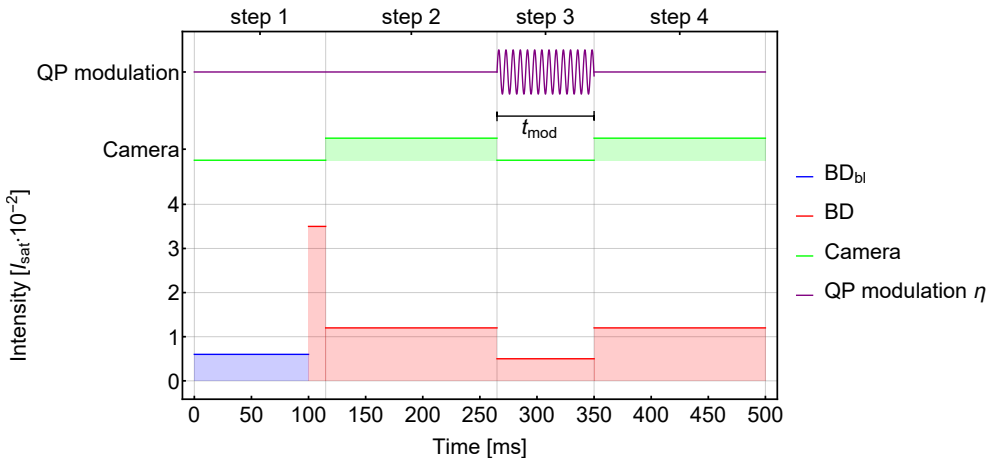

Figure 3.3: Experimental sequence: To investigate individual crystals, we melt our ion crystal with the blue detuned ($\delta \approx +\Gamma/10$) laser ($BD_{bl}$, blue line) to a hot cloud. In the next step we recrystallize the cloud via our red detuned Doppler cooling laser (BD, red line). During the phase transition, we apply a high BD laser power as this leads to a increase of the propability to create a kink. The ion crystal's structure is detected with a first picture of 150 ms exposure time by our CCD camera (green line). Then we lower the cooling power, to reduce photochemical reactions. However it is still strong enough to prevent ions from leaving the crystal. In addition, we modulate $U_{RF,0}$ by η with a selected frequency $\omega_{mod}/(2\pi)$ to excite vibrational eigenmodes (purple sinosoidal). After a certain time of modulation t_{mod}, we record a second picture of the crystalline structure with our CCD camera, to determine whether the initial structure survived. The laser powers are varied between 0.003 and 0.035 I_{sat}.
For each experimental datapoint, we run this sequence at least 100 times to determine the structure survival probability (SSP).

laser power of the cooling laser is reduced by a factor of three to reduce additional damping.

4. In the next step the laser power is rised again to increase the fluorescence signal of the ions. The structure is recorded again by the CCD camera.

The sequence is repeated for each experimental set of data at least a hundred times. Subsequently, we analyze the frames based on an image processing algorithm, see below. The crystals are labeled in three groups: zigzag configuration, with kink and not obviously identifiable (less than 1%). We compare the CCD pictures recorded in step 2 and step 4 of the sequence. If a kink is present in both images, the kink survived the modulation of the trapping potential. As experimental measurand, we calculate the ratio of runs, wherein a crystal with kink survives the modulation duration, to all crystals initially created with kink. We discard crystals containing two kinks and frames with ongoing dynamics during the exposure time. The ratio is called structure survival

probability (SSP) and depends on the modulation frequencies $\omega_{\text{mod}}/(2\pi)$, depth η and duration t_{mod}

$$\text{SSP}\left(\frac{\omega_{\text{mod}}}{2\pi}, \eta, t_{\text{mod}}\right) = \frac{\text{total kinks at step 4}}{\text{total kinks at step 2}}. \tag{3.6}$$

This ratio is a quantity to describe the excitation probability of the kink, which leads to a loss of the kink out of the Peierls-Nabarro potential. Based on this evaluation we can not distinguish between kinks that survived t_{mod} and melted crystals, that recrystallize with a two mismatching domains. This will be discussed in the contaxt of the experimental results.
To calculate SSP, we have to label each camera frame on the detected fluorescence light, showing the structure of the ion crystal. The SSP will be studied in dependency on all three parameters in the results part of this thesis.

3.3.2 Crystal identification

The structure survival propability, as introduced before, is based on the identification of the structure of the crystal in each individual recorded camera frame.
Analyzing the acquired data results to six different crystal conformations: Kink8, $\overline{\text{Kink8}}$, Kink10, $\overline{\text{Kink10}}$, Zigzag and $\overline{\text{Zigzag}}$, as shown in fig. 3.4. In the following, the identification routine is described for the experimentally obtained data, how the individual configuration and its mirror image are identified in our case.

This is done in three steps by a script based on the computer algebra program Mathematica, developed by Wolfram: First we distinguish between structures with and without a kink. We are interested in kinks that are stable at the center of the crystal for several seconds.

Structure identification We select the central part of the crystal as region of interest and evaluate the position of each ion, see fig. 3.5. To label each structure, we compare the results of two methodes based on the coordinates of the ions:

- We calculate the axial distance between neighboring ions in the upper and in the lower string seperately. The variance of the axial distances is used to distiguish between three cases “Zigzag”, kinked crystal (“Kink”) and “Trash”.
  - Zigzags have a periodic structure, so the variance in axial direction is very small ($< 1.5\,\text{pixel}^2$).
  - Crystals with kink have a defined structure, but the axial distances are not as similar as in the case of the zigzag, so the variance is larger. Based on several benchmark measurements, we use the variance of axial distances of the individual ions inside the crystal as criteria. For a kinked crystal it has to be $> 1.5\,\text{pixel}^2$ and $< 5\,\text{pixel}^2$.

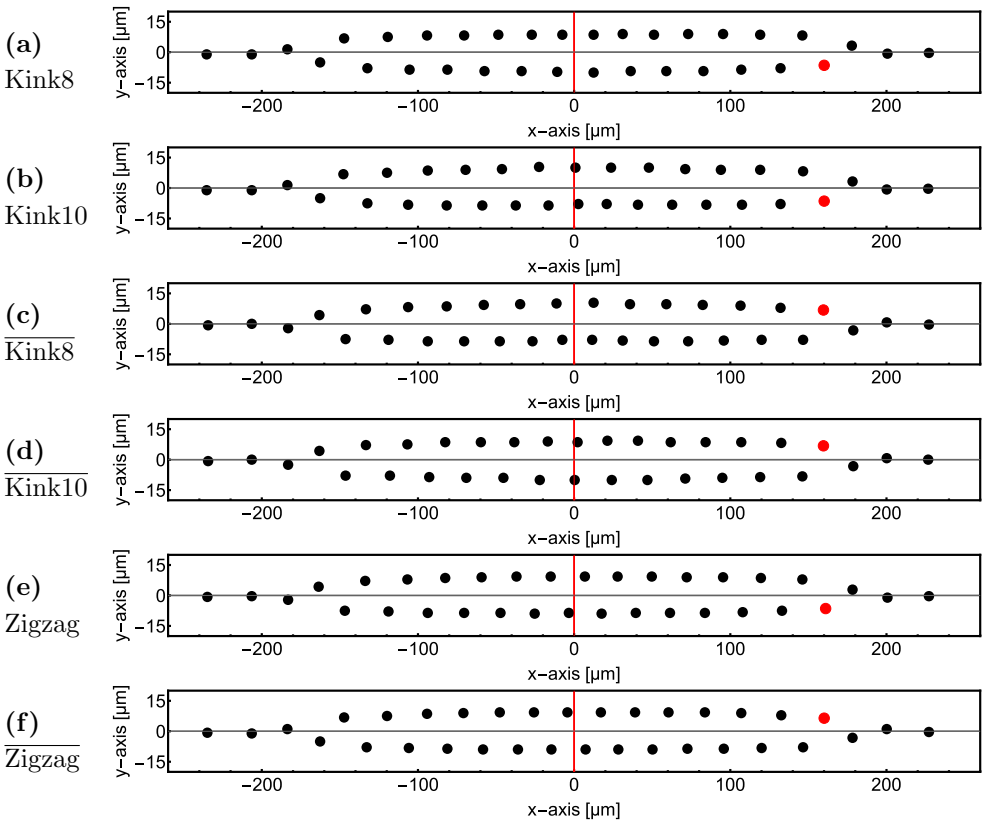

Figure 3.4: Experimentally derived coordinates of 34 ions obtained by the image analysis routine and rescaled by the magnification of the objective in front of the camera. The presented data shows the results of the analysed camera frames. The origin of the coordinate system is located at the center of mass (CoM) of the crystal, calculated from the experimental data. Structures are labeled based on the ions' position relative to the CoM x-coordinate as well as the forth ion from the right, both highlighted in red.
(a) The configuration called "Kink8" is depicted and in **(b)** "Kink10", whereas in **(c)** and **(d)** their anti-particles ("$\overline{\text{Kink8}}$" and "$\overline{\text{Kink10}}$") are depicted.
In **(e)** a "Zigzag" is shown and in **(f)** a "$\overline{\text{Zigzag}}$" is scetched. The CoM in the crystals is slightly shifted to the left, as the red line is not at the center between the ions in the middle. This offers a measure to determine the related deviations of the trapping potential of our Paul trap from the harmonic approximation.

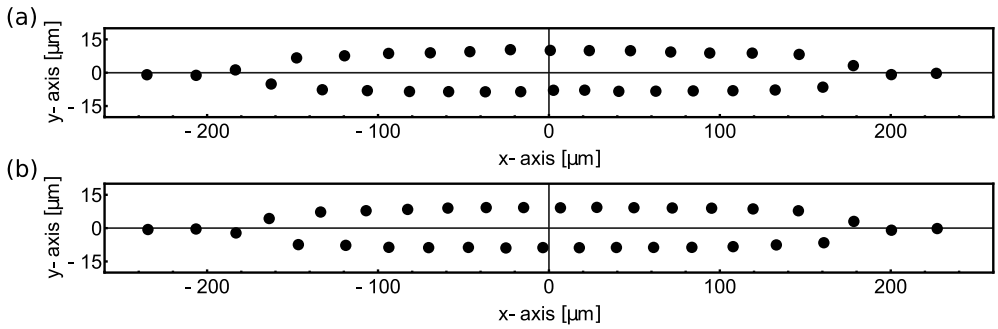

Figure 3.5: Experimentally derived coordinates of 34 ions obtained by the frame analysis routine.
(a) Crystalline structures with a disturbance in the periodicity at the center are labeled "Kink". Note: Two ions are not located at the same x-coordinate as the CoM, as indicated by the numerical result shown in fig. 2.5.
(b) The ions form a "Zigzag" structure, as each ion is on the opposite side of the y-coordinate of the CoM as the ion before.

  - A small amount of crystals shows a variance of $> 5\,\text{pixel}^2$. In most of the cases this is related to an ion, which was not identified as bright spot by the coordinate routine, often related to an insufficient signal to noise ratio. Some of the pictures show no identifiable crystalline structure, as the ion position changes during the exposure time of the camera. These pictures with a disordered structure are labeled as "Trash".

- The second approach is based on the alternating position of each ion with respect to the radial CoM coordinate. The radial distance of each ion from the axial crystal axis is calculated. An ion above the axis has a positive sign, whereas an ion below a negative one. The ions are sorted based on their x-coordinate. Now the signs of the radial coordinate of following ions are multiplied by each other. The result is compared to the following three cases:
  - All products are "-1". This means, that all pairs of ions are on opposite sides of the crystal axis. So the crystal is labeled as "Zigzag".
  - All results are "-1", except one that is "$+1$". There is one pair of ions located at the same side of the y-coordinate of the center of mass of the ion crystal. This crystalline structure is labeled as "Kink".
  - If the number of "$+1$" in the list is larger than one, something in the indentification routine went wrong. This structure is labeled as "Trash".

If both criteria yield the same result, the label is stored and the routine proceeds with the next frame until it reaches the end of the image stack. In the case that the labeling does not match or both methodes label the frame as "Trash", the routine shows the frame to the user, to allow to analyze the origin of the fail.

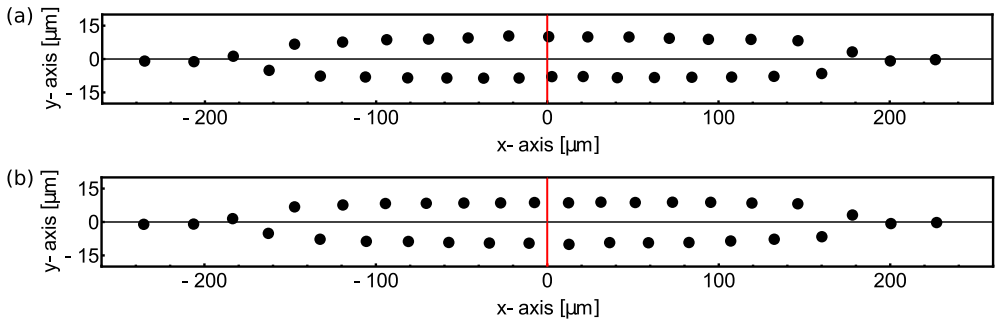

Figure 3.6: Experimentally derived coordinates of 34 ions, containing two type of kinks, obtained by the frame analysis routine and rescaled by the magnification of the objective in front of the camera. As both structures clearly differ at the x-coordinate of the CoM, the latter is highlighted by a red line. The eigenmode spectrum is with in the experimental resolution identical.
(a) Two ions are on opposite sides of the crystal axis and with similar x-coordinates as the CoM. We label this structure a Kink10.
(b) There is a gap at the center of the crystal next to the CoM. We label this structure a Kink8.

Kink configuration identification In a second step, we take all "Kink" labeled structures from the set of data and check whether there are ions around the x-coordinate of the center of mass. Configurations with ions at the center are labeled as "Kink10", as there are about 10 ions displaced from the original periodic "Zigzag", see fig. 3.4 for comparism.
A second configuration appears at comparable rate in the experimental data. There is a gap in the ion crystal at the CoM and the Kink extends to about eight ions, see fig. 3.6 b. So it is labeled as Kink8.

Crystal conformation identification Each experimentally observed structure is labeled by its configuration. The last degree of freedom is the symmetry inside the trapping potential. We have in z-direction a confinement ≈ 1.3 stronger than in y-direction. So the radial degeneracy is canceled and the ions are pushed into two dimensional structures. Assuming symmetric potentials, planar structures like the ion crystals have two degenerate conformations: an image and its mirror image. Independent on the configuration of the crystal, we label all identified structures based on the forth ion from the right side, shown as red disc in fig. 3.7. Around the ion's position, we define a region of interest (ROI) in the order of twice the width of the ion in axial direction and take the complete height of the recorded frame in y-direction into account. Now we sum up each row of the ROI. In the next step, we compare the fluorescence below the y-coordinate of the CoM with the signal above. The crystals with more fluorescence below the y-coordinate of the CoM are labeled as "Down" conformation,

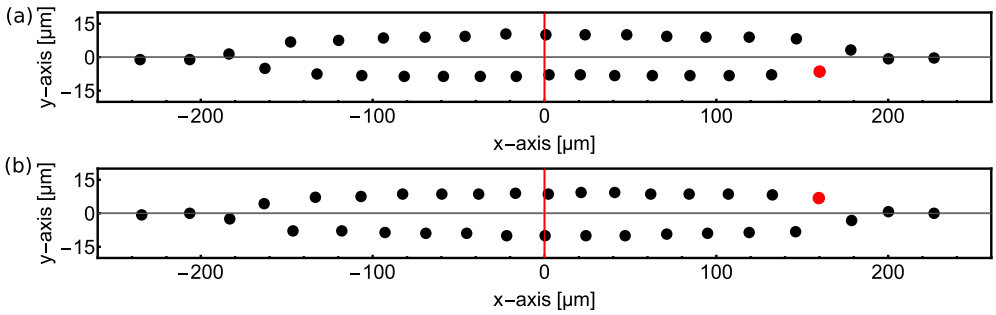

Figure 3.7: Coordinates of 34 ions obtained by the frame analysis routine and rescaled by the magnification of the objective in front of the camera.
The crystallization is a random process and the two dimensional structure might also be rotated by 180° around the x-axis of the crystal. Both structures are energetically degenerate. A rotation without melting is not possible in the trapping potential. So both structures are individual distinguishable conformations and have to be labeled independently. This is done by the position of the 4^{th} ion from the right side, highlighted as a red disc.
(a) Crystalline structure with a Kink10 at the center and the outer ion below the crystal axis, is labeled as Kink10.
(b) Ion crystal with a Kink10 at the center and the outer ion above the x-axis is labeled as $\overline{\text{Kink10}}$.

the others as "Up". Comparing both conformations of kinks inside crystals, it becomes obvious that one can define "Down" as the particle and "Up" as the anti-particle, as introduced in fig. 2.4.

3.4 Molecular dynamics simulation

We can tune the experimental parameters and study their influence on the structure survival probability, see chapter 4. However, the signal to noise ratio of each camera frame limits us to study processes on timescales below the chosen exposure time of our CCD camera of 150 ms. During detection, we increase the laser power to detect enough photons on each pixel. We alternate the laser power during the rest of the sequence to reduce the amount of photo chemical reactions of our Magnesium ions. In the context of this limitations, we study relevant timescales and dynamical processes inside the crystal, assisted by numerical simulation. Haggai Landa developed during his master thesis [47] a molecular dynamics (MD) simulation for Coulomb crystals in a Paul trap, considering micromotion [48].
The simulation is based on classical mechanics and neglects quantum mechanical effects. The global potential, starting positions of the ions and initial velocities are relevant for the simulation. First the energy is minimized as the positions of the ions inside the

potential are optimized. Ions move inside the potential due to their initial velocity and momentum transfer due to interaction with other particles. The simulation is concatenated by timesteps small compared to $1/\omega_{102}$. Within a timestep each particle moves independently along its trajectory. At the end of each timestep, velocities and interaction with neighboring particles are recalculated and set as initial conditions for the next timestep.
A first comparison between simulation and experimental results is published in [2]. Further studies on the kink dynamics in simulation are shown in [1].

Amplitude modulation In the experiments, we modulate the amplitude of the trapping potential, see chapter 3.2. This is implemented in the differential equation of motion in pseudo-potential approximation in radial direction, see eq. 2.6:

$$\frac{\partial^2}{\partial t^2}y + \left[\omega_{\mathrm{y}}^2 + \left(\frac{\mathrm{q}}{2}\frac{\Omega_{\mathrm{RF}}/\omega_{\mathrm{x}}}{2}\right)^2 \left(\eta' \cdot \sin\left(\omega_{\mathrm{mod}}t\right) + \eta'^2 \sin^2\left(\omega_{\mathrm{mod}}t\right)\right)\right] y = 0 \qquad (3.7)$$

with q= $\frac{2\,\mathrm{e}\,U_{\mathrm{RF},0}}{m\,\alpha_{\mathrm{RF}}^2\,\Omega_{\mathrm{RF}}}$, where α_{RF} represents the scaling to the trap geometry [8, 9]. η' is the modulation depth as defined above in eq. 3.5 and $\eta' \ll 1$, so the term in η'^2 can be neglected.

Laser cooling During the experimental sequence, we reduce the laser power in step 3, see fig. 3.3, but it is still present. This is considered in the molecular dynamics simulation with a Langevin-type equation [69, 70]. The cooling rate depends on the laser power and is a free parameter sD in the simulation, similar to I/I_{sat} as introduced in eq. 2.12. In addition the simulation takes into account, that we directly cool the ions primarily along the axial direction only. To compare simulation and experiment, we have to calibrate sD to the laser intensity used during the experiments.

We calculate trajectories of the ions of the Coulomb crystal with the simulation. The motion inside the crystal can be decomposed to the normal coordinates as shown in sec. 2.3. Two vibrational eigenmodes of a kinked crystal as a function of simulation time are shown in fig. 3.8 (a),(b). The trapping parameters correspond to the experimental conditions. We derive relevant timescales like the excitation of each vibrational eigenmode from the simulation. Based on our definition of the kink coordinate we can trace its position during the simulation, as shown in fig. 3.8 (c).
In addition, we estimate the viscosity $\xi_{\mathcal{K}}(T)$ from results of the simulation, as we currently do not have direct experimental access to measure the auto correlation function of the kink velocity and the shape of the Peierls-Nabarro potential.

In the following, we present numerically derived data colored in orange or gray, to allow the reader to distinguish between experimentally and numerically derived data.

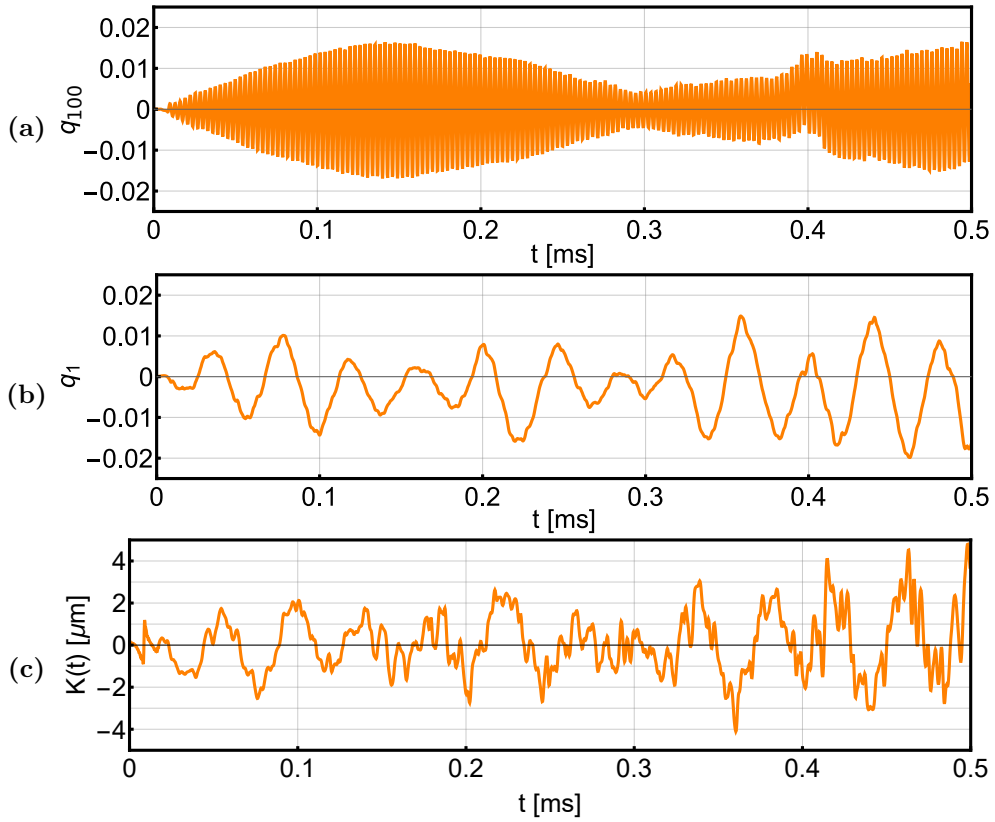

Figure 3.8: Numerically simulated amplitudes of vibrational eigenmodes on timescales, the RF modulation excites the system.
(a) The eigenmode amplitude of q_{100} increases in the prescence of the RF modulation until 0.15 ms, then it drops to about half the amplitude. This is an indication, that the amplitude reaches a certain level, when nonlinear mode coupling becomes relevant in the dynamics inside the ion crystal.
(b) In addition there is no change for instance in the amplitude of mode q_1 until about 0.3 ms. At this point the amplitude of mode q_{100} reaches its minimum and the amplitude of q_1 increases.
(c) The location of the kink is depicted as a function of time. The kink coordinate is defined by eq. 2.18.

Chapter 4

Resonant excitation of structural defects

The experimental setup and the data analysis are described in the previous chapter. Here we focus on the results and their discussion in detail. In this chapter, the results are presented for the eigenmode spectroscopy and the related mean lifetime measurements of the kink inside the ion crystal. The last part of this chapter discusses the derivation of the depth of the Peierls-Nabarro potential based on Kramers' model.

4.1 Spectroscopy of vibrational eigenmodes

Coulomb crystals with structural defects feature a characteristic eigenmode spectrum compared to crystals without a defect, see fig. 2.8. For instance, there is an axial sliding mode, whose frequency is below the axial centre of mass frequency. An excitation to the anharmonic regime leads to an escape of the kink in axial direction. The outer frequency rage of the normalmode spectrum is shifted in the prescence of a structural defect up to 30 kHz away from the frequencies from a zigzag.
We excite eigenmodes of the ion crystal with motional components mostly in radial direction via amplitude modulation of the radial trapping potential, as discussed before. Eigenmodes located on the ions contributing to the kink are of further interest. First we set $t_{\mathrm{mod}} = 85\,\mathrm{ms}$ and $\eta = 1.45 \times 10^{-3}$. We run the experimental sequence and modulate the amplitude of the RF-field with frequencies $\omega_{\mathrm{mod}}/(2\pi)$ of choice in the range from 315 to 336 kHz in random order. The result is shown in fig. 4.1 as blue squares.
Reference level of 0.9 is in agreement with the mean lifetime of such crystalline structures, limited by residual gas collisions. The errorbars are calculated based on binomial statistics, indicating the 1σ interval. The structure survival probability (SSP) is reduced to about 15% at a modulation frequency $\omega_{\mathrm{mod}} = 2\pi(325.3 \pm 0.3)\,\mathrm{kHz}$. The full width at

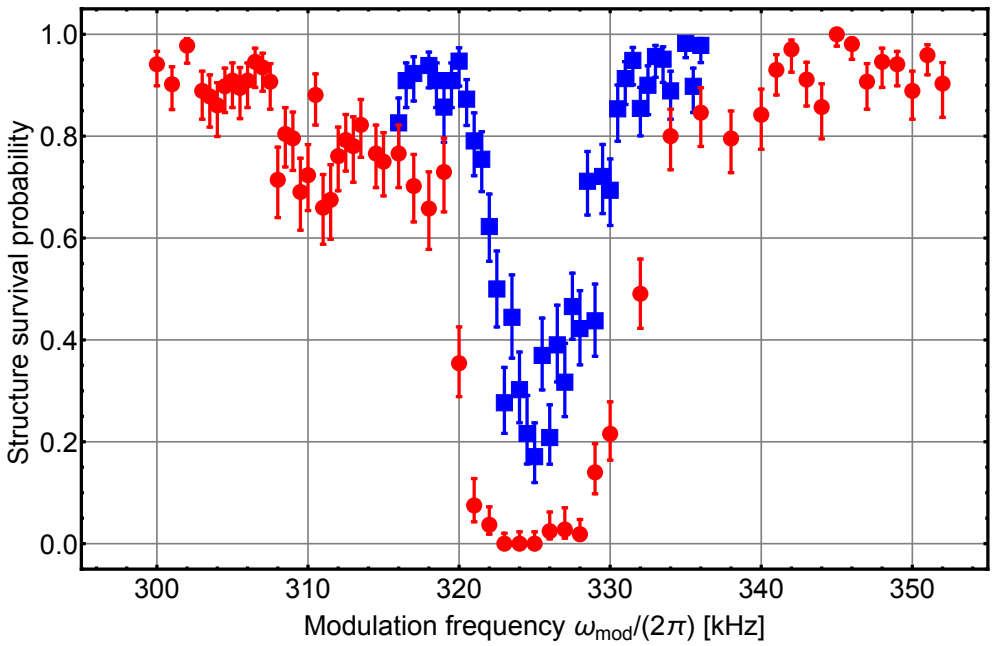

Figure 4.1: The experimentally determined structure survival probability (SSP) as a function of modulation frequency $\omega_{\mathrm{mod}}/(2\pi)$ and modulation depth η (blue squares: $\eta = 1.45 \times 10^{-3}$, red circles: $\eta = 1.74 \times 10^{-3}$). During data evaluation, there is only distinguished between kink containing crystals and zigzags. Around a frequency $\omega_{\mathrm{mod}}/(2\,\pi)$ of $(325.3 \pm 0.2)\,\mathrm{kHz}$ the soliton is excited and leaves the crystal in about 85 % of the analyzed experimental sequences.
This ratio depends on the modulation depth. In the case of $\eta = 1.74 \times 10^{-3}$ the survival ratio is for several $\omega_{\mathrm{mod}}/(2\pi)$ around zero. For a modulation frequency of $(311 \pm 1)\,\mathrm{kHz}$, there is an additional local minimum in the survival probability related to q_{97}.

half maximum (FWHM) of the resonance is $2\pi(4.8 \pm 0.5)\,\mathrm{kHz}$. Data taken for a modulation depth $\eta = 1.74 \times 10^{-3}$ is labeled in red discs and broadened around resonance due to a stronger modulation compared to $\eta = 1.45 \times 10^{-3}$. The modulation frequency is close to an eigenfrequency of the crystal, and its eigenvector has an sufficient overlap with the radial excitation modulation. The eigenfrequency q_{100} (see fig. 2.9 (a)) calculated for such an ion crystal in pseudo-potential approximation deviates to the minimum of the experimental data about 1% in frequency. The shift is comparable to the results obtained by molecular dynamics (MD) simulation in pseudo-potential approximation, as shown in fig. 2.8. Simulations with time dependent radial trapping potential reveal a shift of q_{100} less than 0.5%, due to micromotion.
The datapoints for larger modulation depth ($\eta = 1.74 \times 10^{-3}$) show at $\omega_{\mathrm{mod}} = 2\pi(311 \pm 1)\,\mathrm{kHz}$ an additional local minimum with a depth of 25%. This is next to the eigenfrequency of mode q_{97}, see fig. 2.9 (b). SSP drops at the eigenfrequencies of q_{97} and q_{100}, in both cases the eigenvector projected to the ions has mainly radial components, as

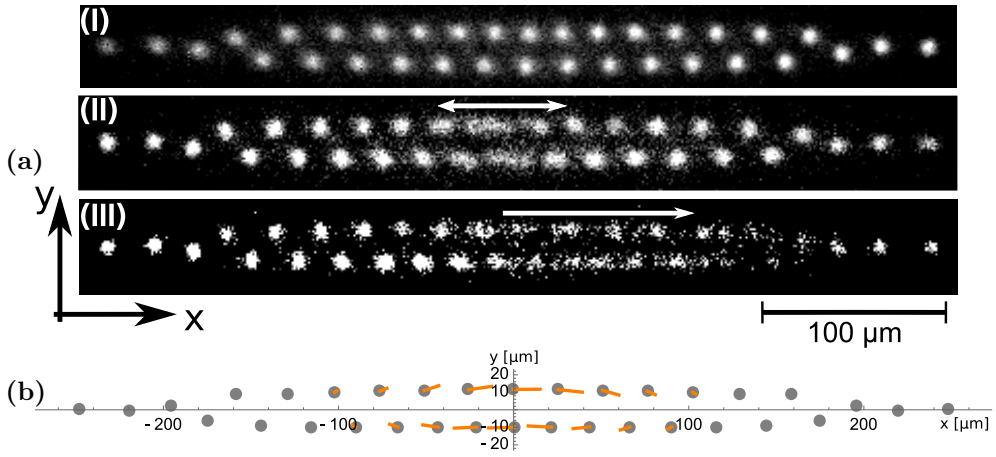

Figure 4.2: 34 ion crystal confined in a linear Paul trap with $\omega_{(\mathrm{x,\ y,\ z})}/(2\pi) = (38.1 \pm 0.5, 233.3 \pm 0.2, 293.74 \pm 0.3)\,\mathrm{kHz}$.
(a) Experimentally obtained flourescence images:
(I) Ion crystal with periodic zigzag structure interrupted at the center by a structural defect (extended kink), stable for several seconds and linear chains to the outer sides. The two central ions are almost on top of each other, the other ions are arranged in zigzag configuration.
(II) At the center of the crystal the ions oscillate due to external high frequency excitation at 327 kHz and nonlinear coupling of energy to excite the low energy kink mode q_{102}, indicated by the white $\leftrightarrow$ at the top. The outer parts do not contribute in the motion.
(III) Similar to (II), but we increase η further, so the kink is heated out of the crystal to the right, as depicted by the white arrow. As the motion is fast compared to the exposure time of the camera, the right half of the crystal is recorded as a superposition of a kink containing and a zigzag crystal.
(b) Simulated ion positions (black dots) in pseudo-potential approximation (PPA) and certain vibrational eigenmodes of the ion crystal containing a kink. Eigenmode q_1: mainly axial contributions to the movement profile, which could be described as an axial sliding mode.

shown in fig. 2.9 (a), (b).

We drive a high frequency eigenmode of the ion crystal and this leads to a loss of the kink out of the PN potential. In the following, I discuss two possible explanations:

First the resonant enhancement of q_{100} (q_{97}) leads to a melting of the crystalline structure to a non-neutral plasma. This might lead to a loss of the kink, but this explanation we neglect due to a SSP of zero on resonance of q_{100} for $\eta = 1.74 \times 10^{-3}$. If the crystal is heated up to an ion cloud, the recrystalization leads to a nonzero probability to obtain a crystalline structure with kink. So camera frames recorded during step 4 in the experimental sequence would show at least few crystals with a kink. In our definition the kink would have survived the excitation.

The second approach to identify the mechanism, which leads to the loss of the kink, is to record camera frames during t_{mod}. We modified the experimental sequence in such a way that the exposure time of the camera is parallel in time to the quadrupol modulation. Recorded frames are identified in the basis set as shown in fig. 3.4. The fluorescence images from step 4 of crystals with the same structure at step 2 are averaged to increase signal to noise ratio. Results of this procedure are shown in fig. 4.2 (a) (II). They reveal a central region in the crystals of undefined structural order. This is related to an oscillatory motion of the ions contributing the kink, which corresponds to the motional directions related to eigenvector q_1, see fig. 4.2 (b). Further increasing η, and analyzing the frames the same way as before, we obtain images (from "step 4") as shown in fig. 4.2 (a) (III). One half of these crystals shows in axial direction a periodic structure, whereas the other side is smeared out. The ions' motion is faster than the exposure time of the camera (150 ms). Therefore, we conclude that the kink leaves the crystal, if its axial motion q_1 is excited.
This is in agreement with the MD simulation, which shows in first step an increase of amplitude in mode q_{100}, see fig. 3.8 (a). At about 0.15 ms the motion of q_{100} decreases and the amplitude of q_1 starts to increase at about 0.3 ms, see fig. 3.8 (b). So motional energy is transfered to other modes and on a second timescale to the low energy mode.

The Peierls-Nabarro potential confines the kink inside the ion crystal, there should be an oscillatory motion of the kink in its harmonic potential. The experimental data does not show such a behaviour, but this might be related to damping of the cooling laser necessary to detect fluorescence light. Even in the simulation the kink moves only related to the temperature of the crystal on its position of minimal energy at the central lattice side of the crystal.
Results from the MD simulation show that mode coupling is relevant on short timescales (up to 0.5 ms), but the loss of the kink happens on a timescale, where the whole mode spectrum is excited.
So the mechanism is rather related to a heating of the phonon bath than a direct coupling or even coherent drive of selected eigenmodes in the crystal.

Latter we tested by a random phase shift of U_{mod} at $t_{\mathrm{mod}}/2$, but there is no evidence that this would increase the SSP. This might be limited by the finite temperature of the system above the Doppler limit. We proceed on this topic as soon as we have a sub-doppler laser cooling setup [71] available at the ion trap apparatus.

We did similar experiments on eigenmode spectroscopy with an intensity modulated radial laser, focused to a single ion. The modulation frequency corresponds to ω_1, but the secular frequencies were different, so there are ions having motional components along the $\vec{k}_{\mathrm{L}}$ of the focused laser beam, adressing a single ion. Details are discussed in [35].

With our experimental approach, we can resolve individual vibrational eigenmodes of Coulomb crystals containing a kink. The time scale of kink loss mechanism is studied in the following.

4.2 Mean kink lifetime

The experimental data presented in figure 4.1 show the structure survival probability (SSP) as a function of the modulation frequency $\omega_{\mathrm{mod}}/(2\pi)$. For $\eta = 1.74\times10^{-3}$ (shown in red) the resonance is broadened. The kinks do not survive for several modulation frequencies around $2\pi(326 \pm 3)\,\mathrm{kHz}$. The measurement with reduced $\eta = 1.45 \times 10^{-3}$ shows a local minimum at $2\pi \times 326\,\mathrm{kHz}$. The excitation duration of 85 ms is constant in both measurements. To get a deeper insight in the loss mechanism, we vary the excitation duration t_{mod} for different η. In contrast to the experimental data shown above (see fig. 4.1), the trapping potential of the ion crystal is modulated with the fixed frequency corresponding to the minimal survival probability. The results are shown in fig. 4.3. Each datapoint represents at least a hundred runs of the experimental sequence (see fig. 3.3) with a certain modulation amplitude η and duration t_{mod}. The SSP decreases with an increase of η, as shown in fig. 4.1, and is in addition dependent on the modulation time t_{mod}. The data is corrected by the loss rate of kinks due to their limited lifetime, because this is limited to about 3.2 s. The set of datapoints, shown in fig. 4.3, are taken during several days at the lab, which causes certain fluctuations of the experimental parameters. They are represented by the error bars given at the experimental parameters like trapping frequencies.

SSP can be described by an exponential decay $e^{-t/\tau}$ for each η. Further discussion of the experimental data is split in two separate parts: the data for (1) $\eta > 1.4 \times 10^{-3}$ and (2) $\eta < 1.4 \times 10^{-3}$.
(1) The SSP drops to zero within $\approx 200\,\mathrm{ms}$ of modulation. The mean lifetime for $\eta = 1.45\times10^{-3}$ is $(71 \pm 5)\,\mathrm{ms}$ (blue) and in the case of $\eta = 1.74\times10^{-3}$ it is $(23 \pm 2)\,\mathrm{ms}$ (red).
(2) The structure survival probability does not drop to zero within 300 ms. We assume

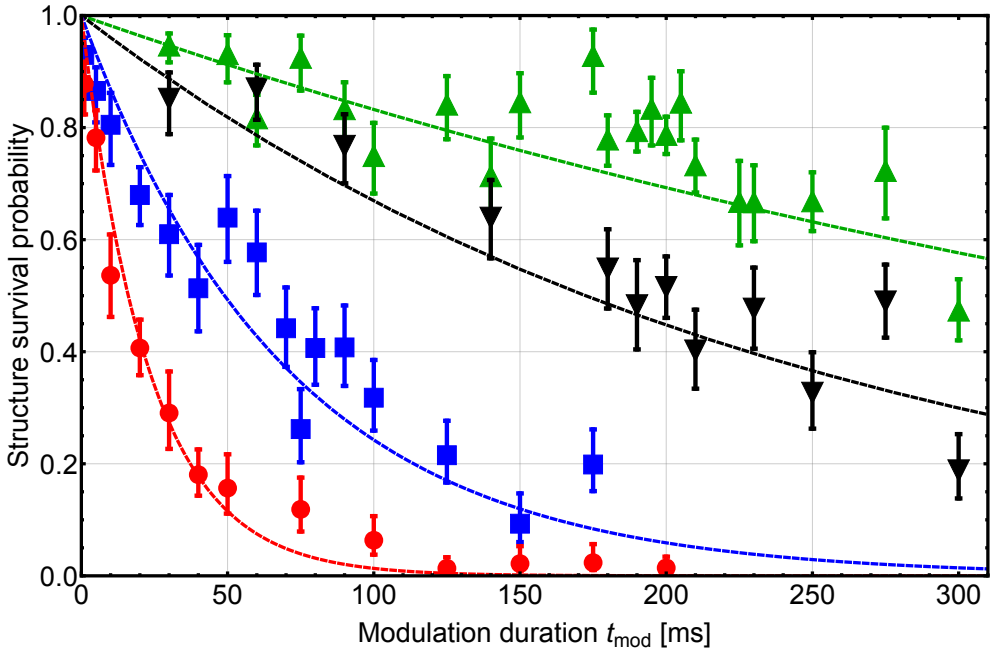

Figure 4.3: Structure survival probability as a function of modulation duration t_{mod}. The data is shown for four modulation depths η. $\eta \times 10^3 \in \{1.15, 1.30, 1.45, 1.74\}$ are labeled in {green, black, blue, red}. Mean lifetimes result to $\{(544 \pm 35)\,\mathrm{ms}, (248 \pm 16)\,\mathrm{ms}, (71 \pm 5)\,\mathrm{ms}, (23 \pm 2)\,\mathrm{ms}\}$. Datapoints represent at least a 100 measurements. Data is rescaled by losses due to the natural lifetime ($\approx 3.2\,\mathrm{s}$) of kinks inside ion crystals. The results of an approximation of an exponential decay are shown as dashed lines in the corresponding color.

that for these η the SSP drops to zero as well, but on timescales longer than studied in these experiments. So we calculate the decay constants and obtain in the case of black with $\eta = 1.3 \times 10^{-3}$, $\tau = (248 \pm 16)\,\mathrm{ms}$ and for $\eta = 1.15 \times 10^{-3}$, $\tau = (544 \pm 35)\,\mathrm{ms}$. However, this is still under investigation and has to be studied further as there are first hints that the SSP does not drop to zero within 1000 ms. These diverging timescale have to be studied further are might be a way to test theoretical prediction on self-stablizing phase-space trajectories [72].

We achieve similar SSP for short but strong excitation as for long and weak. So we can interprete this as a heating mechanism inside the crystal. It does not matter, whether the internal energy is rised on short or on long timescales. The excitation based on the modulation of the trapping potential η is stronger than the stabilization due to laser cooling, the structural defects leave the crystal. A linear increase in the modulation effects the mean lifetime in a nonlinear way.

So we can resolve the individual mean lifetime of structural defects inside the crystals in dependence of η. The modulation depth results to an internal energy via nonlinear mode coupling, the mean kink lifetime depends on the internal energy. As discussed before, kinks move along the crystal axis and vanish, so the structural defects leave the

Peierls-Nabarro (PN) potential. The barrier height of the PN potential can be derived based on the mean lifetime and the internal energy.

4.3 Estimation of the barrier height of the kink trapping potential

As introduced in chapter 2, we approximate the barrier height of the Peierls-Nabarro (PN) potential based on the Kramers' model [29]. This can be interpreted as a measurand of the quasi topological protection. For this, we have to calculate the viscosity of the ion crystal for several temperatures based on the numerical simulation introduced in chapter 3.4.

4.3.1 Viscosity $\xi_{\mathcal{K}}$ of an ion crystal

We compute based on the results of the numerical simulation the velocity autocorrelation function (vACF) of the kink coordinate for several internal temperatures, see fig. 4.4. The simulation is run without laser cooling and quadrupol modulation. To calculate the integral of the vACF, we neglect the fast oscillatory components and focus on the envelope. We slice the simulation duration in 50 short intervals. The maximum of the absolute value of each slice is taken and its corresponding time to describe the envelope of the vACF. This is valid as long as we are only interested in the decay constant of the envelope. The suggested offset is related to the methode, as we take the maximum into account. The results are shown as gray dots in fig. 4.4. We approximate an exponential decay to these datapoints as depicted as gray dashed line. The decay constants of at least 24 runs for each temperature are averaged. Using eq. 2.28, we calculate the viscosity $\xi_{\mathcal{K}}$ for each temperature seperately, assuming that the density of the ion crystal ρ_{IC} stays constant in this temperature regime. The results are plotted in fig. 4.5 as orange datapoints.
The viscosity depends strongly on the temperature of the system. Kramers' model is based on the viscosity of the system, so it has to be described by an analytical expression. First we discuss the approach derived by Raman and Andrade [60, 61] as shown by a light gray line in fig. 4.5:

$$\frac{\xi_{\mathcal{K}}\left(T_{\mathrm{D}}\right)}{\rho_{\mathrm{IC}}} = \xi_0\, e^{b/T_{\mathrm{D}}} = (1.90 \pm 0.05)\ 10^{-10}\,\frac{\mathrm{m}^2}{\mathrm{ms}}\, e^{(2.6\pm0.4)\,10^{-4}\,T_{\mathrm{D}}/T} \tag{4.1}$$

where ξ_0, b are free parameter approximated to numerically obtained datapoints. The approach underestimates the data, especially for low internal temperatures.
This is also the case for the model $\propto T^{-\alpha/2}$, as shown by a dark gray line in fig. 4.5.

$$\frac{\xi_{\mathcal{K}}\left(T_{\mathrm{D}}\right)}{\rho_{\mathrm{IC}}} = (4.1 \pm 0.3)\,10^{-10}\,\frac{\mathrm{m}^2}{\mathrm{ms}}\,T^{\,(-0.35\pm0.05)} \tag{4.2}$$

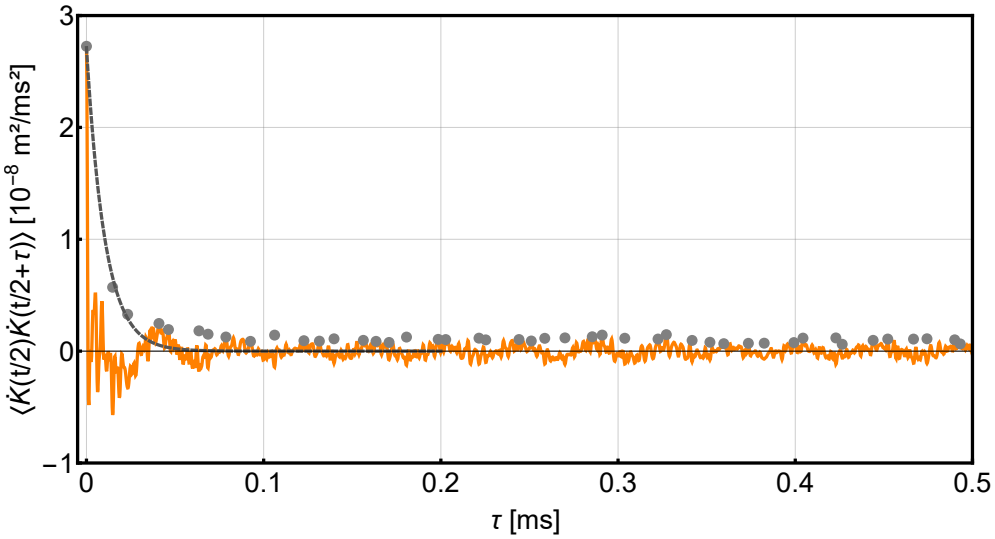

Figure 4.4: Velocity autocorrelation function for $T = 3\,T_\mathrm{D}$. Data shown in orange represents the trace calculated based on the numerical simulation. The data is dominated by two timescales, fast oscillations and the decaying envelope. As we are interested in the decay constant, we neglect the highfrequency oscillatory motion of the kink, slice the timetrace into 50 parts of $10\,\mu s$ each, and take the maximum absolute value, indicated by the gray datapoints. It can be described by an exponential decay, shown as dashed gray line. As we take the maximum value of each slice, on longer timescales the gray points suggest an offset in the data. However, this is due to the noisy environment and is neglegted.

We derive an effective dimension of the system $\alpha = (0.7 \pm 0.1)$. As the kink can only move along the x-axis of the crystal, the system is quasi one dimensional, thus, we expect α to be 0.5.
For low internal temperatures the description with both models deviates strongly from the numerical data, as shown by orange datapoints in fig. 4.5 in comparism to the gray lines representing the models. Both models are developed for systems with a continuous dispersion relation and temperatures, which ensures that all modes are equally populated with phonons.
As long the internal temperature is above $4\,T_\mathrm{D}$, both models describe the dependency of viscosity $\xi_\mathcal{K}$ and temperature well.

So far, we only take the internal temperatures, representing the internal energy of the system, into account. During the experiments, we have access to the modulation depth η and the cooling rate sD, which is related to the intensity of the laser I_sat. However, we can not directly measure the internal energy distribution or even the temperature T of the ion crystal in experiment.
We perform further numerical studies to derive a relation between T, sD and η. The system is initialized at a certain temperature, the internal energy increases in the pres-

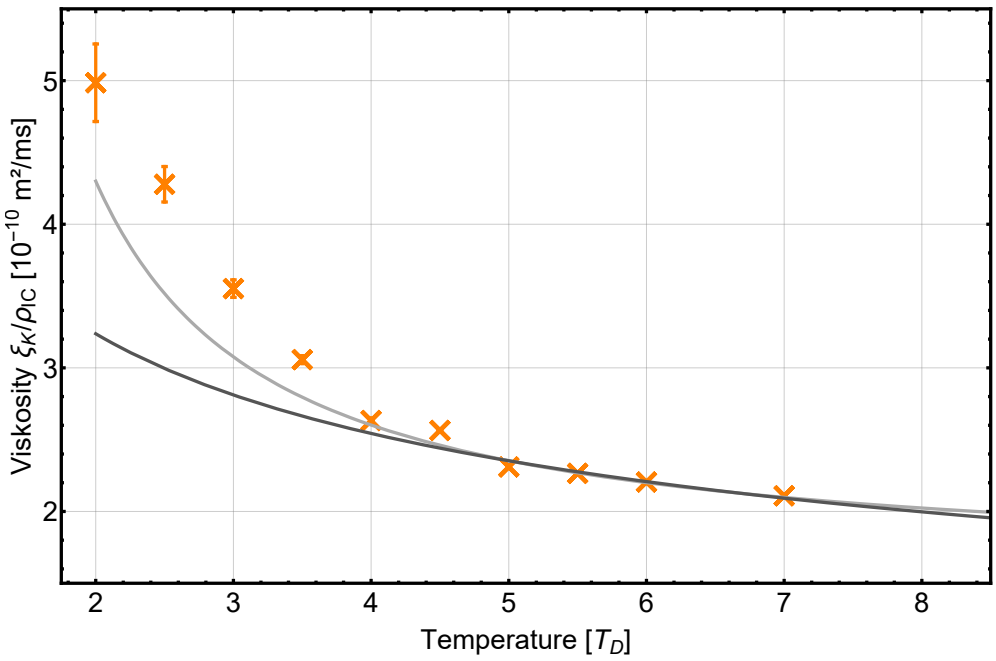

Figure 4.5: Viscosity $\xi_{\mathcal{K}}/\rho_{\mathrm{IC}}$ versus internal temperature of the ion crystal. The MD simulation is run for at least twenty times for each temperature and we calculate the integral of the vACF for each run. Mean and standard deviation are plotted for each temperature. As we need an analytical expression as input for the Kramers' model, we approximate the datapoints by $\xi_0\, e^{b/T}$ (light gray line) and $\propto T^{-\alpha/2}$ (dark gray line), describing the viscosity in dependency of temperature T. Both models underestimate the increase of the viscosity in the low temperature regime.

ence of quadrupol modulation. The mean kinetic energy turns into equilibrium after a certain duration for given modulation η and cooling rate sD. Since the relevant timescales are much longer than the timescale for the heating process, we can assume equipartition of all eigenmodes corresponding to the internal energy distribution. Running simulations in the experimentally accessable parameter range, we derive the datapoints shown in fig. 4.6. Each datapoint represents at least ten runs of simulation. Assuming a linear dependency of modulation depth, cooling rate and mean kinetic energy, we interpolate the data and get a calibration surface, as shown in gray in fig. 4.6. This can be described by the following formular:

$$\begin{aligned}\langle E_{\mathrm{kin}}\,(sD,\,\eta)\rangle &= \frac{\sum_{\mathrm{i}=1}^{\#\mathrm{ions}} E_{\mathrm{kin},i}\,(sD,\,\eta)}{\#\mathrm{ions}} \\ &= (2.9 \pm 0.1) - (389 \pm 24)\; sD + (2140 \pm 68)\,\eta. \end{aligned} \tag{4.3}$$

The energy is given in units of T_{D}. In the experiments the number of ions (#ions) amounts to 34. All experiments are run under same cooling conditions during step 3 (see fig. 3.3).

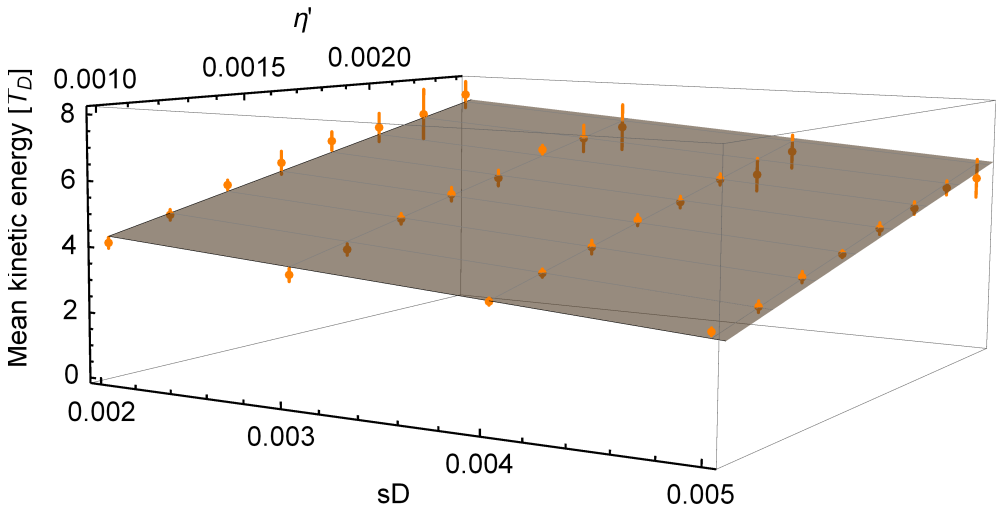

Figure 4.6: Relation between mean kinetic energy in units of T_D, cooling parameter sD and modulation depth η. We run the MD simulation to study the influence of cooling sD and quadrupol modulation on the internal temperature. Numerical studies were carried out several times for each combination of parameter sets and we calculate mean and standard deviation of the mean kinetic energy (orange datapoints). To interpolate the data, we assume a linear dependency on both parameters and approximate the model to the data, as shown by the gray surface.

We can not quantify the difference between the cooling model in the simulation and the laser cooling by photon scattering in the experiment. In the experiment combinations for laser cooling and η result to a mean lifetime of the kinks, as shown in fig. 4.3. The parameter sD is approximated iteratively to $sD = 2.25 \times 10^{-3}$ by tuning the mean lifetime τ in the simulation for an excitation $\eta = 1.15 \times 10^{-3}$ to achieve the experimentally obtained results $\tau = (544 \pm 35)\,\mathrm{ms}$.

Subsequently, we apply the derived relation between mean kinetic energy and the cooling parameter sD to rescale the x-axis in fig. 4.5 in terms of η. Therefore, we obtain an analytic expression corresponding to the numerically derived datapoints for the viscosity:

$$\frac{\xi_\mathcal{K}(\eta)}{\rho_\mathrm{IC}} = (1.90 \pm 0.05)\,10^{-10}\,\frac{\mathrm{m}^2}{\mathrm{ms}}\,e^{-\frac{(-2.7\pm0.4)10^{-4}}{\eta'}}. \tag{4.4}$$

The alternative model results in

$$\frac{\xi_\mathcal{K}(\eta)}{\rho_\mathrm{IC}} = (4.5 \pm 1.2)\,10^{-11}\,\frac{\mathrm{m}^2}{\mathrm{ms}}\,\eta^{(-0.25\pm0.03)}. \tag{4.5}$$

Both models describe the viscosity for experimental relevant η. In the following we use the model, taking the dimensionality of the system into account: $\propto \eta^{-\alpha/2}$.
This equation is used to describe the viscosity in the Kramers' model and we calculate the barrier height of the PN potential in the next step.

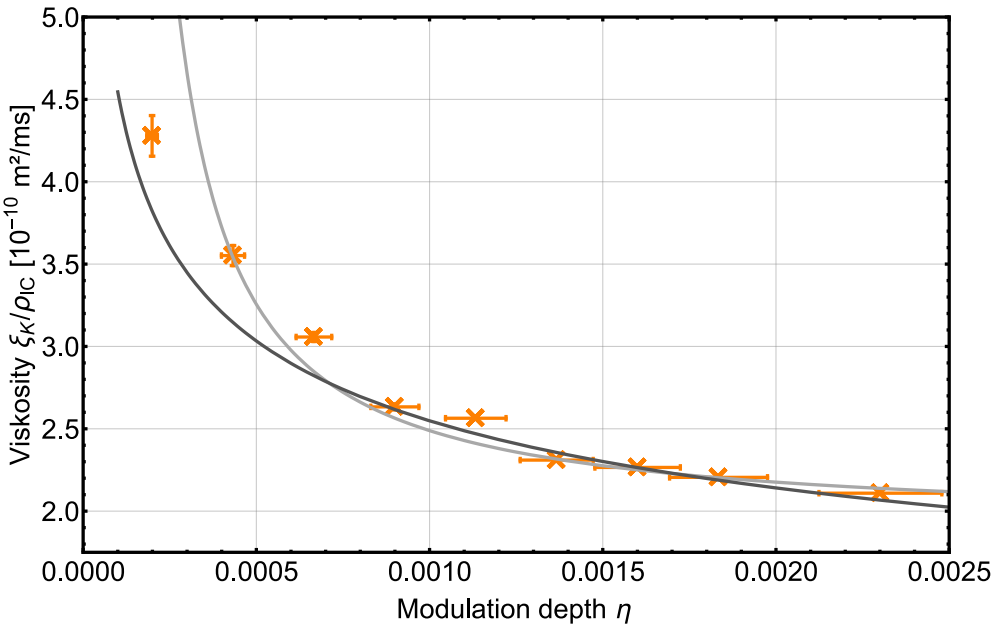

Figure 4.7: Viscosity $\xi_{\mathcal{K}}/\rho_{\mathrm{IC}}$ in dependency on the quadrupol modulation depth. For a fixed cooling rate sD, we can relabel the T-axis of fig. 4.5 with the modulation depth η, as we derived the linear relation in eq. 4.3. Mean and standard deviation are plotted for each η. Again we test both models to describe the relation between η and viscosity $\xi_{\mathcal{K}}$. The light gray curve ($\propto e^{b/T}$) as well as the $\propto T^{-\alpha/2}$ (dark gray curve) describe the relation in the relevant range of η between 0.001 and 0.002.

4.3.2 Barrier height of the Peierls-Nabarro potential

The numerically derived results are combined to calculate the barrier height E_{PN} of the PN potential. Kramers' equation as shown above (see eq. 2.35) is extended by the numerically derived analytic expression for the viscosity of the ion crystal as function of the internal temperature, respectively the modulation depth:

$$\tau\left(\eta\right) = \frac{\pi \frac{\xi_{\mathcal{K}}(\eta)}{\rho_{\mathrm{IC}}}}{\omega_1} \frac{\rho_{\mathrm{IC}}}{\omega_{\mathrm{B}}} e^{\frac{E_{\mathrm{PN}}}{\eta}} \tag{4.6}$$

There are still two free parameters, E_{PN} and ω_{B}. Both parameters are optimized to the numerically derived mean lifetimes and the result is shown in fig. 4.8. Experimental datapoints are colored the same way as in fig. 4.3 and are in agreement with the numerically derived Kramers' model. $\frac{\rho_{\mathrm{IC}}}{\omega_{\mathrm{B}}}$ amounts to $(1.2 \pm 0.07)\, 10^{10}\, \frac{\mathrm{kg}}{\mathrm{m^3\, s}}$. A rough estimate on the density ρ_{IC} amounts to $2.5 \cdot 10^{-12}\, \frac{\mathrm{kg}}{\mathrm{m^3}} = 2.5\, \frac{\mathrm{ng}}{\mathrm{m^3}}$ for $^{24}\mathrm{Mg}^+$ assuming an average distance of $\approx 25\,\mu\mathrm{m}$ in all three dimensions. Thus, we derive $\omega_{\mathrm{B}} = 2\pi(3.3 \pm 0.3) \times 10^{-23}\,\mathrm{Hz}$.

As before all parameters are still a function of η, we rescale the data with eq. 4.3 as shown by the upper x-axis. We derive the barrier height $E_{\mathrm{PN}} = (24.2 \pm 0.7)\, T_{\mathrm{D}}$. As Kramers' model [29] estimates the mean first passage time over a certain potential

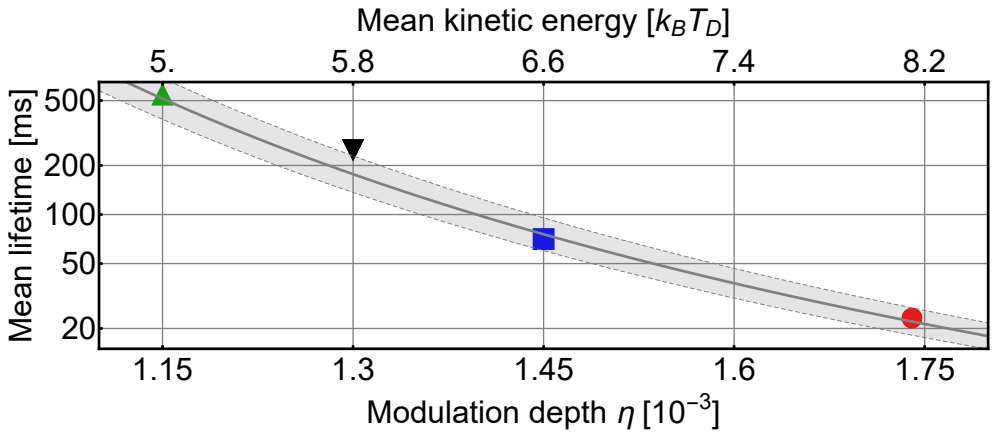

Figure 4.8: Experimentally obtained mean lifetimes of the kink in dependence of the modulation depth η. The errorbars are hidden in the symbols of each datapoint.
In addition we derive the mean lifetime of the kinks by numerical studies and approximated Kramers' model to the data. The result is shown by the gray line. The uncertainty of the approximation is indicated by the light gray corridor. Based on the interpolation function in eq. 4.3, we can rescale η to a mean kinetic energy as shown on the upper x-axis. Kramers' model gives a barrier height in terms of energy of $(24.2 \pm 0.7)\ T_\mathrm{D}$.

barrier, originally developed to describe rates in chemical reactions. Thus, we obtain by this approach the mean lifetimes of structural defects trapped inside, a lower bound of the trap depth of the Peierls-Nabarro based on the internal dynamics of the ion crystal.

There are several assumption in the derivation, so this is only an estimate of the barrier height of the Peierls-Nabarro potential. We use models to describe the dynamics of the system and to determine relevant timescales to calculate for instance the viscosity $\xi_\mathcal{K}$. Self-diffusion and the viscosity described by Raman and Andrade are developed to describe dynamical aspects in the liquid phase of systems of infinite size.
The approach $\propto T^{-\alpha/2}$ takes the dimensionality of the system into account. A kink inside a two dimensional ion crystal can move only along the crystals x-axis. So the dimensionality of the system is reduced to one degree of freedom the kink can move along.

Beside this, our extension of Kramers' model presumes a symmetric barrier to the left and to the right, as we reduce the mean lifetime by a factor of two. The Peierls-Nabarro potential depends strongly on the trapping potential, as shown in [35]. An assymetric trapping potential would lead to barriers of different height. The x-coordinate of center of mass, illustrated by the red line in fig. 3.4 (e) and (f), is shifted to the left of both central ions. So the ion distribution is more dense to the left than to the right.

Chapter 5

Transformation and dynamics of structural defects inside Coulomb crystals

In the previous chapter, we evaluated the SSP based on the differentiation of kinks and zigzags. However, the experimental data contains in a statistical relevant manner six crystalline configurations. We already introduced in chapter 3.3 four configurations of kinks and two zigzags. In the following, we want to study the structure transformation probability seperately for each configuration.
In the first part of this chapter, we focus on the transformation dynamics of individual structures due to the increase of the internal energy in the presence of the external drive. In the second part the directionality of escape out of the Peierls-Nabarro (PN) potential is discussed individually for each configuration of kink. Based on the shape of the ion crystal derived from the experimental data, we extend the harmonic confining potential of the Paul trap by higher order terms and suggest an explanation for the preferred escape directionality.

5.1 Structure survival probability of individual conformations

In this chapter, we are interested in the conformational resolved dynamics of each type of kink in the presence of the quadrupol modulation, as shown in fig. 3.4. First, we discuss the influence of certain modulation depths on each configuration of the ion crystals. In the second, part we show the results for selected kink configurations comparing several modulation depths.

5.1.1 Fixed modulation amplitude

The experimental data in fig. 4.2 (a) (III) depict a kink moving to the right during the exposure time (150 ms) of the CCD camera. Up to now, we analysed video frames to decide, whether there was a kink in the crystal or whether there was a pure zigzag. To study the dynamical aspects in more detail, we analyse the data based on each of the individual conformations of the ion crystals, as listed in fig. 3.4.
Thus, we can identify transformations between certain structures and decay mechanisms of the kink containing structures to zigzags.

Analysis of measurements with $\eta = 0$

To study the effect of the external modulation, first, we have to analyze the data recorded for modulation $\eta = 0$, as shown in fig. 5.1. Without modulation the crystalline conformations survive in about 90% t_{mod} of 1000 ms. We first seperate the experimental data based on all six initial configuration detected during step 2. To increase statistics, we individually sum up modulation duration between 400 ms and 1000 ms. The results depicted as matrix in fig. 5.1, indicate that almost all structures stay in their initial configuration during t_{mod} as the diagonal elements show at least 81% structure survival probability. The ratio of each structure represents the recorded configuration in step 4 normalized to all initially detected. The upper and lower number on the right depict the 1σ interval based on binomial statistics. The data is rescaled by background gas collisions in that sense, that we averaged the transfer ratios of Zigzag to $\overline{\mathrm{Zigzag}}$ and vice versa and substract them from the whole set of data. Thus, a Kink8, for instance, survives the modulation duration with a ratio of $0.92\,^{+0.03}_{-0.04}$. Within the errorbars the stability of $\overline{\mathrm{Kink8}}$ and $\overline{\mathrm{Kink10}}$ is similar, but less stable than in the case of Kink8 and Kink10. In addition crystal with kink are less stable than zigzag configurations. This might be explained by the finite lifetime of these crystalline structures, due to the finite depth of the Peierls-Nabarro potential.
The last row represents frames recorded during step 2 that do not fit to any of the given structures. This is most times related to residual dynamics, like a kink escaping the crystal, during exposure time and the process of recrystallization. Two third of these are identified in step 4 as zigzags, the configuration of minimal energy, but statistics is not the best.

Mean lifetime of all of these crystalline structures is sufficient to study effects on timescales beyond 1000 ms.

Analysis of measurements with $\eta = 1.30 \times 10^{-3}$

We discuss in the following the influence of the modulation, resulting in an increase of internal energy allowing dynamics, like structural transformation. Considering only

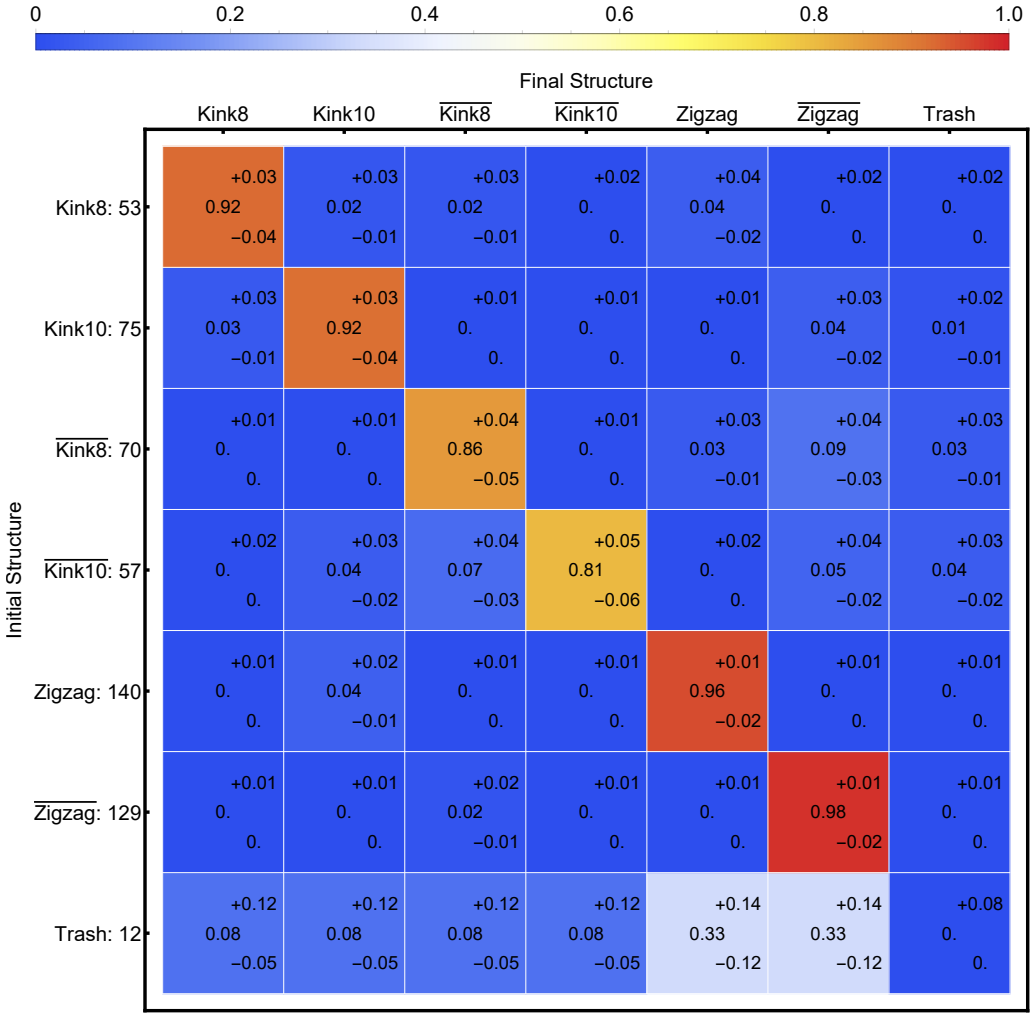

Figure 5.1: Conformational dependency of structure transformation probability with modulation $\eta = 0$. Full structural analysis is shown in the basis set defined in fig. 3.4. The structures recorded and identified in step 2 (see fig. 3.3) are listed on the left side as initial configuration. In addition, the number of analysed crystals for each configuration is listed. In the upper row, the identified structures from step 4 are listed. Diagonal entries of the matrix are brigth and indicate that initial and final structure are identified as the same. In addition, ratios of each combination are given and illustrated in the color scheme from blue via white and yellow to red, indicating high ratios in red and small ones in blue. The ratios are rescaled to consider the limited lifetime of crystalline structures, indicated by of the transfer rate between zigzag and $\overline{\text{zigzag}}$.
Errors as listed in the figure (above and below the central value) are calculated based on binomial statistics and indicate the 1σ interval. The probability for crystals with kink to survive is smaller than for zigzag crystals.

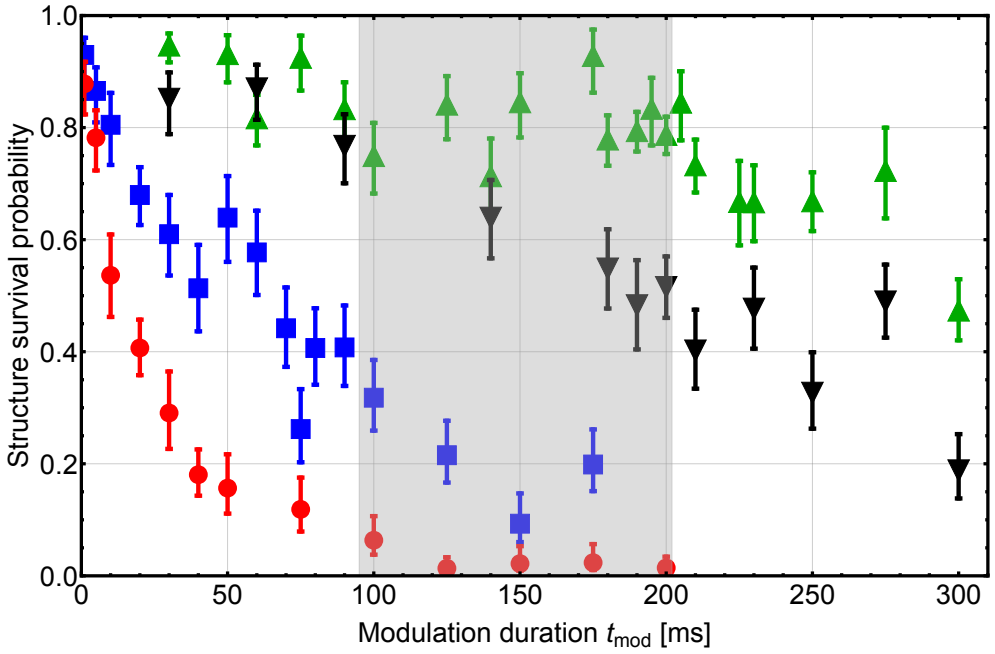

Figure 5.2: Structure survival probability as a function of the modulation duration t_{mod}, as shown in fig. 4.3. The gray shaded area indicates the data selected for the following studies. The time span is chosen as there are measurements for all modulation depths $\eta \times 10^3 \in \{1.15, 1.30, 1.45, 1.74\}$ and the transformation signal to noise in the case of weak modulation is maximal.

data for t_{mod} between 100 ms and 200 ms, as highlighted by the gray shaded area in fig. 5.2, we have a comparable set of data for all four modulation depths, corresponding to different internal energies. We analyzed the data obtained for a modulation depth $\eta = 1.30 \times 10^{-3}$ the same way as for $\eta = 0$. The matrix is shown in fig. 5.3 and discussed in the following. Zigzag crystals survive with the same probability as in the undisturbed case. However, crystals with kink are transformed and kinks are driven out of the crystal: Kinks initialized as Kink8 are transferred to Kink10 or driven out of the crystal, such as the video frame in step 4 shows a $\overline{\text{Zigzag}}$ or Zigzag with equal ratios. The transformation of the kink can be understood as a reorganisation of the two ions at the center of the crystal, as depicted in fig. 5.4 (a). Defects of type Kink10 stay in their configuration and only about 10% are transferred to a Kink8. The ratios for a transformation to one of the zigzag configurations are similar to those of Kink8. $\overline{\text{Kink8}}$ is as stable as Kink10. It has a preference to be transformed to a Zigzag, if the kink is driven out of the crystal. In the case of $\overline{\text{Kink10}}$, the major part is detected in step 4 as $\overline{\text{Kink8}}$ configuration. The survival ratio of $\overline{\text{Kink10}}$ is about 8%, similar to the structure transformation ratio from $\overline{\text{Kink8}}$ to $\overline{\text{Kink10}}$, see fig. 5.3. Based on the data, we can not identify, whether $\overline{\text{Kink10}}$ survives, or is transformed to a $\overline{\text{Kink8}}$ configuration which is transformed back, as scetched in fig. 5.4 (b). Data obtained for an intial configuration $\overline{\text{Kink8}}$ shows a relevant transformation to $\overline{\text{Kink10}}$.

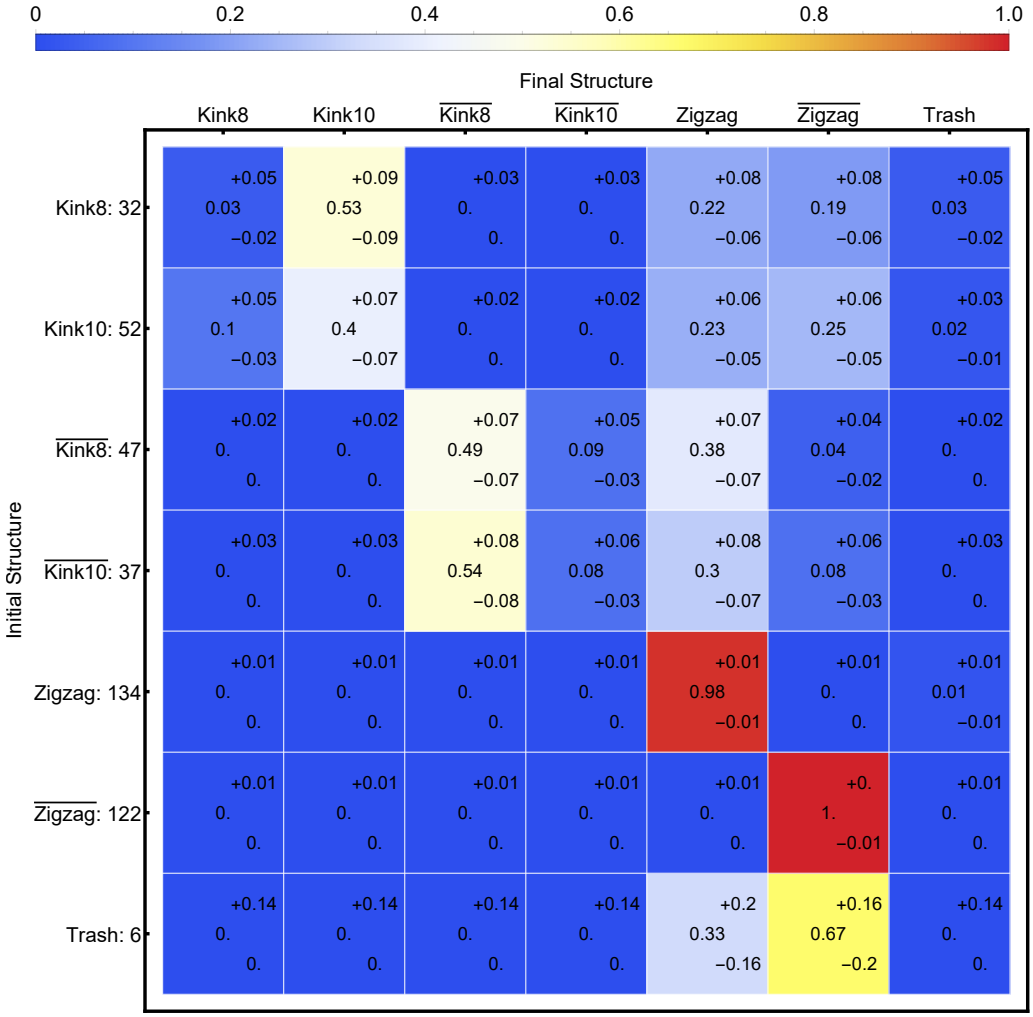

Figure 5.3: Conformational dependency of structure transformation probability with a modulation depth $\eta = 1.30 \times 10^{-3}$.
Data processing and labeling is identical to fig. 5.1. Kink8 ($\overline{\text{Kink10}}$) is transferred to Kink10 ($\overline{\text{Kink8}}$), whereas Kink10 and $\overline{\text{Kink8}}$ are stable as initial configuration, or decay to zigzag structures. The survival ratios of Kink8 and $\overline{\text{Kink10}}$ are similar. Further investigations have to be performed to clearify, whether the configurations survive or they are transformed from Kink10 ($\overline{\text{Kink8}}$).
Kinks are transformed almost equally to Zigzag and $\overline{\text{Zigzag}}$. However, for $\overline{\text{kinks}}$, there is a preference for the Zigzag configuration.
Crystals without kinks are not disturbed by the modulation, as there is no eigenmode in spectral range of excitation.

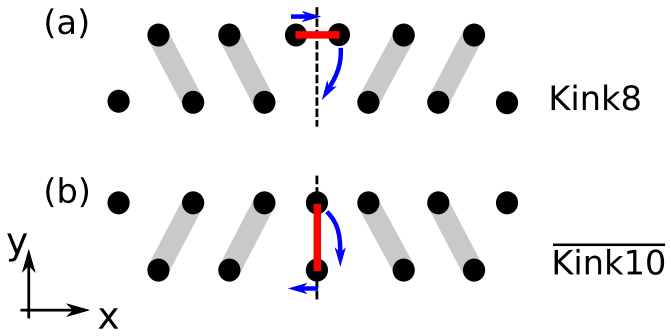

Figure 5.4: Schematics of the central part of an ion crystal with a kink depicting the configurational change as revealed by the experimental data. The dashed black line indicates the symmetry axis. The position of the ions connected by a red bar defines the type of kink. Blue arrows indicate the moving direction of the ions related to the transformation.
(a) Transformation of a Kink8 to a Kink10: The central ions are located in the upper string of ions. One of them crosses the crystal axis, whereas the other moves slightly to the middle.
(b) $\overline{\text{Kink10}}$ is transformed to a $\overline{\text{Kink8}}$. The ions located next to the x-coordinate of the CoM rearrange their position inside the crystalline structure, as both are finally located at the lower ion chain.

Both structures are stable for long time for $\eta = 0$, so their configurations are separated by a structural energy barrier, that prohibits the ions from crossing the crystal axis. The prescence of the modulation $\eta > 0$ rises the energy inside the system that the ions can cross the energy barrier and the kinks are transformed. In parallel laser cooling damps the system that the motion of the ions is damped and they equilibrate to their position given by the configurations of less energy.
Further numerical studies are neccessary to evaluate the amount of energy that is neccessary to overcome the internal energy barrier to transform a Kink8 ($\overline{\text{Kink10}}$) to a Kink10 ($\overline{\text{Kink8}}$). First estimations reveal a barrier height of less than $3\,k_\text{B}\,T_\text{D}$. We have to set up a system of transformation rate equations, to derive quantitative results from the numerical simulation comparable to the experimentally derived transformation matrices.

Kinks can only change their structure to anti-kink configurations during melting the crystalline structures and a recrystallization, a first order phase transition. As discussed already above, this would lead in the case of a zigzag to at least in one half of the cases to a kink containing structure. Such events would be listed as off-diagonal contributions in the transformation matrix, in the row of the crystals initialized as zigzags.

Until now, I discuss the structural change of the crystalline configuration for a modulation depth $\eta = 1.30 \times 10^{-3}$. Data analysis is done for all different modulation depths and is presented in the appendix A.1.

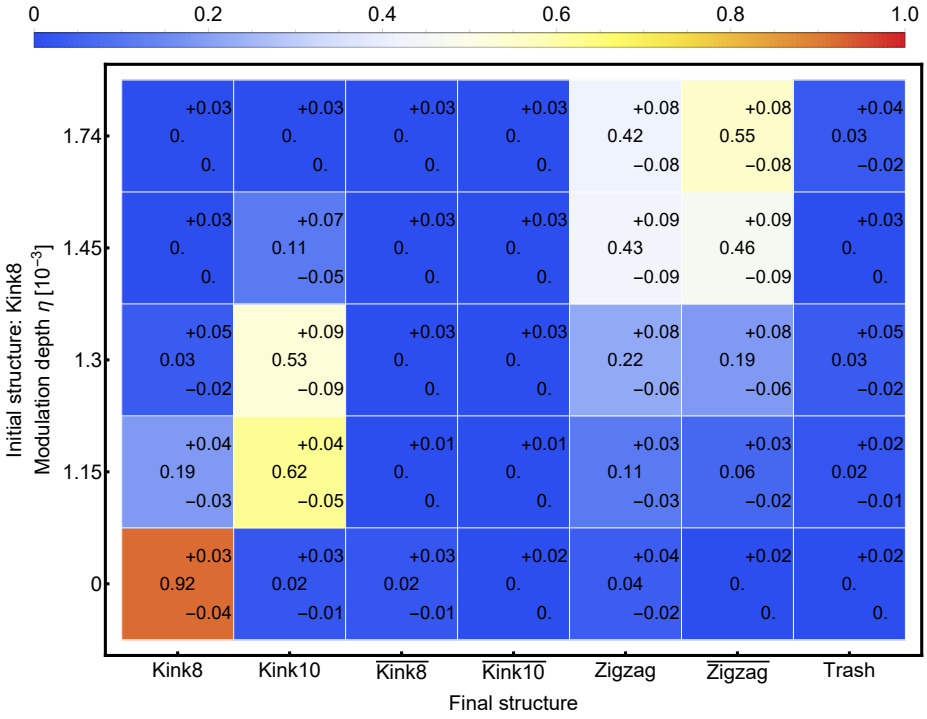

Figure 5.5: Transformation dynamics of Kink8 in dependence on η:
Data evaluation is performed the same way as before, for details see fig. 5.1 and text. We label the columns based on the six crystal configurations. The vertical axis gives the modulation depth analysed in each of the rows. We select the dataset with Kink8 as initial configuration and study in dependency on the modulation depth the resulting structure, recorded during step 4 in the experimental sequence.
Kink8 is first transferred to a Kink10 and for stronger modulation most Kink8 are transformed to zigzag and $\overline{\text{zigzag}}$ crystals in similar ratios.

5.1.2 Resolving structural changes of an individual type of kink

The set of data is limited, so a statistical relevant analysis of each configuration on more than one timestep is not possible. As numerical studies confirm, the crystal is heated by the quadrupol modulation. Instead of analyzing several modulation durations t_{mod}, we compare the four different modulation depth, as shown in fig. 5.2. As discussed before, the structure survival probability decays exponentially, see fig. 4.3. This approach can be interpreted as a study of a weak modulation for several times.
Data is processed and presented as described above. However, we select in this evaluation one configuration of the kinks and compare the structure transformation probability for several modulation depths η, as shown in fig. 5.5. Columns are labeled with the structures obtained in step 4. In vertical direction, the modulation depth increases from $\eta = 0$ to $\eta = 1.74 \times 10^{-3}$.

First, we discuss the experimental results of Kink8 to gain deeper insight in the trans-

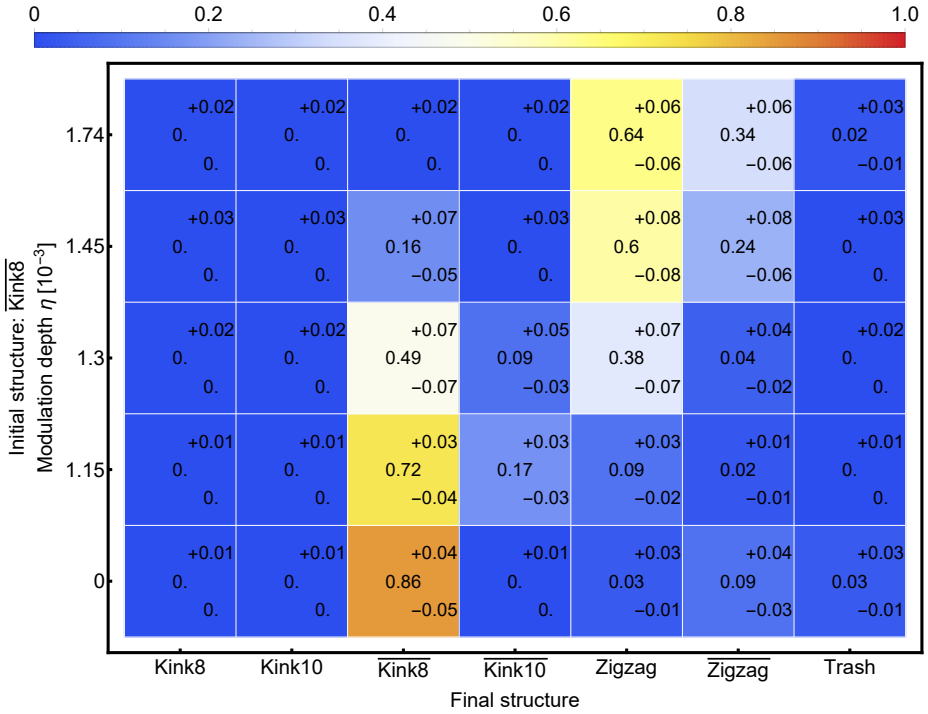

Figure 5.6: Decay dynamics of $\overline{\text{Kink8}}$ in dependence on η:
Data evaluation is performed as discussed already in the context of fig. 5.5.
We select the dataset with $\overline{\text{Kink8}}$ as initial configuration and studied in dependency of the modulation depth (vertical axis) the resulting structure, recorded during step 4 in the experimental sequence.
$\overline{\text{Kink8}}$ is only transformed for weak modulation with a ratio of 1:4 to a $\overline{\text{Kink10}}$. Increasing the modulation results to a transformation of 2:1 to a Zigzag as the preferred configuration in comparisom with $\overline{\text{Zigzag}}$.

formation process and study the appearance of different conformations. On the left bottom Kink8 stays itself, as the modulation depth $\eta = 0$. Increasing the modulation depth leads a transformation of Kink8 to other structures. The crystals are transferred to a Kink10 configuration with a ratio of about 1:3. Further increasing the modulation, the configuration Kink8 is transformed to Kink10 or is driven out of the crystal.
There are no contributions in the columns of $\overline{\text{kink}}$, as discussed above.
Kinks are transformed in almost equal ratios to Zigzag / $\overline{\text{Zigzag}}$ and appear for all modulation depths with similar probabilities within the errorbars. This analysis reveals that a Kink8 is transformed to a Kink10 and for stronger modulation leaves the PN potential. As modulation depth corresponds to internal energy, the transformation of kinks is relevant only for energies small compared to the depth of the Peierls-Nabarro potential.
The data analysis is done for the Kink10 the same way, as shown in fig. A.4. The structure survival rate of Kink10 decreases with an increase of the modulation depth.

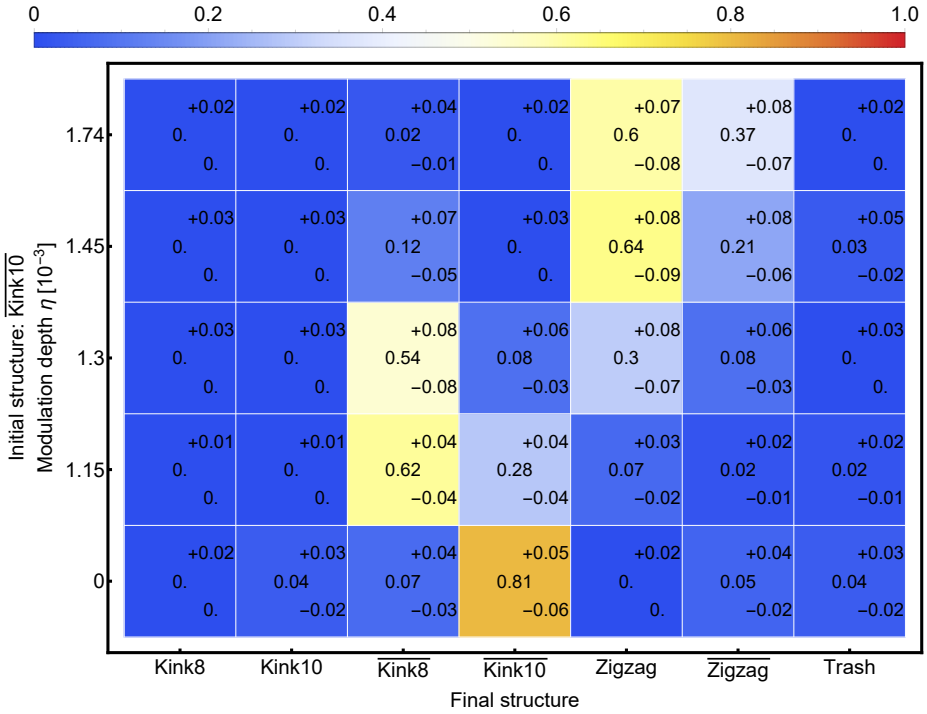

Figure 5.7: Decay dynamics of $\overline{\text{Kink10}}$ in dependence on η:
Data evaluation is performed as discussed already in the context of fig. 5.5.
We select the dataset with $\overline{\text{Kink10}}$ as initial configuration and studied in dependency of the modulation depth the resulting structure, recorded during step 4 in the experimental sequence. As indicated by the bright entries of the array plot, $\overline{\text{Kink10}}$ is first transformed to a $\overline{\text{Kink8}}$ with a ratio of 2:1. For stronger modulation it is further transformed to a Zigzag.

The zigzags increase with similar ratios in the case of Kink8. Kink10 configurations are transformed to Kink8, but not in a comparable amount as the Kink8 decays to a Kink10.

The analysis of $\overline{\text{Kink8}}$ and $\overline{\text{Kink10}}$ configurations reveals a different dynamic compared to kinks. We discuss the $\overline{\text{Kink8}}$ first. Its decay dynamics for individual modulation depths is shown in fig. 5.6. Configurations of kinks are not created during the decay, as this is only possible in the case that the whole crystalline structure is dissolved. Weak modulation leads to a transformation from $\overline{\text{Kink8}}$ to $\overline{\text{Kink10}}$ in one out of four cases. However, the configurations created by this transformation get lost with an increase in modulation. The configuration $\overline{\text{Kink8}}$ is more stable, as they appear for stronger modulation in the data. Further increasing the modulation to $\eta = 1.74 \times 10^{-3}$ all $\overline{\text{Kink8}}$ are transformed to the zigzags.
The ratio of transformation of $\overline{\text{Kink8}}$ to a Zigzag configuration is for all modulations depths ($\eta \neq 0$) at least twice the ratio compared to $\overline{\text{Zigzag}}$.

Analyzing decay dynamics of the crystal configuration $\overline{\text{Kink10}}$, we obtain a similar picture as for Kink8 crystals. However, applying the modulation leads in first place to a change in conformation from $\overline{\text{Kink10}}$ to a $\overline{\text{Kink8}}$ and decays similarly as $\overline{\text{Kink8}}$ to its preferred conformation, the Zigzag. Comparing $\overline{\text{kinks}}$ initialized as $\overline{\text{Kink10}}$ and $\overline{\text{Kink8}}$, the ratio of 0.3 for a $\overline{\text{Kink10}}$ to stay in the presence of the modulation $\eta = 1.15 \times 10^{-3}$ a $\overline{\text{Kink10}}$ is significant larger than the transformation ratio of 0.2 to be created from a $\overline{\text{Kink8}}$. So two third of the ratio listed as survival probability might be interpretated as transformation ratio originally coming from the $\overline{\text{Kink8}}$. $\overline{\text{Kink}}$ is transformed via $\overline{\text{Kink8}}$ to the Zigzag configuration with twice the probability as for $\overline{\text{Zigzag}}$.

The experimental data shows transformation processes, that might indicate the relative conformational energy of each type of crystal. During the transformation the ions have to overcome the energy barrier seperating the upper and the lower ion chain. The modulation of the trapping potential transfers energy to the bath of phonons via nonlinear mode coupling and increases the internal energy of the crystal, thus a transformation gets reasonable. In the experiment, laser cooling is present during the modulation. The damping rate given by the laser cooling is similar to the phonon excitation, as discussed in chapter 4. This is evidenced by the fact, that we record a second frame in our experimental sequence (step 4) identifiable crystalline structure of different kink configuration. The ions motional excitation has to be damped by laser cooling rate, otherwise the ion crystal would not be stabilized in a well distinguishable configuration, different to the inital one. The ratio of kinks that change their configuration during the experimental sequence, enables us to estimate the relative conformational energy of kinks and $\overline{\text{kinks}}$: Kink10 is the structure of lower energy compared to Kink8, as it is transferred to Kink10 and the inverse process is supressed. For $\overline{\text{kink}}$ configurations, $\overline{\text{Kink8}}$ is the energetic more favorable configuration compared to $\overline{\text{Kink10}}$.

These transformation processes have to be studied further and this has to be supported in detail by numerical studies. In addition, the influence of the trapping potential of our Paul trap on the transformation dynamics has to be studied in detail by numerics. It would be helpful to calculated the conformational energies and energy barriers an ion has to overcome to move from the lower to the upper chain of the ion crystal, as shown in fig. 5.4. Afterwards, we might set up a system of rate equations to describe these processes in quantitative way and proof whether these explanations are realistic.

5.2 Experimental test on the symmetry of the Peierls-Nabarro potential

We have labeled our conformations based on the position of the forth ion from the right side. Camera frames reveal dynamics of reorganization in one half of the crystal, see fig. 4.2 (a) (III). So a kink leaving the crystal to on side leads to a rearrangement

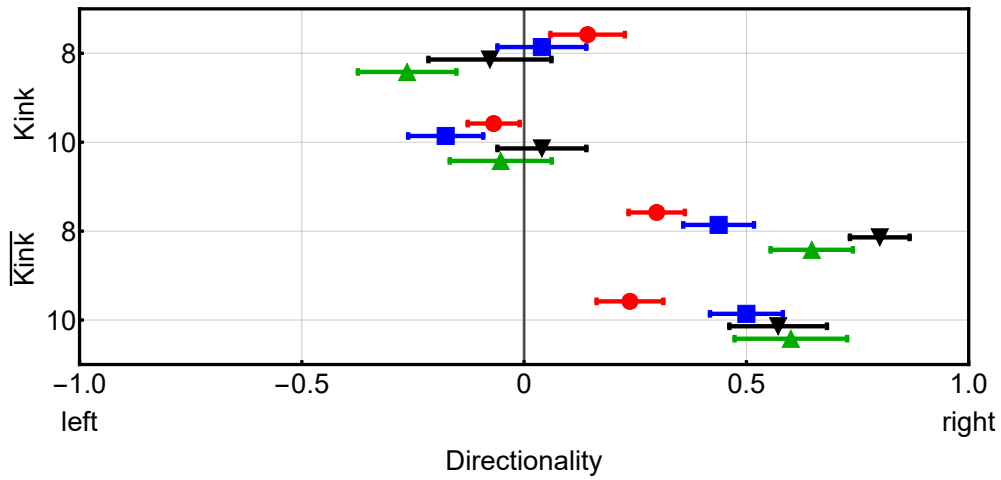

Figure 5.8: The experimentally derived transport directionality (TD) for kinks and $\overline{\text{kinks}}$. TD is defined as a the difference of the probabilities to move to the right and to the left normalized to the sum of all kinks driven out of the PN potential. If both ratios are similar, TD will amount to zero. The color coding is related to the modulation depth $\eta \times 10^3 \in \{1.15, 1.30, 1.45, 1.74\}$ by {green, black, blue, red}, as introduced in fig. 4.3.
The TD of kink configurations is within $2\,\sigma$ in agreement with zero, so there is no preference to leave the crystal to left or to right. Comparing Kink8 and Kink10, both configurations show the same directionality within 2σ for each modulation depth.
In the case of $\overline{\text{kink}}$, more defects leave the crystal to the right than to the left. Both configurations have similar directionalities for a chosen modulation depth. A weak modulation shows a stronger directionality than a strong modulation.

of the ions on this side. In the theory part, we discussed the spin chain analogon to illustrate the domain wall. A pure zigzag is described by $(\cdots \uparrow\uparrow\uparrow\uparrow\uparrow\uparrow\uparrow\uparrow \cdots)$ and a crystal with a domain wall by $(\cdots \uparrow\uparrow\uparrow\uparrow\downarrow\downarrow\downarrow\downarrow \cdots)$. If a kink leaves the crystal to the right, it would result in: $(\cdots \uparrow\uparrow\uparrow\uparrow\uparrow\uparrow\uparrow\uparrow \cdots)$. But moving to the left would result in a crystalline structure that appears like $(\cdots \downarrow\downarrow\downarrow\downarrow\downarrow\downarrow\downarrow\downarrow \cdots)$. In the first case, the labeling of the conformation (Kink $\rightarrow$ $\overline{\text{Zigzag}}$) is changed due to the loss of kink, in the latter the position of the ions in the right part did not change, but the configuration is labeled as a Zigzag. So we consider the resulting structure and derive the motional direction of the kink.

The data analysis above focuses on the internal dynamics, how a kink is transformed to another.
As discussed before, kinks and $\overline{\text{kinks}}$ are transformed to other configuration, but at a certain time, they gain enough energy to overcome the barrier and they can escape from the Peierls-Nabarro (PN) potential. In chapter 2.4.3 and 4.3.2, we discuss the extension the Kramers' model with a second barrier of same height to consider the axial symmetry of the crystal. The transformation of the kinks to zigzags can be used

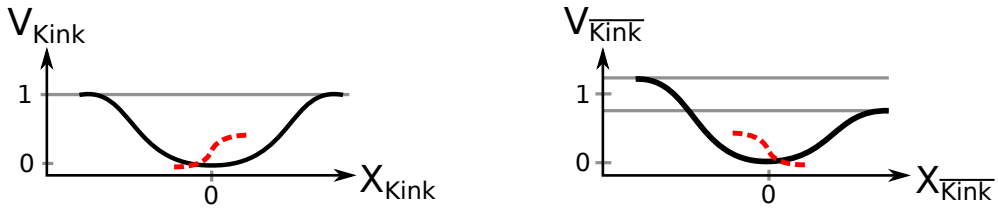

Figure 5.9: Schematics of the structure dependency of the Peierls-Nabarro potential. Kinks are confined inside their self induced trapping potential, the Peierls-Nabarro potential. Kinks have a symmetric potential, whereas $\overline{\text{kinks}}$ have an asymmetric confinement along the x-axis of the crystal. However, this depends on higher order terms in the trapping potential of the Paul trap, for details see text.

to confirm the extension of the PN potential.

In the following, we focus on the initialized kink structure and the final zigzag conformations, to study the direction of motion of the structural defect. A kink moves to the left or to the right in these crystalline structures. The set of data taken into account is the same as in the chapter before, evaluating the data with an initialized kink, that is transformed to one of the zigzags. We calculate the ratio of kinks vanishing to the right and to the left separately. The ratio to the left is substracted from the ratio of kinks moving to the right. The results are individually depicted for all four types of kinks in fig. 5.8. The colors represent the modulation depth, as already introduced in fig. 4.3. The errorbars represent binomial statistics based on the sample size.
Datapoints derived for kinks are located around zero, so the amount of kinks leaving the crystal to the right is the same as to the left. There is no obvious dependency on the modulation depth, as the green datapoint is within $2\,\sigma$ compatible with zero.
In the case of $\overline{\text{Kink}}$, there is a preference leaving the crystral to the right. Thus, $\overline{\text{Kinks}}$ counterpropagate the $\vec{k}_{\text{L}}$ of the cooling laser and with this it can not be epxlained by any effect due to light pressure. The amount of directionality depends on the modulation depth η. Small η results to a strong directionality, whereas an increase of η leads to a loss in directionality.

In the chapter before, we study the mean lifetime of the defects in dependency on the modulation depth, see fig. 4.3. As numerical studies reveal, the mean lifetime is related to the internal energy of the system. A weak modulation results to a small increase of internal energy in comparism with the depth of the PN potential. As the damping by the laser and the external modulation result to an equilibrium state, the difference in the barrier height is resolved for weak modulation by the kink itself. Whereas a strong modulation leads to fast transformation of the $\overline{\text{kink}}$ to a Zigzag. Similar to kink configurations, the directionality of escape is not sensitive to being a $\overline{\text{Kink8}}$ or a $\overline{\text{Kink10}}$. This similarity might be caused by the kink transformation mechanism, as discussed in chapter 5.1. Kinks decay mostly via the Kink10 configuration, and for

$\overline{\text{kink}}$ configurations the $\overline{\text{Kink8}}$ seems to be relevant.

Based on the experimental data, we have a configuration dependency in the escape directionality. We can interprete the experimental results in the context of the PN potential. Kinks are trapped inside a symmetric potential, whereas the $\overline{\text{Kinks}}$ exploit an assymmetric one, see fig, 5.9.

The crystalline structures, as depicted in fig. 3.4, are slightly assymmetric, so we evaluate the ions' position and calculate the center of mass, as discussed in chapter 3.3. In this way, we use our ion crystal to sense the potential of our linear Paul trap.

This derivation hints that we have to take higher order terms into account to describe the trapping potential. With the help of the experimentally derived coefficients, we can extend the numerical simulation by third and forth order terms in axial as well as radial direction. We extend the trapping potential in the numerical simulation by anharmonicities in the potential: $\lambda_1 x^3 + \lambda_2 x^4 + \lambda_3 y^3 + \lambda_4 y^4$.
With the help of simulation code, we derive the conformational energy at each timestep. As we are interested in the transition state, almost at the top of the PN potential barrier, we first have to move the kink to one side of the crystal and search for the outermost stable position. This is done several times to ensure that the routine delivers similar kink configuration and energies of the system. Comparing the energy for a configuration with a kink to the side and a crystal with a kink at the center, we calculate the energy difference and assume that this amounts to the energy a kink has to gain for an escape from the PN potential. In this way, we can calculate each barrier for all types of kinks with respect to the anharmonicities of the trapping potential. It gives a hint on the preferred escape direction, as we assume that the kink leaves the crystal on the side of the lower barrier. These first results, as shown in fig. 5.10, derived by this method are in qualitative agreement with our experimental data.
Taking the eight barriers into account, we derive a mean average of $25.3\,k_\mathrm{B}\,T_\mathrm{D}$. The numerical results represent the barrier height of each configuration of kink, see fig. 5.10. The mean branching in the barrier heights related to the nonlinearities is in the order of $2\,k_\mathrm{B}\,T_\mathrm{D}$, which is similar to the internal energy difference due to the modulation depths. The calculation of escape rates and transformation ratio, as discussed above, remains to be investigated.

Thus, $\overline{\text{kinks}}$ are sensitive to the higher order terms of the trapping potential and leave the crystal for weak modulation in the direction of the lower energy barrier. For given anharmonicities, we obtain a directionality in motion, which can be interpreted as transport effect. In a next step, it is worth to test, whether we can invert this effect by inverting the higher order terms of the Paul trap and drive for instance kink structures to the left.

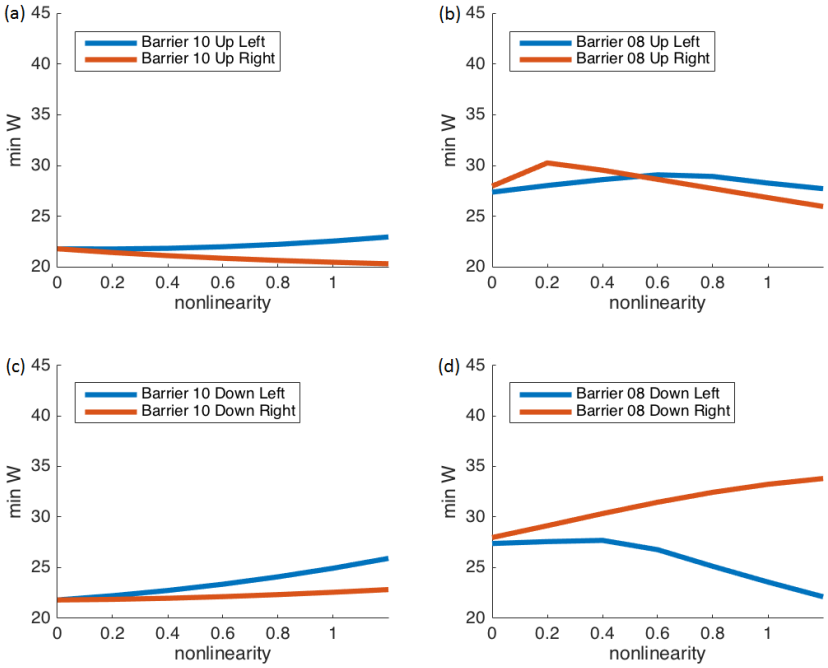

Figure 5.10: Numerical study on the individual barrier heights for each type of kink [62]. It is individually driven to the boarders of the crystalline structure and the internal energy of the crystal is calculated. The energy of the crystalline structure with the kink at the center is substracted. So we obtain the minimum energy $\min W$ of each barrier as a function of the normalized prefactors λ_i of the third and forth order of the trapping potential of the Paul trap. A nonlinearity of one indicates, that it amounts to the value as obtained by fitting the ions' position of the fluorescence images.
(a) Barrier height to the left (blue) and right (orange) of $\overline{\text{Kink10}}$: The barrier to the right is lower compared to the left.
(b) Barrier height to the left (blue) and right (orange) of $\overline{\text{Kink8}}$: The barrier to the right is lower than the left one.
(c) Barrier height to the left (blue) and right (orange) of Kink10: The right barrier is below the left one.
(d) Barrier height to the left (blue) and right (orange) of Kink8: The barrier to the left is in the order of $10\,T_{\mathrm{D}}$ lower than to the right.

Chapter 6

Conclusion and outlook

In this thesis, I present resonant excitation, mean lifetimes and directed transport of topological defects on timescales up to 300 ms. The eigenmode spectroscopy offers an conformational selective way to excite crystalline structures containing a soliton. Amplitude modulation of the quadrupol electric field of the RF trap rises the possibility to transfer energy in a well controlled way to the crystal without melting it, as it is shown by the lifetime measurements. A first estimate on the depth of the Peierls-Nabarro potential is derived from these measurements and amounts to $(24.2 \pm 1.0)\ T_{\mathrm{D}}$. In addition we can experimentally resolve energetic favorable conformations inside the trapping potential of our ion trap. The transport directionality of the solitons out of the crystal might offer a new way to study internal dynamics in crystalline structures.

We will study in the next steps the inversion of the transport direction, as we tune the anharmonicities with additional electric fields. So we expect, that there is a prefered directionality for the Kinks and the $\overline{\text{Kinks}}$ loose their preference to the right.
In addition we proceed with longer timescales of quadrupol modulation and see whether also in the case of weak modulation all kinks are driven out of the crystal.

As we have shown in [35], we are able to address single ions contributing the structural defect inside the crystal. In the high frequency spectral range, there is an eigenmode separated in frequency of tens of kHz from all the other normalmodes. This gap isolates the vibrational eigenmode from the rest of the phonon bath and reduces the intermode coupling.

A cooling of this localized vibrational eigenmode below Doppler temperature would rise the possibility to study reheating processes in the crystal. So we can measure internal mode coupling strength, which results in a study of system-bath interaction.
But to cool the eigenmode below the Doppler limit, we have first to install a Raman cooling setup at the experiment. There is already a well established approach by A. Friedenauer [71] for $^{25}Mg^{+}$. But we can also combine the approach by B. Hemmerling [73] in combination with a zeeman splitting of $^{24}Mg^{+}$ ions [74].

Bibliography

[1] H. Landa, B. Reznik, J. Brox, M. Mielenz, and T. Schaetz. Structure, dynamics and bifurcations of discrete solitons in trapped ion crystals. 15(9):093003, 2013.

[2] M. Mielenz, H. Landa, J. Brox, S. Kahra, G. Leschhorn, M. Albert, B. Reznik, and T. Schaetz. Trapping of topological-structural defects in coulomb crystals. *Phys. Rev. Lett.*, 110(133004), 2013.

[3] N. Wiberg. *Lehrbuch der Anorganischen Chemie (German Edition)*. Walter de Gruyter, 2007.

[4] J. Frenkel. Über die Wärmebewegung in festen und flüssigen Körpern. *Zeitschrift für Physik*, 35(8-9):652–669, 1926.

[5] I. Bloch, J. Dalibard, and W. Zwerger. Many-body physics with ultracold gases. *Rev. Mod. Phys.*, 80:885–964, 2008.

[6] Ch. Schneider, D. Porras, and T. Schaetz. Experimental quantum simulations of many-body physics with trapped ions. *Rep. Prog. Phys.*, 75(2):024401, 2012.

[7] R. Blümel, J. M. Chen, E. Peik, W. Quint, W. Schleich, Y. R. Shen, and H. Walther. Phase transitions of stored laser-cooled ions. *Nature*, 334:309, 07 1988.

[8] S. Kahra. *Trapping and cooling of single molecular ions for time resolved experiments*. PhD thesis, Ludwigs-Maximilians-Universität München, 2010.

[9] G. Leschhorn. *Time-resolved measurements on a single molecular target and Discrete Kink Solitons in Ion traps*. PhD thesis, Ludwig-Maximilians-Universität München, 2011.

[10] J. P. Schiffer. Phase transitions in anisotropically confined ionic crystals. *Phys. Rev. Lett.*, 70:818–821, Feb 1993.

[11] G. Piacente, I. V. Schweigert, J. J. Betouras, and F. M. Peeters. Generic properties of a quasi-one-dimensional classical wigner crystal. 69(4):045324, 2004.

[12] G. Morigi and S. Fishman. Dynamics of an ion chain in a harmonic potential. *Phys. Rev. E*, 70(6):066141, 2004.

[13] N. D. Mermin. The topological theory of defects in ordered media. *Rev. Mod. Phys.*, 51:591–648, 1979.

[14] R. Rajaraman. *Solitons and Instantons: An Introduction to Solitons and Instantons in Quantum Field Theory*. North-Holland Personal Library. North-Holland, 1987.

[15] T. Dauxois and M. Peyrard. *Physics of Solitons*. Cambridge University Press, 2006.

[16] H. Landa, S. Marcovitch, A. Retzker, M. B. Plenio, and B. Reznik. Quantum Coherence of Discrete Kink Solitons in Ion Traps. *Phys. Rev. Lett.*, 104:043004, 2010.

[17] A. del Campo, G. De Chiara, G. Morigi, M. B. Plenio, and A. Retzker. Structural Defects in Ion Chains by Quenching the External Potential: The Inhomogeneous Kibble-Zurek Mechanism. *Phys. Rev. Lett.*, 105:075701, 2010.

[18] T. W. B. Kibble. Topology of cosmic domains and strings. *Journal of Physics A: Mathematical and General*, 9(8):1387, 1976.

[19] T. W. B. Kibble. Some implications of a cosmological phase transition. *Physics Reports*, 67(1):183 – 199, 1980.

[20] W. H. Zurek. Cosmological experiments in superfluid helium? *Nature*, 317:505–508, October 1985.

[21] W. H. Zurek. Cosmological experiments in condensed matter systems. *Physics Reports*, 276(4):177 – 221, 1996.

[22] K. Pyka, J. Keller, H. L. Partner, R. Nigmatullin, T. Burgermeister, D. M. Meier, K. Kuhlmann, A Retzker, M. B. Plenio, W. H. Zurek, A. del Campo, and T. E. Mehlstäubler. Topological defect formation and spontaneous symmetry breaking in ion coulomb crystals. *Nature Communications*, 4:2291, 2013.

[23] S. Ulm, J. Roßnagel, G. Jacob, C. Degünther, S. T. Dawkins, U. G. Poschinger, R. Nigmatullin, A. Retzker, M. B. Plenio, F. Schmidt-Kaler, and K. Singer. Observation of the kibble–zurek scaling law for defect formation in ion crystals. *Nat Commun*, 4, 2013.

[24] S. Ejtemaee and P. C. Haljan. Spontaneous nucleation and dynamics of kink defects in zigzag arrays of trapped ions. *Phys. Rev. A*, 87:051401, 2013.

[25] T. Fujii, M. Nishida, and N. Hatakenaka. Mobile qubits in quantum josephson circuits. *Phys. Rev. B*, 77:024505, 2008.

[26] S. Marcovitch and B. Reznik. Entanglement of solitons in the frenkel-kontorova model. *Phys. Rev. A*, 78:052303, 2008.

[27] P. Binder, D. Abraimov, A. V. Ustinov, S. Flach, and Y. Zolotaryuk. Observation of Breathers in Josephson Ladders. *Phys. Rev. Lett.*, 84:745–748, 2000.

[28] A. Wallraff, A. Lukashenko, J. Lisenfeld, A. Kemp, MV Fistul, Y. Koval, and AV Ustinov. Quantum dynamics of a single vortex. *Nature*, 425(6954):155–158, 2003.

[29] H. A. Kramers. Brownian motion in a field of force and the diffusion model of chemical reactions. *Physica*, 7(4):284 – 304, 1940.

[30] H. L. Partner, R. Nigmatullin, T. Burgermeister, J. Keller, K. Pyka, M. B. Plenio, A. Retzker, W. H. Zurek, A. del Campo, and T. E. Mehlstäubler. Structural phase transitions and topological defects in ion Coulomb crystals. *Physica B: Condensed Matter*, 460:114 – 118, 2015. Special Issue on Electronic Crystals (ECRYS-2014).

[31] W. Paul. Electromagnetic Traps for Charged and Neutral Particles. *Nobel Lecture*, 1989.

[32] C. N. Cohen-Tannoudji. Nobel lecture: Manipulating atoms with photons. *Rev. Mod. Phys.*, 70:707–719, 1998.

[33] H. J. Metcalf and P. Van Der Straten. *Laser Cooling and Trapping.* Graduate Texts in Contemporary Physics. Springer-Verlag GmbH, 1999.

[34] N. Kjaergaard, L. Hornekaer, A.M. Thommesen, Z. Videsen, and M. Drewsen. Isotope selective loading of an ion trap using resonance-enhanced two-photon ionization. *Applied Physics B*, 71(2):207–210, 2000.

[35] P. Kiefer. Structural Defects in Coulomb Crystals. Master's thesis, Albert-Ludwigs-Universität Freiburg, 2015.

[36] A. Friedenauer, H. Schmitz, J. T. Glueckert, D. Porras, and T. Schaetz. Simulating a quantum magnet with trapped ions. *Nat. Phys.*, 4:757, 2008.

[37] H. Schmitz, R. Matjeschk, Ch. Schneider, J. Glueckert, M. Enderlein, T. Huber, and T. Schaetz. Quantum walk of a trapped ion in phase space. *Phys. Rev. Lett.*, 103:090504, 2009.

[38] D. J. Wineland and Wayne M. Itano. Laser cooling of atoms. *Phys. Rev. A*, 20(4):1521–1540, 1979.

[39] I. Schmager. Trapping of topological defects in coulomb crystals, 2015.

[40] H. L. Partner, R. Nigmatullin, T. Burgermeister, K. Pyka, J. Keller, A. Retzker, M. B. Plenio, and T. E. Mehlstäubler. Dynamics of topological defects in ion Coulomb crystals. *New J. Phys.*, 15(10):103013, 2013.

[41] O. M. Braun and Y. S. Kivshar. *The Frenkel-Kontorova Model: Concepts, Methods, and Applications*. Texts and Monographs in Physics. Springer, 2004.

[42] C. Cormick and G. Morigi. Structural Transitions of Ion Strings in Quantum Potentials. *Phys. Rev. Lett.*, 109(5):053003, 2012.

[43] L. L. Yan, W. Wan, L. Chen, F. Zhou, S. J. Gong, X. Tong, and M. Feng. Exploring structural phase transitions of ion crystals. *Scientific Reports*, 6(1):21547, 2016. Article.

[44] U. Schramm, T. Schätz, and D. Habs. Bunched crystalline ion beams. *Phys. Rev. Lett.*, 87:184801, 2001.

[45] U. Schramm, T. Schätz, and D. Habs. Three-dimensional crystalline ion beams. *Phys. Rev. E*, 66:036501, 2002.

[46] http://www.tau.ac.il/ quantum/projects/solitons.html, 08 2015.

[47] H. Landa. Coherence properties of discrete static kinks. Master's thesis, Tel Aviv University, 2009.

[48] H. Kaufmann, S. Ulm, G. Jacob, U. Poschinger, H. Landa, A. Retzker, M. B. Plenio, and F. Schmidt-Kaler. Precise experimental investigation of eigenmodes in a planar ion crystal. *Phys. Rev. Lett.*, 109:263003, 2012.

[49] E. B. Wilson, J. C. Decius, and Paul C. Cross. *Molecular vibrations: the theory of infrared and Raman vibrational spectra*. Dover Publications, New York, 1980.

[50] W. Demtröder. *Molekülphysik: Theoretische Grundlagen Und Experimentelle Methoden (German Edition)*. Oldenbourg, 2003.

[51] I. V. Hertel and C.-P. Schulz. *Atoms, Molecules and Optical Physics 2: Molecules and Photons - Spectroscopy and Collisions (Graduate Texts in Physics)*. Springer, 2014.

[52] H. Landa, A. Retzker, T. Schaetz, and B. Reznik. Entanglement Generation Using Discrete Solitons in Coulomb Crystals. *Phys. Rev. Lett.*, 113:053001, 2014.

[53] Robert Brown F.R.S. Hon. M.R.S.E. & R.I. Acad. V.P.L.S. Xxvii. a brief account of microscopical observations made in the months of june, july and august 1827, on the particles contained in the pollen of plants; and on the general existence of active molecules in organic and inorganic bodies. *Philosophical Magazine Series 2*, 4(21):161–173, 1828.

[54] A. Einstein. Über die von der molekularkinetischen Theorie der Wärme geforderte Bewegung von in ruhenden Flüssigkeiten suspendierten Teilchen. *Annalen der Physik*, 322(8):549–560, 1905.

[55] M. von Smoluchowski. Zur kinetischen Theorie der Brownschen Molekularbewegung und der Suspensionen. *Annalen der Physik*, 326(14):756–780, 1906.

[56] F. J. Demond, S. Kalbitzer, H. Mannsperger, and H. Damjantschitsch. Study of Si self-diffusion by nuclear techniques. *Physics Letters A*, 93(9):503–506, feb 1983.

[57] N. G. Van Kampen. *Stochastic Processes in Physics and Chemistry (North-Holland Personal Library)*. North Holland, 2011.

[58] M. S. Green. Markoff Random Processes and the Statistical Mechanics of Time-Dependent Phenomena. ii. Irreversible Processes in Fluids. *The Journal of Chemical Physics*, 22(3):398–413, 1954.

[59] R. Kubo. Statistical-Mechanical Theory of Irreversible Processes. i. General Theory and Simple Applications to Magnetic and Conduction Problems. *Journal of the Physical Society of Japan*, 12(6):570–586, 1957.

[60] C. V. Raman. A theory of the viscosity of liquids. 111:532, 1923.

[61] E. N. da C. Andrade. Xli. a theory of the viscosity of liquids.—part i. *The London, Edinburgh, and Dublin Philosophical Magazine and Journal of Science*, 17(112):497–511, 1934.

[62] H. Landa. *private communication*.

[63] P. Hänggi, P. Talkner, and M. Borkovec. Reaction-rate theory: fifty years after Kramers. *Rev. Mod. Phys.*, 62:251–341, 1990.

[64] T. Huber. *Optical Trapping of Barium Ions - Towards Ultracold Interactions in Ion-Atom Ensembles*. PhD thesis, Albert Ludwigs Universität Freiburg, 2014.

[65] Ju. Schmidt. Optical trapping of barium ions. Master's thesis, Albert Ludwigs Universität Freiburg, 2014.

[66] Huebner-Photonics. *C-Wave Manual*, 2016.

[67] I. Breunig. *Optisch parametrische Oszillatoren für die Erzeugung monochromatischen Lichtes im mittleren und fernen Infrarot*. PhD thesis, Rheinische Friedrich-Wilhelms-Universität Bonn, Januar 2009.

[68] M. Bujak. Spectroscopy of Topological Defects in Coulomb Crystals, 2017.

[69] W. M. Itano and D. J. Wineland. Laser cooling of ions stored in harmonic and penning traps. *Phys. Rev. A*, 25:35–54, 1982.

[70] S. Stenholm. The semiclassical theory of laser cooling. *Rev. Mod. Phys.*, 58:699–739, Jul 1986.

[71] A. Friedenauer. *Simulation of the Quantum Ising Model in an Ion Trap.* PhD thesis, Ludwigs-Maximilians-Universität München, 2010.

[72] P. S. Burada and B. Lindner. Escape rate of an active Brownian particle over a potential barrier. *Phys. Rev. E*, 85(3):032102, 2012.

[73] B. Hemmerling, F. Gebert, Y. Wan, D. Nigg, I.V. Sherstov, and P.O. Schmidt. A single laser system for ground-state cooling of $^{25}Mg^{+}$. *Applied Physics B*, 104:583–590, 2011.

[74] M. D. Barrett, B. DeMarco, T. Schaetz, V. Meyer, D. Leibfried, J. Britton, J. Chiaverini, W. M. Itano, B. Jelenković, J. D. Jost, C. Langer, T. Rosenband, and D. J. Wineland. Sympathetic cooling $^{9}Be^{+}$ and $^{24}Mg^{+}$ of for quantum logic. *Phys. Rev. A*, 68:042302, Oct 2003.

Appendix A

Additional experimental data

In this thesis, I present four modulation depth and six types of crystals in chapter 5. In the main part, I show characteristic figures, that are of interest for the discussion. Here, I add the figures, that might be of further interest for the reader.

A.1 Dynamical studies on the conformation resolved structure survival probability

In chapter 5.1, I individually discuss the experimentally derived structure survival probability of each conformation. Here the figures are shown that we obtain for a modulation depth $\eta \times 10^3 = \{1.15$ (fig. A.1), 1.45 (fig. A.2) and 1.74 (fig. A.3)$\}$.

In chapter 5.1.2, we discuss the individual decay mechanism of each type of kink. The figure with the dynamics of Kink10 is shown in fig. A.4.

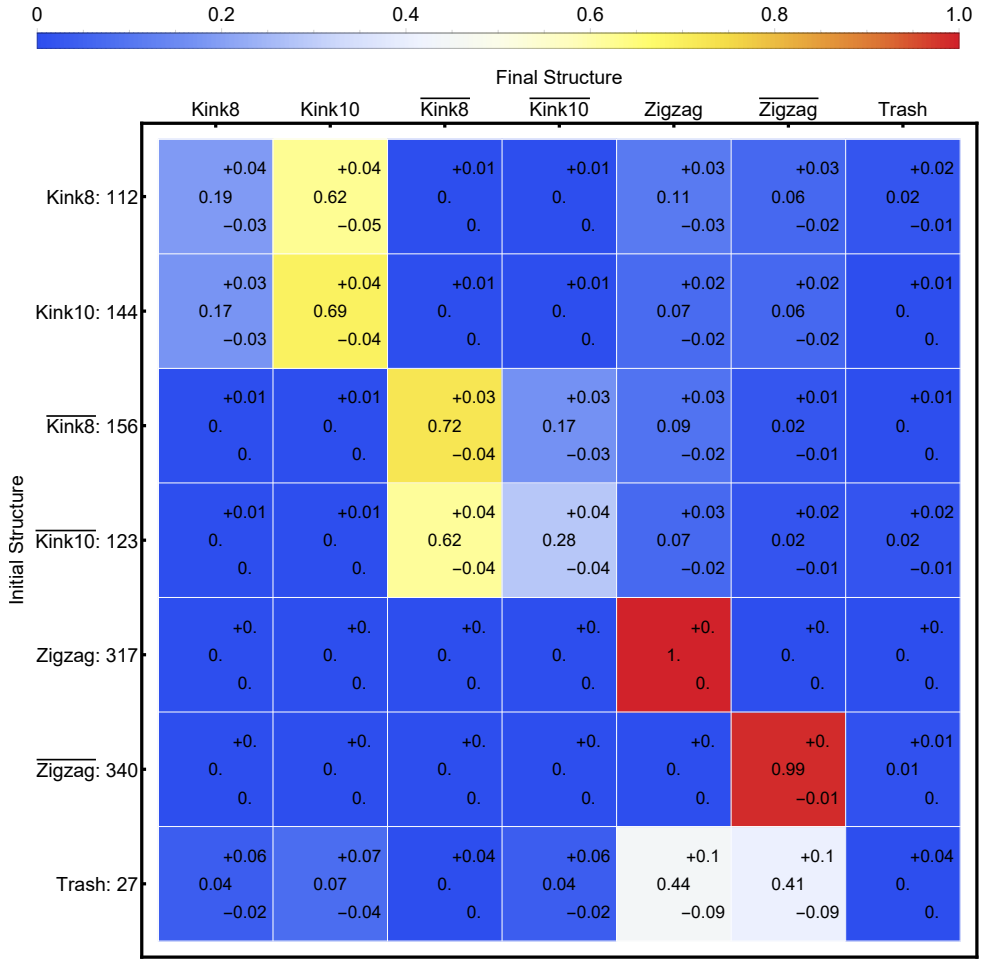

Figure A.1: Conformational dependency of structure survival probability with a modulation of $\eta = 1.15 \times 10^{-3}$.

Data processing and labeling is identical to fig. 5.1. The initial crystalline structure survives the modulation time with $\eta = 1.15$ as the same structure (labeled based on fig. 3.4) with different probabilities. Kink8 ([Kink10) are transformed in a significant way to Kink10 ($\overline{\text{Kink8}}$). The other way round is happens not that often, but is also present in the data. Only few kinks are heated out of the crystal. The zigzag crystals are not influenced by the modulation.

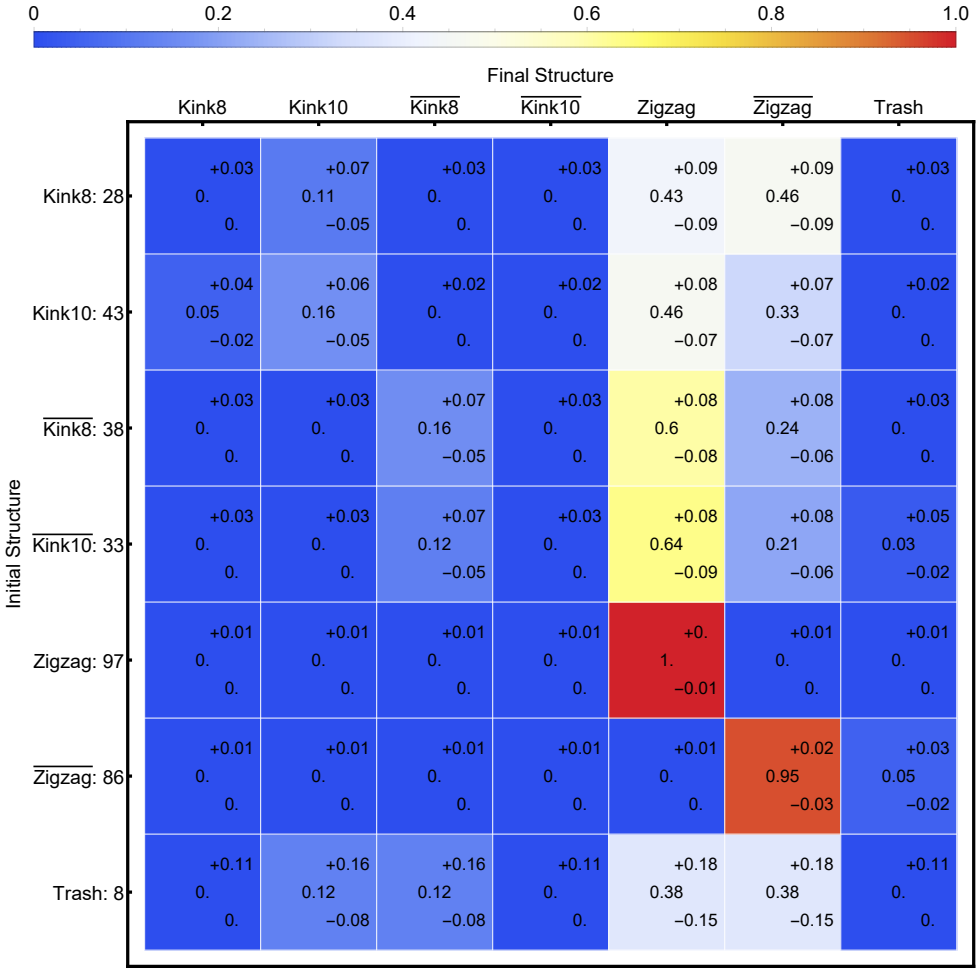

Figure A.2: Conformational dependency of structure survival probability with a modulation of $\eta = 1.45 \times 10^{-3}$.

Data processing and labeling is identical to fig. 5.1. The initial crystalline structure survives the modulation time with $\eta = 1.45 \times 10^{-3}$ as the same structure (labeled based on fig. 3.4). Most of the kinks are heated out of the Peierls-Nabarro potential. In the case of kinks both types appear within the errorbars with equal ratios. For $\overline{\text{kinks}}$ the Zigzag is more likely than the $\overline{\text{Zigzag}}$. The zigzags are not influenced by the modulation.

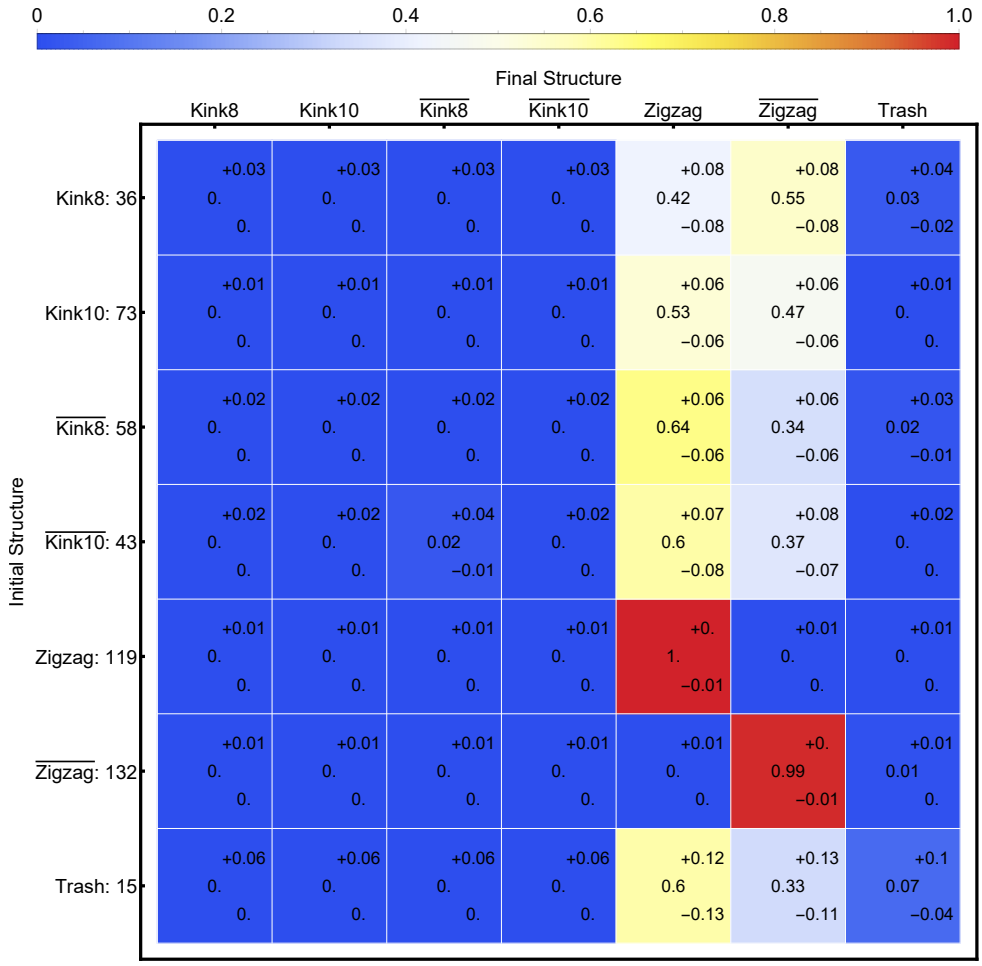

Figure A.3: Data processing and labeling is identical to fig. 5.1. The initial crystalline structure survives the modulation time with $\eta = 1.74 \times 10^{-3}$ only in the case of zigzags as the same structure (labeled based on fig. 3.4). Kink containing structures do not survive the modulation duration for this amplitude. Kinks leave the crystal in both direction, whereas $\overline{\text{kinks}}$ show a prefered direction to the right side.

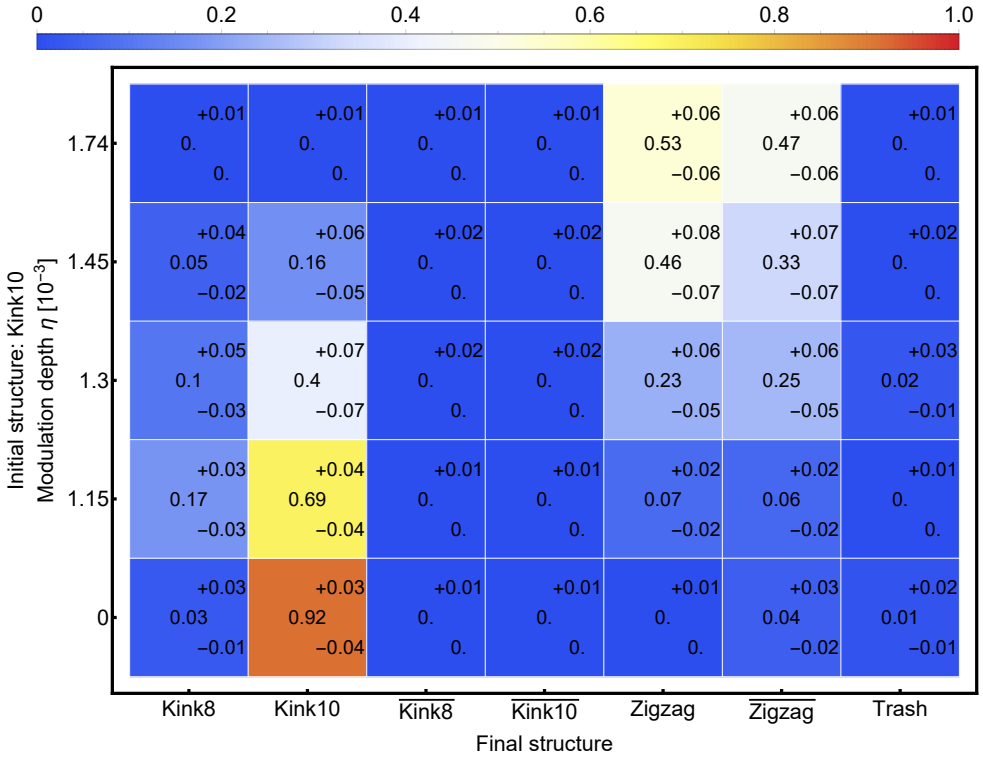

Figure A.4: Decay dynamics of Kink10:
The color scheme from blue via white and yellow to red, indicates high ratios in red and small ones in blue. The numbers of each cell represent the ratio normalized to the amount of studied crystals. Above and below are the bionomial errors.
We select the dataset with Kink8 as initial configuration and studied in dependency of the modulation depth the resulting structure, recorded during step 4 in the experimental sequence. We label the columns based on the six crystal configurations. The vertical axis gives the modulation depth analysed in each of the rows.
As indicated by the bright entries of the array plot, Kink10 decays to zigzag crystals in similar ratios. In contrast to the Kink8, as shown in fig. 5.5, there are only few transformation to a Kink8 structure.